2018

Enhancing PV Panel Convective Cooling Using A Trip Wire

Ashhar Ahmed
University of Windsor

Enhancing PV Panel Convective Cooling Using A Trip Wire

By

Ashhar Ahmed

A Thesis
Submitted to the Faculty of Graduate Studies
through the Department of Mechanical, Automotive, and Materials Engineering
in Partial Fulfillment of the Requirements for
the Degree of Master of Applied Science at the University of Windsor

Windsor, Ontario, Canada

2018

Enhancing PV Panel Convective Cooling Using A Trip Wire

by

Ashhar Ahmed

APPROVED BY:

_____

S. Ray, Special Committee Member

Essex Energy Corporation

_____

P. Henshaw

Department of Civil and Environmental Engineering

_____

J. Defoe

Department of Mechanical, Automotive and Materials Engineering

_____

D.S-K. Ting, Advisor

Department of Mechanical, Automotive and Materials Engineering

January 17, 2018

DECLARATION OF CO-AUTHORSHIP / PREVIOUS PUBLICATION

I hereby declare that this thesis comprises of three experiments which are the result of join research in collaboration with Mr. Steve Ray, Essex Energy Corporation under the supervision of Dr. David S.-K. Ting, University of Windsor. In all cases, the key ideas, primary contributions, experimental designs, data analysis, interpretation, and writing were performed by the author. The contribution of Dr. Ting was primarily through the provision of supervision, refinement of ideas and editing of manuscript. The contribution of Mr. Steve Ray was primarily through the editing of manuscript. This thesis included one original paper that has been previously submitted for publication in a peer-reviewed journal as follows:

Thesis Chapter	Publication Title/Full Citation	Publication Status*
Appendix A	Ahmed, A., Ting, D. S-K., and Ray, S., "Promoting Vortical Flow Over a Flat Plate Using a Cylindrical Rod on the Leading Edge", European Journal of Fluid Mechanics.	Under Review

I am aware of the University of Windsor Senate Policy on Authorship and I certify that I have properly acknowledged the contribution of other researchers to my thesis, and have obtained written permission from each of the co-author(s) to include the above material(s) in my thesis.

I certify that, with the above qualification, this thesis, and the research to which it refers, is the product of my own work.

I certify that I have obtained a written permission from the copyright owner(s) to include the above published material(s) in my thesis. I certify that the above material describes work completed during my registration as graduate student at the University of Windsor.

I declare that, to the best of my knowledge, my thesis does not infringe upon anyone's copyright nor violate any proprietary rights and that any ideas, techniques, quotations, or any other material from the work of other people included in my thesis, published or otherwise, are fully acknowledged in accordance with the standard referencing practices. Furthermore, to the extent that I have included copyrighted material that surpasses the bounds of fair dealing within the meaning of the Canada Copyright Act, I certify that I have obtained a written permission from the copyright owner(s) to include such material(s) in my thesis.

I declare that this is a true copy of my thesis, including any final revisions, as approved by my thesis committee and the Graduate Studies office, and that this thesis has not been submitted for a higher degree to any other University of Institution.

ABSTRACT

The current study focuses on the cooling of photovoltaic panels by utilizing a two-dimensional bluff body. A bluff body placed on the surface of a flat plate acts as a vortex generator in the near-wake, and a turbulence generator in the far-wake. As a result, the boundary layer over the flat plate becomes turbulent and conducive to heat transfer from the plate. As an exploratory experiment, a circular tripwire was used to augment the fluid turbulence over a flat plate. The measured flow parameters showed good potential for heat transfer augmentation. The second experiment measured heat transfer and flow with circular, square and diamond-shaped tripwires placed on a smooth plate. The experiments were performed at two Reynolds numbers (Re_d) based on the freestream velocity and diameter (d) of the tripwire. The heat transfer rate of the square and diamond-shaped tripwires was improved over a large downstream region. The peak normalized Nusselt number (Nu/Nu_o) of the diamond-shaped tripwire was observed to be around 1.4, and that of the square tripwire was around 1.2. The third experiment investigated the effect of introducing a gap (G) between the top of the smooth plate and the bottom of a diamond-shaped tripwire. Heat transfer and flow parameters for six G/d ratios were measured. When the tripwire was placed on a smooth surface, the flow structure of a smooth plate downstream of the tripwire (i.e., flow separation and reattachment) had a significant impact on heat transfer. When a gap was introduced between the smooth plate and tripwire, the von Kármán vortices shed by the tripwire interacted with the smooth plate, improving heat transfer. The turbulence produced by the tripwires, especially near the plate surface, significantly improved the Nusselt number in the far-wake. Wall-normal velocity is also an important factor in improving the heat transfer rate.

DEDICATION

I would like to dedicate my thesis to my mother and my hero, Syeda Nasreen Aisha, for her unconditional love and support without which I could never succeed.

ACKNOWLEDGEMENTS

I would like to thank my advisor Dr. David S.-K. Ting for his supervision and extremely valuable advice during my M.A.Sc. study at the University of Windsor. I would like to thank Mr. Steve Ray for his contributions and support. I would also like to thank Dr. Paul Henshaw and Dr. Jeff Defoe for providing their time and knowledge to help me achieve my Master's project. Also, I would like to thank Mr. Andy Jenner for his technical assistance.

TABLE OF CONTENTS

LIST OF TABLES

LIST OF FIGURES

LIST OF APPENDICES

CHAPTER 1

INTRODUCTION

1.1   Motivation and Background

The conversion of solar energy to electricity via photovoltaic (PV) systems is one of the most promising renewable energy technologies. However, the efficiency of solar panels is strongly dependent on the operating temperature. Typically, the efficiency of a PV panel is around 15% [1]. The remaining solar radiation absorbed in the cell transforms into thermal energy and causes the temperature of the solar panel to increase. Consequently, the efficiency of the PV panel decreases [2,3], as does the overall system performance. Therefore, thermal management of PV systems plays a key role in maximizing solar panel performance. Numerous active and passive methods have been proposed to cool PV panels [3–5]. In an air-cooled system, heat can be removed by either natural or forced convection. The cooling cost of such a solution is considerably lower than that of others [5–7].

One method to increase the convective heat transfer rate is to disturb the flow over the PV panel using a rough two-dimensional element. The flow structure with an obstacle like a tripwire involves flow separation and then reattachment in the near-wake as well as high turbulence in the far-wake. In this thesis, a tripwire is defined as a two-dimensional object placed near the surface of the PV panel; transverse to the flow and extending over the span of the PV panel. It promotes the transition of a laminar boundary layer into a turbulent boundary layer. These parameters have been shown to enhance heat transfer from the surface [8,9]. Therefore, a tripwire placed on the PV panel can be an affordable and easy method to improve the heat transfer rate. Studies have also shown that multiple rows of tripwires applied over the surface more effectively enhance heat transfer. However, multiple rows of tripwires cannot be applied to a solar panel as they may block solar radiation, thus decreasing power output. Hence, to cool a solar panel, only one row of tripwires can be applied to the leading edge of the panel. It is therefore necessary to maximize the heat transfer enhancement of a single tripwire.

One method to overcome the decrease in rate of heat transfer due to separation is to introduce a gap (G) between the top of the flat surface and the bottom of the tripwire. Experiments have shown that a jet-like flow originates from the gap as the gap is increased from zero. The gap flow impinges on the flat surface, thus increasing heat transfer in the near-wake [12–14]. Another important outcome is shedding of the von Kármán vortices as the gap is increased [8,15,16]. These vortices interact with the surface to entrap and transport heat away from the flat surface. This thesis studies the effect of a tripwire on heat transfer augmentation and modifies the gap so that the overall heat transfer rate increases.

1.2   Thesis Objective and Overview

The objective of the current research is to augment the rate of heat transfer rate from a heated plate. A tripwire was placed on and near the plate to disturb the flow characteristics. The temperature distribution of the plate with and without any modification was captured with a thermal camera. This data was used to calculate the increase in the rate of heat transfer for each case. The flow parameters of each case were also measured using an X-probe hotwire anemometer. Different steps of this research are explained in the following chapters:

Chapter 1 (Introduction, current chapter)

The motivation, objective and overview of the thesis are presented.

Chapter 2 (Augmenting flat plate heat transfer via circular, square and diamond-shaped tripwires)

A new setup was used to study the effects of three tripwire geometries. Circular, square and diamond-shaped tripwires with hydraulic diameters (d) of 0.4 cm were placed on the flat surface. The heat transfer rate of each shape at two Reynolds numbers ($Re_d = 1.4 \times 10^3$ and 2.8×10^3) corresponding to freestream velocity of 5 m/s and 10 m/s respectively was determined. Also, the flow parameters at six downstream locations (x/d = 5, 10, 20, 30, 40 and 50) were acquired using an X-probe hotwire. The results show that flow structure depended on the geometry of the tripwire. The reattachment lengths and peak value of the

2

normalized Nusselt number (Nu/Nu_0) varied for each tripwire geometry. It was found that the diamond-shaped tripwire generated the best overall heat transfer augmentation for the tested downstream length and that the increase in heat transfer rate was mainly due to the higher turbulence generated by the tripwire.

Chapter 3 (On flat plate heat convection downstream of a diamond-shaped tripwire at varying gap)

It is observed that increasing the G/d ratio improves the heat transfer rate in the near-wake due to the flow coming from the gap between the tripwire and the flat surface. The results from Chapter 2 show that diamond-shaped tripwire generated the best heat transfer rate. Therefore, the effect of introducing and varying a gap (G) between the tripwire and the heated plate on heat transfer and flow parameters is studied in detail. The results of this experiment were discussed in Chapter 3. Six gap ratios (G/d = 0.3, 1.3, 2.3, 3.3, 4.3 and 5.3) were tested at $Re_d = 1.6 \times 10^3$. The flow parameters were measured at five downstream locations (x/d = 10, 20, 30, 40 and 50). Also, the flow parameters with the most influence on heat transfer enhancement of the plate were identified as the vortices shed from the tripwire, and turbulence intensity.

Chapter 4 (Conclusion)

The work in the previous chapters was summarized and this thesis was concluded with recommendations for future work.

Appendix A. An exploratory experiment was carried out to establish the flow structure of a circular tripwire and its suitability for heat transfer applications. This experiment was not included in the main body of the thesis as the setup and the existing flow conditions were different than the other two experiments. The tripwire was placed at the leading edge of a flat plate. A circular stainless steel tripwire with a diameter (d) of 0.4 cm was placed at the leading edge of the flat plate. The gap ratio (G/d) was set to zero, and the flow parameters at x/d = 6.25, 12.5, 18.75, 25 and 31.25 were acquired. The Reynolds number (Re_d) based on the diameter of the tripwire is changed from 0.7×10^3 to 2.0×10^3. The flow and turbulence parameters indicate that the tripwire produced high turbulence as well as high wall-normal velocity near the surface of the flat plate.

Appendix B The uncertainty calculation method for heat transfer and flow measurements is published.

References

[1]   M.A. Green, K. Emery, Y. Hishikawa, W. Warta, E.D. Dunlop, D.H. Levi, A.W.Y. Ho-Baillie, Solar cell efficiency tables (version 49), Prog. Photovoltaics Res. Appl. 25 (2017) 3–13. doi:10.1002/pip.2855.

[2]   Z. Ling, Z. Zhang, G. Shi, X. Fang, L. Wang, X. Gao, Y. Fang, T. Xu, S. Wang, X. Liu, Review on thermal management systems using phase change materials for electronic components, Li-ion batteries and photovoltaic modules, Renew. Sustain. Energy Rev. 31 (2014) 427–438. doi:10.1016/J.RSER.2013.12.017.

[3]   R. Kumar, M.A. Rosen, A critical review of photovoltaic–thermal solar collectors for   air   heating,   Appl.   Energy.   88   (2011)   3603–3614. doi:10.1016/J.APENERGY.2011.04.044.

[4]   B. Du, E. Hu, M. Kolhe, Performance analysis of water cooled concentrated photovoltaic (CPV) system, Renew. Sustain. Energy Rev. 16 (2012) 6732–6736. doi:10.1016/j.rser.2012.09.007.

[5]   H.M.S.S. Bahaidarah, A.A.B.B. Baloch, P. Gandhidasan, Uniform cooling of photovoltaic panels: A review, Renew. Sustain. Energy Rev. 57 (2016) 1520–1544. doi:10.1016/j.rser.2015.12.064.

[6]   J.K. Tonui, Y. Tripanagnostopoulos, Air-cooled PV/T solar collectors with low cost performance   improvements,   Sol.   Energy.   81   (2007)   498–511. doi:10.1016/J.SOLENER.2006.08.002.

[7]   M. Hasanuzzaman, A.B.M.A. Malek, M.M. Islam, A.K. Pandey, N.A. Rahim, Global advancement of cooling technologies for PV systems: A review, Sol. Energy. 137 (2016) 25–45. doi:10.1016/j.solener.2016.07.010.

[8] E. Marumo, K. Suzuki, T. Sato, Turbulent heat transfer in a flat plate boundary layer disturbed by a cylinder, Int. J. Heat Fluid Flow. 6 (1985) 241–248. doi:10.1016/0142-727X(85)90056-6.

[9] S. Chamoli, N.S. Thakur, J.S. Saini, A review of turbulence promoters used in solar thermal systems, Renew. Sustain. Energy Rev. 16 (2012) 3154–3175. doi:10.1016/j.rser.2012.01.021.

[10] S.W. Ahn, The effects of roughness types on friction factors and heat transfer in roughened rectangular duct, Int. Commun. Heat Mass Transf. 28 (2001) 933–942. doi:10.1016/S0735-1933(01)00297-4.

[11] R.P. Saini, J. Verma, Heat transfer and friction factor correlations for a duct having dimple-shape artificial roughness for solar air heaters, Energy. 33 (2008) 1277–1287. doi:10.1016/j.energy.2008.02.017.

[12] M.S. Akoz, Flow structures downstream of the horizontal cylinder laid on a plane surface, Proc. Inst. Mech. Eng. Part C J. Mech. Eng. Sci. 223 (2009) 397–413. doi:10.1243/09544062JMES1111.

[13] C. Lei, L. Cheng, K. Kavanagh, Re-examination of the effect of a plane boundary on force and vortex shedding of a circular cylinder, J. Wind Eng. Ind. Aerodyn. 80 (1999) 263–286. doi:10.1016/S0167-6105(98)00204-9.

[14] T. Kim, B. Lee, D. Lee, Study on the unsteady wakes past a square cylinder near a wall, J. Mech. Sci. Technol. 19 (2005) 1169–1181. doi:10.1007/BF02984039.

[15] S. Sarkar, S. Sarkar, Vortex dynamics of a cylinder wake in proximity to a wall, J. Fluids Struct. 26 (2010) 19–40. doi:10.1016/j.jfluidstructs.2009.08.003.

[16] G.-S. He, C. Pan, J.-J. Wang, Dynamics of vortical structures in cylinder/wall interaction with moderate gap ratio, J. Fluids Struct. 43 (2013) 100–109. doi:10.1016/j.jfluidstructs.2013.09.005.

CHAPTER 2

AUGMENTING FLAT PLATE HEAT TRANSFER VIA CIRCULAR, SQUARE AND DIAMOND-SHAPED TRIPWIRES

Nomenclature

A = Area of flat plate

d = Diameter or width of tripwire

h = Heat transfer coefficient

K_{PTFE} = Thermal conductivity of Polytetrafluoroethylene (PTFE)

K_{air} = Thermal conductivity of air

Nu = Nusselt number

Nu_o = Base Nusselt number without tripwire

PTFE = Polytetrafluoroethylene

Re_d = Reynolds number based on the diameter of the tripwire

Re_x = Reynolds number based on the distance of measurement location from the leading edge

St = Strouhal number

T_{air} = Temperature of the ambient air

T_{bottom} = Temperature of the bottom surface of PTFE plate

T_{top} = Temperature of the top surface of the PTFE plate

$T_{top, o}$ = Temperature of top surface of the PTFE surface without tripwire

$\bar{U}$ = Time averaged local velocity

U_∞ = Free stream velocity

u_{rms} = Fluctuating velocity

x = Streamwise distance from the tripwire

z = Wall-normal distance from the plate surface

ν = Kinematic viscosity

2.1   Introduction

Heat transfer from a flat surface is of practical importance because of its application in many engineering solutions. A common method to increase the heat transfer from a flat plate is to roughen the surface, thus disturbing flow via a vortex or turbulence generator. When a bluff body is placed in a fluid stream, the fluid tends to separate and recirculate, creating a significant wake region downstream [1]. If the bluff body is isolated from any other interference, the separated flow will produce von Kármán vortices. Vortices produced by a hot tripwire placed in the freestream have been shown to aid cooling [2,3]. Therefore, researchers have attempted to utilize the vortex shedding phenomenon to cool a flat surface. After placing the tripwire on a flat surface, the separation bubble from the bluff body is attached to the surface of the flat plate, significantly reducing flow velocity and causing conduction heat transfer to dominate in this region [4]. Some important observations regarding the application of a 2-D bluff body near a plate are presented in Table 2.1.

In the vicinity of a wall, separation of a bluff body is dependent not only on the Reynolds number and geometry of the tripwire but also on the gap ratio, as shown by numerous studies [2,5,6]. When a circular tripwire is placed on top of a flat surface, the flow separates from the top shoulder of the tripwire and reattachment occurs seven diameters behind it [7]. On the other hand, the flow and heat transfer with a square tripwire evolves with Re_d. The fluid separates from the front face, and as the Reynolds number increases, the sharp edge of the top surface promotes separation [2,8]. Due to this separation, the wake of the square tripwire was thicker than that of a circular tripwire [12]. Fouladi et al. [9] found that

7

the periodic vortex shedding from the shear layer observed at a lower Re_d vanished as Re_d increased. Furthermore, reattachment length was observed to vary from three to ten diameters [4,10,11].

Square tripwires have been the focus of a lot of studies, especially in relation to heat transfer [4,11,13]. Comparison of the effect of span or length of tripwire with respect to the span of the plate (continuous vs. truncated) on the heat transfer rate was conducted by Wang et al. [4], who showed that a truncated tripwire generates twin vortices. Liou et al. [10] investigated the effect of a pair of square tripwires and distance between them on the near-wake heat transfer [10], observing that the reattachment length from the first tripwire decreased as the distance between the tripwires increased from 1 to 20, while the reattachment from the trailing tripwire stayed constant. Liu et al. [14] performed an extensive analysis of the arrangement of truncated square tripwires with eight simulation cases. Reattachment and recirculation were measured behind each subsequent wire. Yadav and Bhagoria [15] analyzed the effect of a series of square tripwires at different pitch ratios and rib heights, showing that reattachment length after the first wire was around eight diameters. It decreased for the next two to three wires but then seemed to stay the same for the remaining tripwires. The peak Nusselt number was also observed to accompany reattachment. Alfarawi et al. [16] performed extensive experiments to compare the heat transfer from semi-circular, rectangular and hybrid semi-circular and rectangular tripwires. They concluded that, even though a hybrid semi-circular and rectangular tripwire increased heat transfer, it also increased the pressure drop in the flow.

Table 2.1 Main findings of the studies highlighted in this thesis. d = diameter of tripwire, FV = flow visualization experiment, G = tripwire – plate gap, HW = hot wire and/or hot film analysis, LCT = liquid crystal thermaography, LDV = laser doppler velocimetry, PIV = particle image velocimetry, PM = pressure measurements, x = downstream distance from the tripwire and X_l = tripwire placement from the leading edge.

Reference	Experiment Details	Measurement	Main Findings
Bearman & Zdravkovich [1]	Tripwire geometry = circular, $X_l = 32$, $Re_d = 2.5 \times 10^4 \sim 4.8 \times 10^4$, $G/d = 0 \sim 3.5$, $x/d = 0.4 \sim 8$.	PM, HW, FV	Separation bubble forms both upstream and downstream of the tripwire. It is attached to the tripwire at $G/d = 0$.
Ryu [2]	Tripwire geometry = square, $Re_d = 10$ and 5.0×10^4, $0.25 < G/d < 3$, $x/d = 0 \sim 20.5$.	Simulation	Flow regime depends on the Reynolds number and gap ratio. As G/d increases, the gap flow becomes stronger, leading to vortex shedding. As Re increases, fluid is separated from the top and bottom surfaces of the tripwire.
Wang [4]	Tripwire geometry = square, $Re_d = 8.0 \times 10^3 \sim 2.0 \times 10^4$, $G/d = 0$.	LCT	Local hot spots arise immediately at the rear corner of the rib. A rapid increase in heat transfer occurs in the reattachment zone. The Nusselt number decreases as the thermal boundary layer redevelops. The flow structure depends on Re. Heat transfer decreases as Re increases.
Price et al. [5]	Tripwire geometry = circular, $X_l/d = 10$, $Re_d = 1.2 \times 10^3 \sim 4.9 \times 10^3$,	FV, HW, PIV	No gap flow occurs, and a strong shear layer moves away from the plate without producing a vortex.

	G/d = 0 ~ 2, x/d = 4.8.		
Akoz [6]	Tripwire geometry = circular, $Re_d = 1.0 \times 10^3 \sim 7.0 \times 10^3$, G/d = 0, x/d = 11.	PIV	Two separation regions form behind the tripwire. The primary region forms at 9d ~ 10d downstream, and the secondary forms at 0.73d ~ 1.2d. The separation point moves downstream with increasing Re_d. The separated flow from the second separation bubble moves towards the tripwire, and before reaching the tripwire, the flow curls up and causes a vortex to form in the near-wake of the tripwire. The structure of the wake changes with Re_d.
Liou et al. [10]	Tripwire geometry = square, G/d = 0, $Re_d = 4.2 \times 10^4$.	LDV, Simulation	Three pairs of ribs are placed on the surface of a duct. Separation occurs at the first rib pair. "Velocity overshoot" is observed at 0.5d on the top surface. Reattachment length changes with Re_d.
Bayraktar et al. [12]	Tripwire geometry = circular, square and diamond, $Re_d = 0.3 \times 10^3 \sim 1 \times 10^3$, G/d = 0.1 ~ 0.8, x/d = 0 ~ 20.	Simulation	Two recirculation zones form behind the diamond-shaped tripwire at the smallest gap ratio. Increasing the G/d ratio produces vortices of different sizes. These vortices merge together at G/d = 0.8. The biggest St value is associated with the circular tripwire, and the next largest is associated with the diamond-shaped tripwire.
Kamali et al. [13]	Tripwire geometry = square, triangle and trapezoid, $Re_d = 2.0 \times 10^3$, G/d = 0, x/d = 0 ~ 10.	Simulation	The simulation results align well with the results of Wang et al. [4]. The Nu/Nu_o trends for square and triangular ribs are very similar. However, the recirculation zone for a triangular rib has a higher Nu/Nu_o.

The above literature review shows that much is still unknown concerning the most effective way to augment heat transfer from a flat plate. This is true even for the simplest case: a two-dimensional bluff body. This study aims to shed some light on this phenomenon by using circular, square and diamond-shaped tripwires to enhance the heat convection of a uniform flat surface. The analysis reveals the effect of 3 geometric of 2-D wires on heat transfer from a heated surface at two Reynolds numbers. In addition, flow parameters such as time averaged velocity and turbulence intensity are discussed. Comparison of the results of the experiments is expected to reveal the best geometry for heat transfer augmentation. The circular, square and diamond-shaped tripwires were placed on the surface of a heated polytetrafluoroethylene (PTFE) plate, and the temperature distribution of the plate was quantified using a thermal camera. In addition, the flow was measured at $x/d = 5, 10, 20, 30, 40,$ and 50 downstream from the tripwire using an X-probe hotwire anemometer.

2.2 Experimental Setup and Apparatus

The experiments were carried out in a closed-loop wind tunnel, as shown in Figure 2.1. The test section was 183 cm long, with a 76 cm by 76 cm cross section. A 1.0 cm fibreglass sheet was used as the base of the test section. A 29.5 cm by 38 cm section was cut out of the fibreglass sheet to enable installation of a 0.3 cm-thick PTFE plate. The thermal conductivity of the fibreglass sheet was 0.04 $Wm^{-1}K^{-1}$, while that of the PTFE was 0.25 $Wm^{-1}K^{-1}$. The tripwire was placed at the junction between the PTFE and fibreglass.
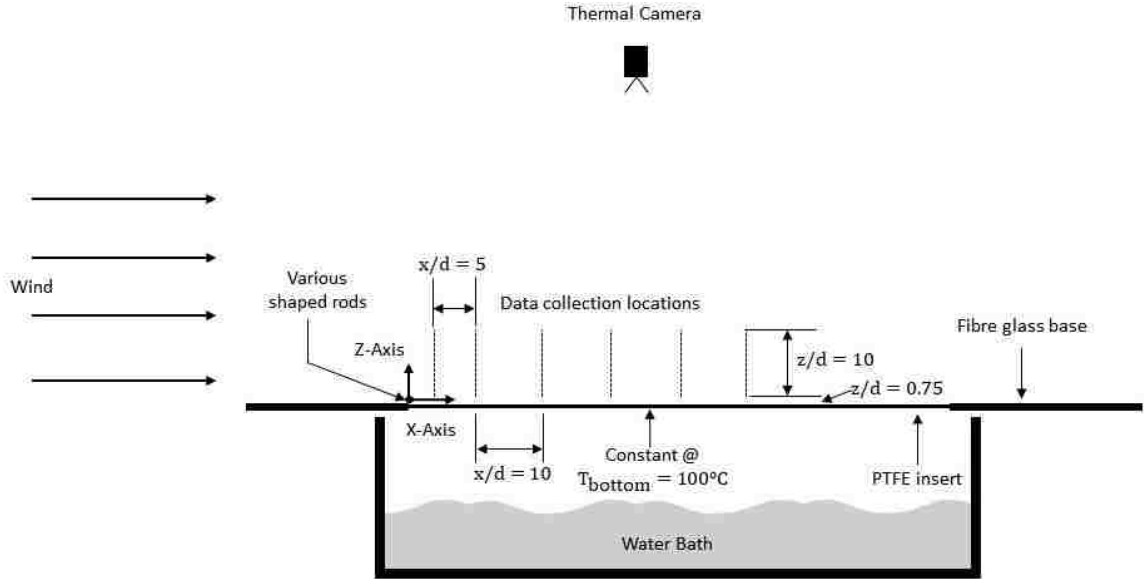
Figure 2.1 Experimental setup showing the placement of tripwire and data acquisition points.

A hot water bath was used to generate steam at 100 °C, which heated up the PTFE insert. A Fluke TiX520 camera was used to capture a thermal image of the PTFE section. Two T-type thermocouples were used to verify the temperatures of the top and bottom surfaces at the trailing edge of the PTFE insert.

A Dantec hot-wire X-probe (model 55P61) was used to acquire 10^6 samples of instantaneous velocities. The probe was connected via a 55H25 support to two constant temperature anemometers (model 55C90) modules on a StreamLine Pro frame. Data were acquired using Streamware software, and they were sampled at 80 kHz and low-pass filtered at 30 kHz to avoid aliasing. The flow data was analyzed at five downstream locations (x/d = 5, 10, 20, 30, 40 and 50). At each x/d location, data was acquired from z/d = 0.75 ~ 10 at intervals of 0.25. Due to the physical dimensions of the hotwire probe, data could not be acquired from z/d < 0.75.

Circular, square and diamond-shaped tripwires were used in this experiment. The diameter (d) of the circular tripwire was 0.4 cm, while the cross section of the square-shaped tripwire was 0.4 cm by 0.4 cm. The square tripwire was rotated 45° to create a diamond-shaped tripwire. All tripwires were 50 cm long. The dimensions of the tripwires were chosen so that the hydraulic diameter of each shape would remain the same.

The Reynolds number can be calculated based on the hydraulic diameter (d) as well as the downstream distance (x) using Equation 2.1:

$$Re_d = \frac{U_\infty \cdot d}{\nu} \qquad\qquad (2.1)$$

where ν is the kinematic viscosity of air and d is the hydraulic diameter of the tripwire. The Reynolds numbers based on diameter (Re_d) and downstream distance (Re_x) for each test case are presented in Table 2.2.

Table 2.2 Test matrix presenting the studied Reynolds numbers and downstream distances.

x/d Re$_d$ \ Re$_x$	5	10	20	30	40	50
1.4×10^3	7.5×10^3	1.5×10^4	3.0×10^4	4.5×10^4	6.0×10^4	7.5×10^4
2.8×10^3	1.5×10^4	3.0×10^4	6.0×10^4	9.0×10^4	1.2×10^5	1.5×10^5

Before conducting the experiments, the existing flow conditions were analyzed at six downstream locations corresponding to x/d = 0, 10, 20, 30, 40 and 50. The streamwise velocity and turbulence intensity profiles are shown in Figure 2.2. The boundary layer thickness (where $\overline{U} = 0.99U_\infty$) was 2.4 cm (or 6d) at x/d = 0 (i.e., the location where the

tripwires were placed). The shape factor (Figure 2.3) of the existing unperturbed flow at the tested conditions shows that the boundary layer is turbulent.

(a)   (b)
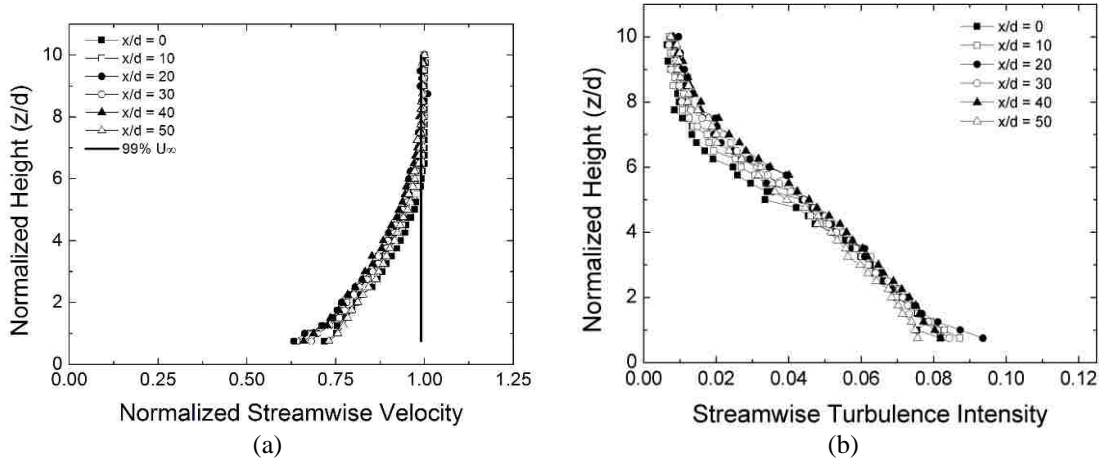
Figure 2.2 Normalized time-averaged velocities and turbulence intensities in a streamwise direction at various x/d locations.
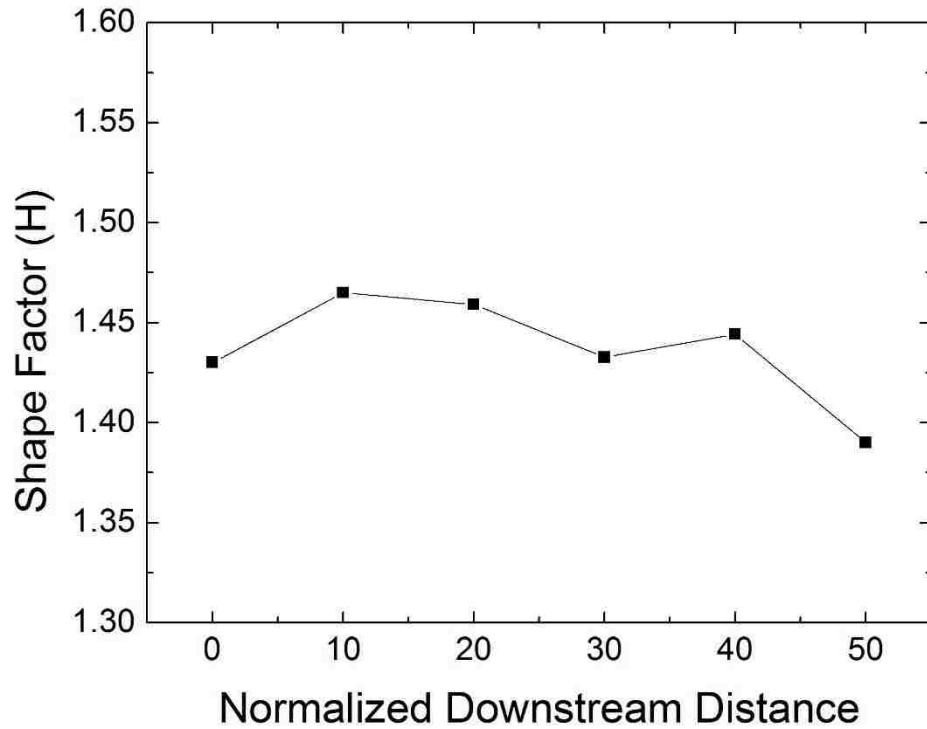
Figure 2.3 Shape factor of the unperturbed flow over the plate at the tested locations

2.3 Data Reduction and Analysis

2.3.1   Heat Transfer Parameters

Heat transfer away from a flat PTFE surface can be computed using Equation 2.2:

$$Q_{Total} = K_{PTFE} \cdot A \frac{T_{bottom} - T_{top}}{t_{PTFE}} \qquad (2.2)$$

where K_{PTFE} is the thermal conductivity of the PTFE, which is 0.25 $Wm^{-1}K^{-1}$; A is the surface area of the PTFE surface; T_{bottom} is the temperature of the PTFE surface at the bottom and T_{top} is the temperature of the PTFE surface at the top.

The total heat transfer calculated from the above equation consists of two major parts: convection to the air and radiation to the surroundings. The goal of this experiment was to examine convective heat transfer. To do so, radiation was calculated for each measured point using Equation 2.3 and then discounted from the total heat transfer:

$$Q_{radiation} = \sigma \cdot A \left(T_{plate,top}^4 - T_{surrounding}^4\right) \qquad (2.3)$$

where σ is Boltzmann's constant, which is 5.67×10^{-8} $Wm^{-2}K^{-4}$; A is the surface area of the PTFE surface; $T_{Plate,top}$ is the temperature of the PTFE surface at the top and $T_{surrounding}$ is the temperature of the surroundings, which is assumed to be equal to the temperature of the air.

$$Q_{Convection} = Q_{Total} - Q_{Radiation} \qquad (2.4)$$

The convective heat transfer coefficient can be calculated using the following equation:

$$h = \frac{Q_{Convection}}{A \cdot (T_{top} - T_{air})} \qquad (2.5)$$

The Nusselt number (Nu) is a dimensionless parameter representing the ratio of convective heat transfer to conductive heat transfer:

$$Nu = \frac{h \cdot a}{K_{air}} \qquad (2.6)$$

where h is the heat transfer coefficient, a is the characteristic length and K_{air} is the thermal conductivity of air. In the current study, the characteristic length is considered to be the downstream distance from the tripwire. Note that this characteristic length is cancelled out in the normalized form.

When the value of a tripwire case is divided by the corresponding base value without the tripwire, the normalized Nusselt number represents the enhancement induced by the tripwire. It is clear that the material properties (such as K_{air}) and characteristic length (a) remain the same for both cases. In addition, like T_{bottom} (which remains constant at 100 °C), they must be eliminated through this normalization.

$$\frac{Nu}{Nu_o} = \frac{h}{h_o} \qquad (2.7)$$

The contribution of radiation to the total heat transfer rate was calculated to be around 10% and 7% for the lower and higher tested velocities, respectively. The uncertainties in the calculated Nusselt number are shown in Table 2.3.

2.3.2 Flow Characteristics

The 99% boundary layer thickness (δ) is defined as the normal distance (position in z-axis in this study) from the wall where the local velocity reaches the 99% value of the freestream. It can be calculated using the following formula.

$$\delta(z) = 0.99U_\infty \qquad (2.8)$$

The momentum thickness (θ) is defined as the distance by which a surface would have to be moved parallel to itself towards the refence plane in an inviscid fluid stream of velocity (U_∞) to give the same total momentum as exists between the surface and the reference plane in a fluid. It can be calculated using the following formula.

$$\theta = \int_0^\infty \frac{U(z)}{U_\infty}\left(1 - \frac{U(z)}{U_\infty}\right) dy \qquad (2.9)$$

The displacement thickness (δ^*) can be calculated using the following formula, and it signifies the distance away from the reference plane in an inviscid fluid stream to give the same flow rate as that in a real fluid.

$$\delta* = \int_0^\infty \left(1 - \frac{U(z)}{U_\infty}\right) dy \qquad (2.10)$$

Shape factor (H) is the ratio of displacement thickness and momentum thickness, which is used to determine the nature of the boundary layer. The shape factor for a separated boundary layer is in the range of 1.8 - 2.4 [17], while it is around $1.3 - 1.4$ for a turbulent boundary layer [18].

$$H = \frac{\delta^*}{\theta} \qquad (2.11)$$

According to the definition of a turbulent flow, the output signal comprises a mean and fluctuating component of velocity. The local time-averaged velocity is the most fundamental parameter that can provide the velocity profile. The locations of shear in the flow can be easily determined from the velocity profile plots.

$$\bar{U} = \frac{1}{N}\sum_{i=1}^{N} U_i \qquad (2.12)$$

where N is the number of instantaneous readings (10^6) and U_i is instantaneous velocity.

The fluctuating component can be expressed as the root mean square velocity:

$$u_{rms} = \sqrt{\sum_{i=1}^{N} \frac{(u_i)^2}{N-1}} \qquad (2.13)$$

This root mean square velocity can be non-dimensionalized using freestream velocity:

17

$$Tu = \frac{u_{rms}}{U_\infty} \qquad\qquad (2.14)$$

It should be noted that the data from the hotwire was not modified to overcome directional insensitivity. The uncertainties associated with each flow parameter are presented in Table 2.3.

Table 2.3 Experimental uncertainties for each parameter.

Parameter	$Nu\,/Nu_o$	$\bar{U}$	$\bar{W}$	Tu_u	Tu_w	u·w
Uncertainty	5%	2%	3%	5%	5%	7%

2.4 Heat Transfer Results

The results of the heat transfer experiment are shown in Figures2.4 and 2.5 and are expressed in two parts according to Reynolds number. The general heat transfer trend, regardless of geometry or the effect of Reynolds number, is discussed in this paragraph. The normalized Nusselt number immediately behind the tripwire is lower than that of the un-tripped case. The Nusselt number continues to decrease to a minimum value. Afterwards, the Nusselt number rises to a maximum value. Heat transfer performance slowly decreases in the far-wake downstream of the mentioned peak. These regions roughly correspond to the flow separation, reattachment and boundary layer reestablishment regions, respectively. In the flow separation region, the shear layer coming from the top shoulder of the tripwire reduces the interaction of hot air near the plate with cold air above the shear layer. This is why the Nusselt number ratio decreases at locations in the near-downstream region. The Nusselt number increases in the reattachment region as the shear layer in this region comes from directly above the plate and cold fluid can mix with near-plate air. The reattachment length, defined as the location of the peak normalized Nusselt number in the near-wake, observed in the current study is compared to the results of the other studies discussed in Table 2.4.
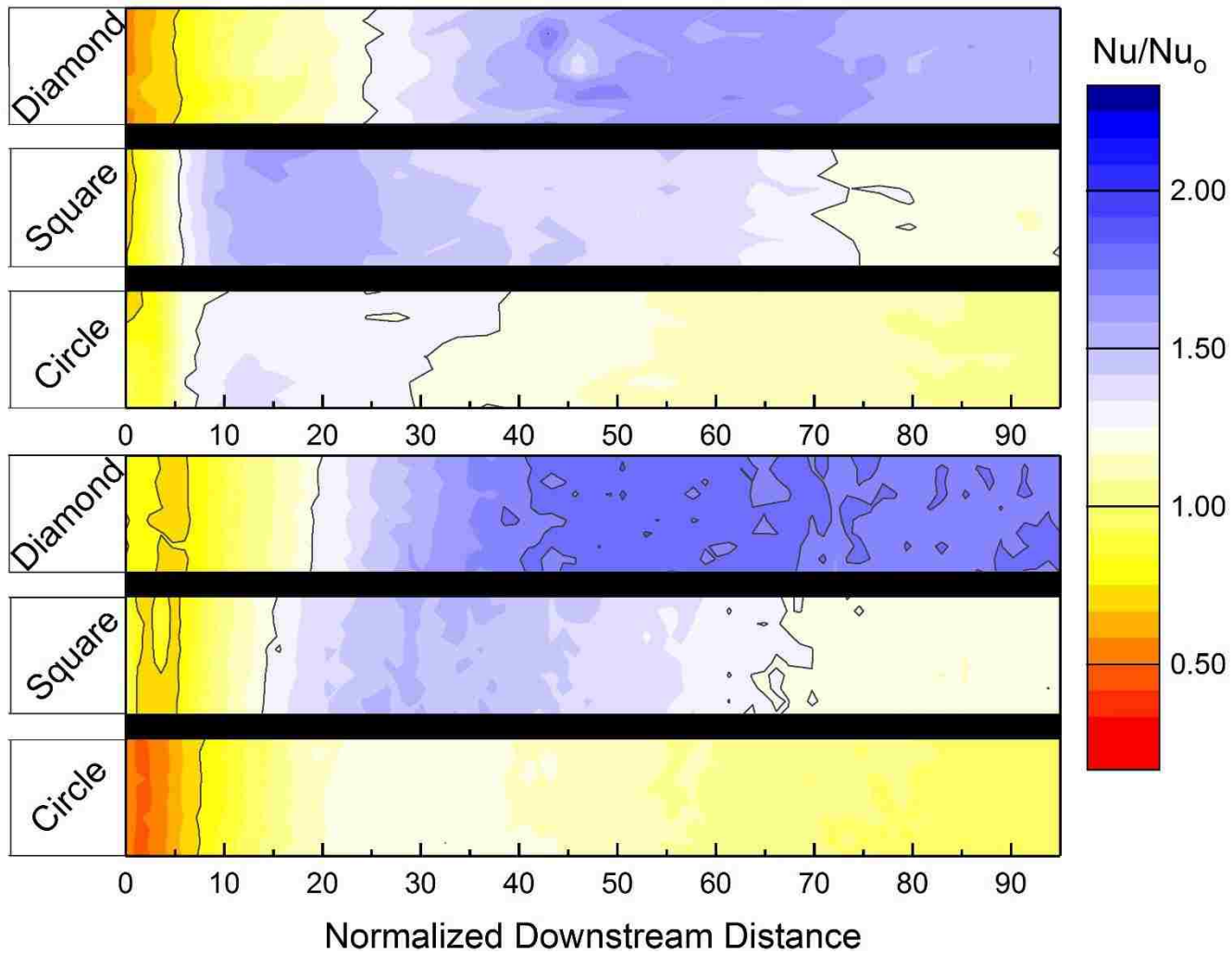
Figure 2.4 Contour plots of normalized Nusselt numbers, where top set of contour graphs represents $Re_d = 1.4 \times 10^3$ and bottom set of contour graphs represents $Re_d = 2.8 \times 10^3$. Each individual plot spans +2D to-2D from the center line of the plate.
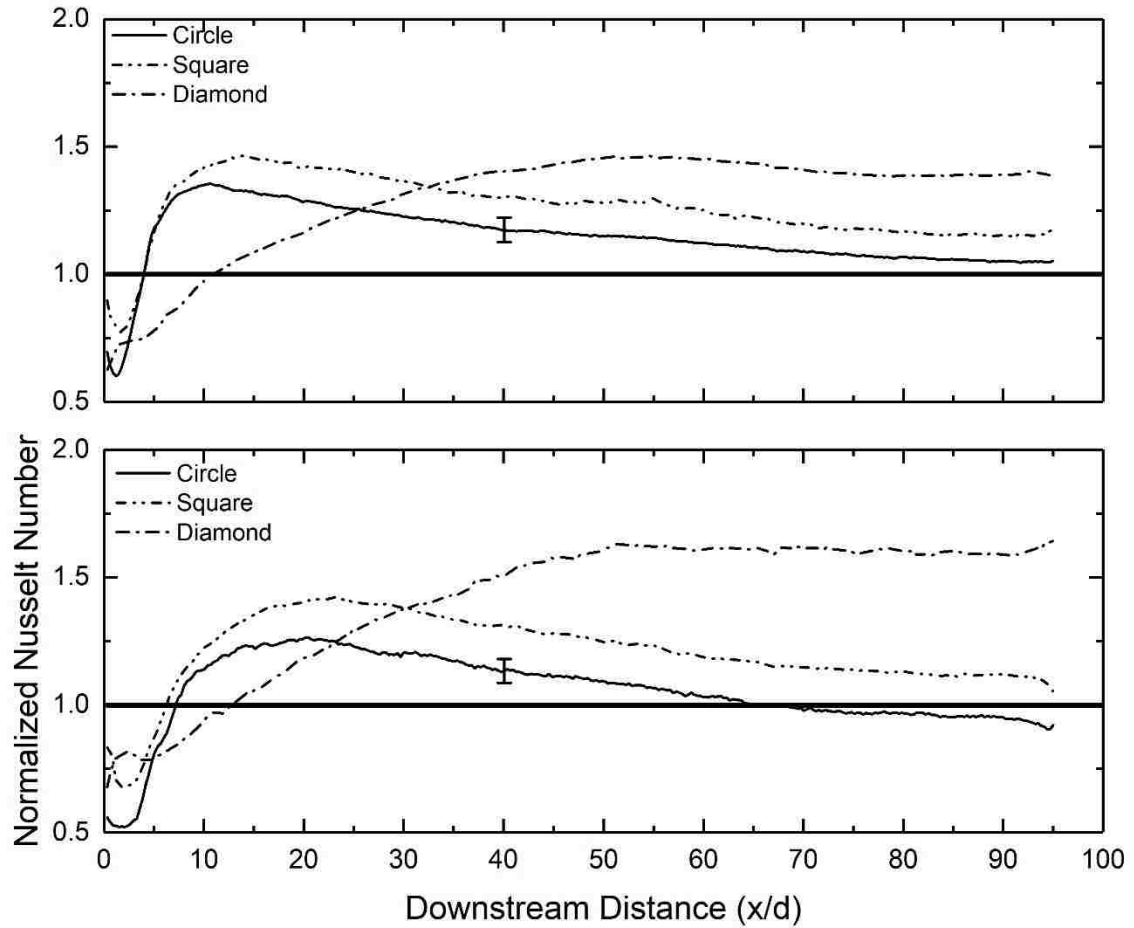
Figure 2.5 Span averaged normalized Nusselt number. Top graph shows measurements at $Re_d = 1.4 \times 10^3$ and bottom graph shows measurements at $Re_d = 2.8 \times 10^3$.

The reattachment length behind the circular tripwire observed in the current study is similar to that observed in the literature. However, in general, the reattachment lengths observed in the current study are about 15% longer because some studies [6,7,10,11] use flow measurement to determine reattachment length. Previous studies by Tariq et al. [19] and Ali et al. [20] showed that heat transfer experiments overestimated reattachment length by 10–12% due to a sweeping flow, which originated from the surface immediately after the reattachment point and shifted the maximum heat transfer area downstream. Thus, heat transfer experiments yielded longer reattachment lengths than flow data.

Table 2.4 Reattachment length and Nusselt number for different geometries compared with other studies. NA = data not available.

Geometry	Reference	Re $(\times 10^3)$	Normalized Reattachment Length (Using Nu/Nu_0)	Normalized Reattachment Length (Using H)
Circle	Akoz [6]	1.0	8.2	NA
		3.0	9.2	NA
		5.0	9.6	NA
		7.0	10.0	NA
	He et al. [7]	1.1	7.0	NA
	Present	1.4	10.0	7.0
		2.8	14.0	14.0
Square	Wang et al. [4]	8.0	4.0	NA
		20.0	3.0	NA
	Liu et al. [11]	13.2	9.75	NA
	Tariq et al. [18]	22.6	14.5	NA
		32.1	14.2	NA
		40.8	14.0	NA
	Liou et al. [10]	42.0	8.9	NA
	Present	1.4	14.0	10.0
		2.8	23.0	22.0

The reattachment length of the square tripwires is longer than that of the circular tripwire. In addition, this reattachment length increases with Reynolds number in the current study. This could be explained by the fact that the square tripwire has two sharp edges. One edge is faced towards the oncoming flow, while the other edge is faced away. At a lower

Reynolds number, the flow separates from the edge facing towards the flow and reattaches between the two edges. It then separates again from the edge facing away from the flow. Thus, the reattachment length is smaller at this Reynolds number. When the Reynolds number is higher, the flow separates from the front-facing edge and does not reattach between the two edges, leading to a thicker wake and longer reattachment length. It should be mentioned that the present reattachment length for the square tripwire is much longer compared to that identified in other studies, primarily because their Reynolds numbers are around 10 times higher than the current study. The flow regime may have changed.

The shape factors can also be assessed to evaluate the nature of the boundary layer. The flow is considered to be separated when the shape factor reaches a value between 1.8 and 2.4 [17]. An attached turbulent boundary layer however, has a shape factor in the range of 1.3 to 1.4 [18]. Figure 2.6 shows the results for each downstream location. Reference lines for a separated and attached turbulent boundary layers have also been included. The estimated locations of flow reattachment using this method has also been included in Table 2.4, and in general, they are shorter than the estimations using heat transfer experiment. It should be also noted that at $Re_d = 2.8 \times 10^3$, the boundary layers reach a shape factor of 1.4 at shorter downstream distance as compared to results from $Re_d = 1.4 \times 10^3$. Irrespective of the Reynolds number, the boundary layer behind the circular tripwire reattaches at a smaller downstream distance.
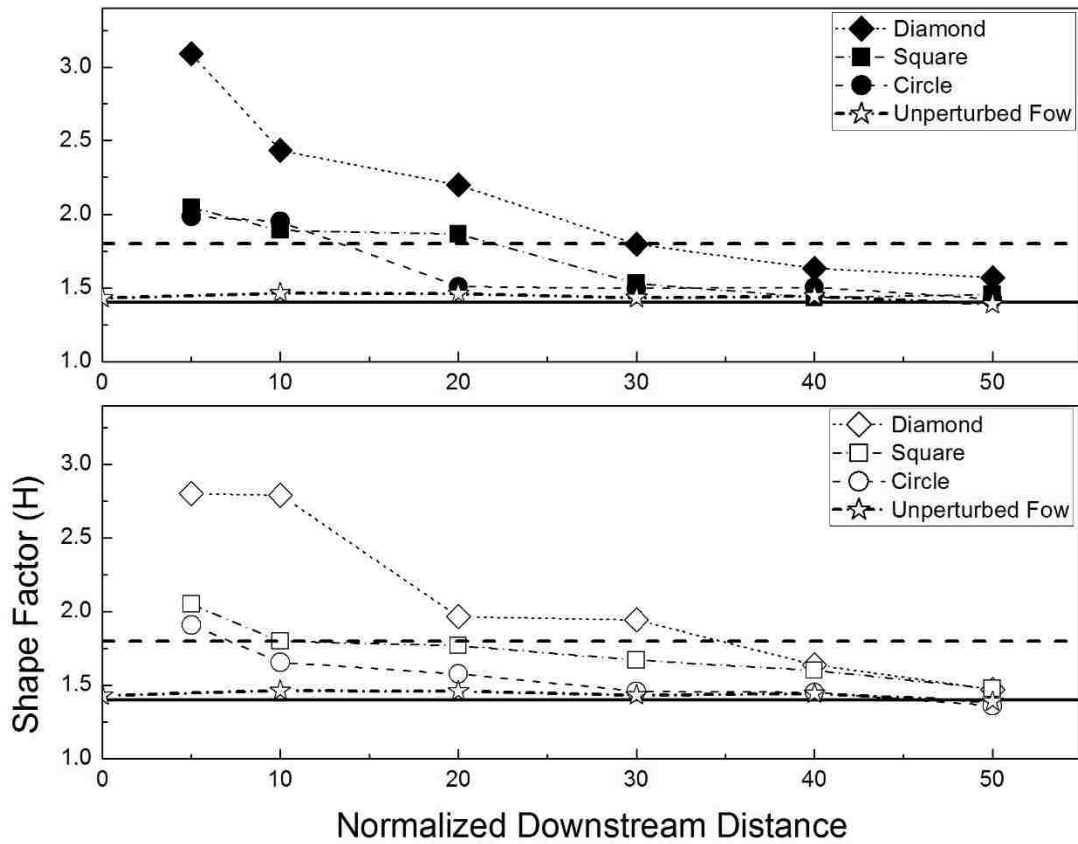
Figure 2.6 Shape factor for each downstream location, top graph shows the results from $Re_d = 2.8 \times 10^3$ and the bottom graph shows the results from $Re_d = 1.4 \times 10^3$.

2.4.1 Effect of Tripwire Geometry

The heat transfer performance of the three tested geometries at the lower Reynolds number is discussed in the following paragraphs. The minimum Nusselt number observed for the circular tripwire is 0.6 at x/d = 1.2. After the minimum value, heat transfer performance rises rapidly and achieves a peak value of 1.35 at x/d = 10. Upon further increase in x/d distance, the cooling effect is gradually reduced. At the farthest tested distance (i.e., x/d = 95), the normalized Nusselt number is around 1.05.

The results for the square tripwire are considerably better than those for the circular tripwire. The Nusselt number is higher immediately downstream of the tripwire, and the

23

minimum value is 0.77 at x/d = 1.5, which is higher than the minimum value observed for the circular tripwire. After this valley, the subsequent increase in heat transfer continues for a longer downstream distance compared to the circular tripwire case. In the near-wake (i.e., x/d < 10), the highest Nusselt number is 1.43. This value is comparatively lower in the mentioned range (i.e., x/d < 10). Unlike the circular tripwire, the Nusselt number keeps improving. The peak Nusselt number behind the square tripwire is measured to be 1.47 at x/d = 14. The subsequent increase in downstream distance decreases the cooling effect, and a minimum value of $Nu/Nu_o = 1.17$ is observed at x/d = 95.

The heat transfer trend behind the diamond-shaped tripwire can be described as follows. Initially, the Nusselt number is the lowest (0.63) for all the tested geometries. The Nusselt number is then observed to rise. It stays constant at 0.74 from x/d = 1.8 to 3.6. After this region, the Nusselt number continues to rise until it reaches a maximum value of 1.46 at a downstream distance of 54. Heat transfer behind the diamond-shaped tripwire is better than the other geometries at x/d = 34. Moving farther downstream beyond the peak value, the Nusselt number stays constant.

To summarize the results of the lower Reynolds number, the diamond-shaped tripwire shows the lowest value immediately behind the tripwire (i.e., in the near-wake). The circular tripwire shows the highest recovery rate, achieving the maximum Nusselt number in the near-wake. The cooling effect decays in the far-wake of the circular and square tripwires. The diamond-shaped tripwire generates a higher Nusselt number than the other geometries at x/d = 35.

2.4.2   Effect of Reynolds Number

The general trends for each tripwire remain the same at the higher Reynolds number with few changes. In general, the Nusselt number results are worse at the higher Reynolds number, and the peaks and valleys are observed at a lower magnitude. The changes between

the two Reynolds numbers for each geometry are discussed in detail in the following discussion.

The circular tripwire showed rapid recovery in heat transfer after the initial valley at the lower Reynolds number. At the higher Reynolds number, the recovery is much more gradual. The peak Nusselt number is also lower (1.26) and at a farther downstream location ($x/d = 20$). Beyond $x/d = 60$, the Nusselt number decreases below that of the un-tripped case.

For the square tripwire, the minimum heat transfer value is lower at the higher Nusselt number (0.68 vs. 0.70). The peak heat transfer augmentation (1.42 vs. 1.46) remains almost the same. At the tested location that is farthest downstream, the Nusselt number is lower (1.05 vs. 1.16) at the higher Reynolds number.

The Nusselt number for the diamond-shaped tripwire increases as the Reynolds number increases. In the near-wake, the Nusselt number increases (0.67 vs. 0.65), and in the far-wake, the peak value is observed to be higher as well (1.64 vs. 1.46). The peak Nusselt number is observed at $x/d = 51$.

2.5 Discussion
2.5.1   Effect of Geometry

The flow parameters can be used to better understand the heat transfer results. Starting our discussion with the flow behind the circular tripwire, streamwise velocity (Figure 2.7) at the nearest downstream location is very low. The time-averaged velocity is reduced to around 20% in the near plate locations. Turbulence (Figure 2.9) near the plate is also lower. Turbulence intensity increases further away from the plate. It peaks at the maximum velocity gradient location, and after achieving a peak, it decreases. This indicates that

turbulence is generated by shear in the velocity flow field and thus that there is a shear layer in this region, presumably produced from the top shoulder of the tripwire. Due to this shear layer, cooler fluid does not reach the plate to convect heat away from it. Thus, the Nusselt number at this location is adversely affected. In addition, a higher wall-normal velocity (Figure 2.8) is detected in the shear layer region. The turbulence (Figure 2.10) in this component follows a similar trend to that of the streamwise counterpart. In theory, higher wall-normal velocity will increase the amount of cold air interacting with the plate. However, lower streamwise velocity inhibits this heat-saturated flow from convecting away from the plate.

Moving downstream to $x/d = 10$, the streamwise velocity in near plate locations is below 30% of the freestream velocity. As the velocity measured at the location nearest to the plate increases, so does the turbulence. At higher wall-normal (z/d) locations, the decreasing trend for turbulence intensity remains the same. The wall-normal velocity is lower at this downstream location, although it is still higher near the plate. In near plate locations, the improved streamwise velocity, higher turbulence intensity and relatively higher wall-normal velocity seem to suggest that more cold air is interacting with the wall. Thus, heat transfer is promoted in this location.

The streamwise velocity and turbulence intensity near the plate continue to increase in the rest of the tested locations. Turbulence at a wall-normal velocity follows a similar trend as streamwise turbulence intensity, indicating that the boundary layer reestablishment process has started. During this process, wall-normal velocity continues to decrease. As a result, the amount of cold flow interacting with the plate decreases. Furthermore, heat transfer slowly decreases in these locations. The magnitude of the turbulence generated by the circular tripwire is the lowest among the three tested geometries.

Figure 2.7 Normalized streamwise velocity profiles. Top graph shows the results for the circular tripwire at $Re_d = 1.4 \times 10^3$, middle shows the results for the square tripwire at $Re_d = 1.4 \times 10^3$, and bottom shows the results for the diamond-shaped tripwire at $Re_d = 1.4 \times 10^3$.

Figure 2.8 Normalized wall-normal velocity profiles. Top graph shows the results for the circular tripwire at $Re_d = 1.4 \times 10^3$, middle shows the results for square tripwire at $Re_d = 1.4 \times 10^3$, and bottom shows the results for the diamond-shaped tripwire at $Re_d = 1.4 \times 10^3$.

Figure 2.9 Streamwise turbulence intensity profiles. Top graph shows the results for the circular tripwire at $Re_d = 1.4 \times 10^3$, middle shows the results for the square tripwire at $Re_d = 1.4 \times 10^3$, and bottom shows the results for the diamond tripwire at $Re_d = 1.4 \times 10^3$.

Figure 2.10 Wall-normal turbulence intensity profiles. Top graph shows the results for the circular tripwire at $Re_d = 1.4 \times 10^3$, middle shows the results for the square tripwire at $Re_d = 1.4 \times 10^3$, and bottom shows the results for the diamond-shaped tripwire at $Re_d = 1.4 \times 10^3$.

The flow behind the square tripwire is more or less similar to that of the circular one. At $x/d = 5$, the shear layer associated with velocity shear prevents the injection of cold fluid, thus restricting heat transfer in this region. Moving downstream to $x/d = 10$, the wake behind the square tripwire is thicker than that behind the circular tripwire. As a result, the heat transfer results are better than those of the circular tripwire. At this location, wall-normal velocity remains oriented towards the plate for all the measured locations. However, the magnitude of wall-normal velocity in the higher-turbulence region is comparatively higher. The turbulence produced at this location generates a higher Nusselt number. The wake continues to increase in thickness as we move downstream.

The flow behind the diamond-shaped tripwire is considerably different than that of other cases. At $x/d = 5$, the streamwise velocity near the plate is around 20%, which is the lowest value among the tested geometries. It remains at this value from $z/d = 0.75$ to 1.5. The turbulence intensity in this region is below 10%. However, the turbulence intensity profile at locations with higher z/d is similar to that of the other geometries. This indicates that the shear layer associated with the diamond-shaped tripwire is positioned higher and the low turbulence region is due to separation behind the intrusive tripwire. Due to the positioning of the shear layer and extremely low streamwise velocity, the Nusselt number here is the lowest.

It should be noted that the diamond-shaped tripwire provided a better opportunity to investigate the flow immediately behind it because the projected area of diamond-shaped tripwire is bigger than the other two geometries. We should have observed a recirculation zone below the height of the tripwire in the near-wake region as the recirculation zone has a lower diameter and height than the tripwire [5,6,21]. However, the hot wire data was not modified to overcome directional insensitivity and thus flow reversal was not observed in this study.

Moving downstream to $x/d = 10$, the streamwise velocity nearest to the plate is still around 20%. However, in the next wall-normal location, velocity increases. The velocity shear and turbulence associated with it are distributed over a wider region compared to $x/d = 5$. Wall-normal velocity is still prevalent and has a higher magnitude near the plate. Theoretically, higher wall-normal velocity should increase heat transfer, but due to the shear layer insulating the heated plate, similar to the case at $x/d = 5$, the Nusselt number is still lower than that of the un-tripped case.

Moving to $x/d = 20$, the near plate streamwise velocity recovered to 30% and the turbulence in this location increases as the wake region expands. As higher turbulence is observed closer to the wall, colder fluid can interact with the plate. The magnitude of turbulence produced by the square tripwire is the highest amongst the three geometries. The Nusselt number continues to increase in this region. Higher wall-normal velocity in the direction of the plate also contributes to the increase in heat transfer.

Farther downstream at $x/d = 30$, the streamwise velocity nearest to the plate continues to increase while the wall-normal component decreases in magnitude. The direction of the wall-normal velocity indicates that the flow is oriented toward the plate. However, turbulence intensity decreases, forming a small valley near the plate. This valley is more pronounced in the wall-normal turbulence intensity profile than the streamwise turbulence intensity profile. It should be noted that the wake of the diamond-shaped tripwire is thickest of all the geometries due to the bigger projected area. Increased time-averaged velocity and higher turbulence in the near plate region indicate more mixing of hotter and colder fluid, which enhances heat transfer.

The trend of increasing streamwise velocity near the plate continues further downstream. Negative wall-normal velocity is also observed at the last two measured locations. At locations that are farther downstream, the wake decreases in strength as turbulence

intensity decreases. Even with decreased magnitude, turbulence intensity and wall-normal velocity generate higher Nusselt numbers at these locations.

2.5.2   Effect of Reynolds Number

At the higher Reynolds number, the individual trends for each flow parameter do not change. However, the magnitude of each parameter is lower compared to that at the lower Reynolds number. As a result, the heat transfer behind each tripwire is lower at the higher Reynolds number. This observation is similar to the findings of other studies as discussed in the Table 2.1. This is because the boundary layer becomes turbulent at a shorter downstream distance at the higher Reynolds number. A few differences between the two Reynolds numbers are discussed below.

Behind the circular tripwire, the normalized velocity profiles (Figure 2.11) and wall-normal velocity (Figure 2.12) have lower magnitudes at all the corresponding locations. At $x/d = 30$, wall-normal velocity is observed to be almost zero at all wall-normal locations. Farther downstream, wall-normal velocity changes its direction, moving away from the wall. Turbulence intensity (Figure 2.13 and 2.14) is also reduced. This is why the rate of heat transfer decreases at higher Reynolds numbers.

Similar differences are observed for the flow behind the square tripwire at the two Reynolds numbers. Wall-normal velocity decreases as we move farther downstream, and it changes direction at the farthest measured location. This reversal of flow direction does not decrease the Nusselt number below 1 as observed for the circular tripwire.

Wall-normal velocity does not change direction behind the diamond-shaped tripwire at the higher Reynolds number. However, the lower-magnitude time-averaged velocity and

33

turbulence generated by the shear tripwire produce a lower Nusselt number, similar to the other geometries.
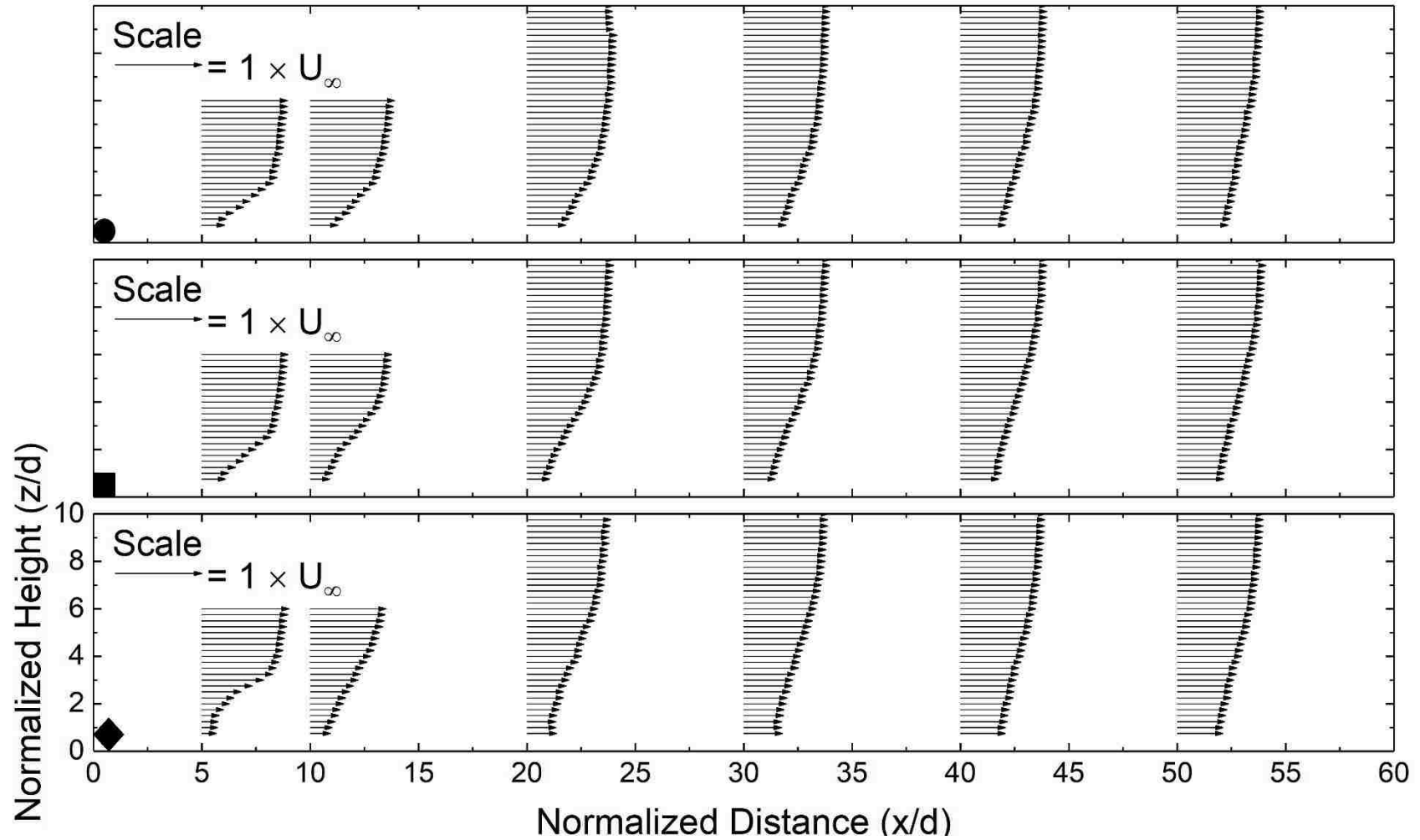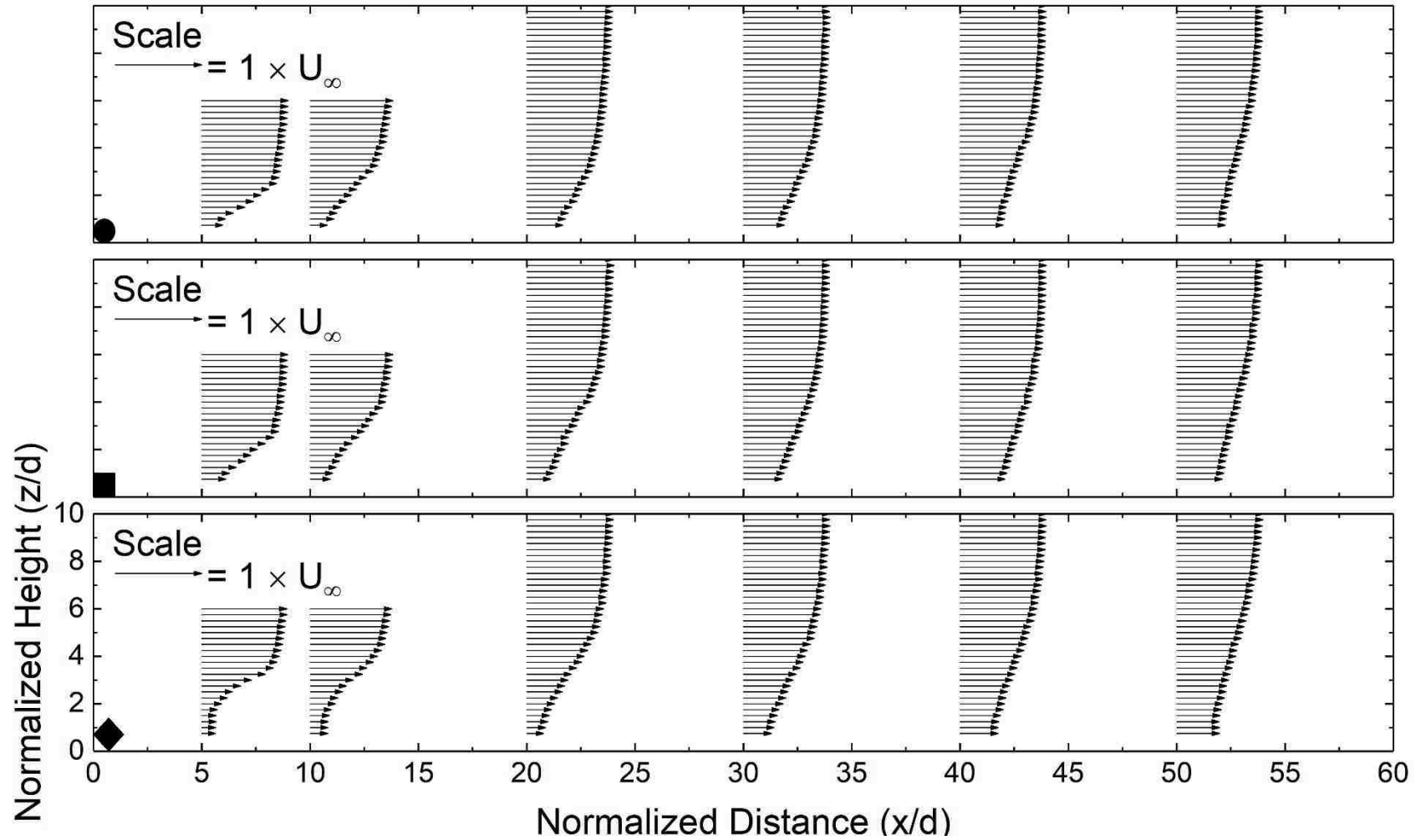
Figure 2.11 Normalized streamwise velocity profiles. Top graph shows the results for the circular tripwire at $Re_d = 2.8 \times 10^3$, middle shows the results for the square tripwire at $Re_d = 2.8 \times 10^3$, and bottom shows the results for the diamond-shaped tripwire at $Re_d = 2.8 \times 10^3$.
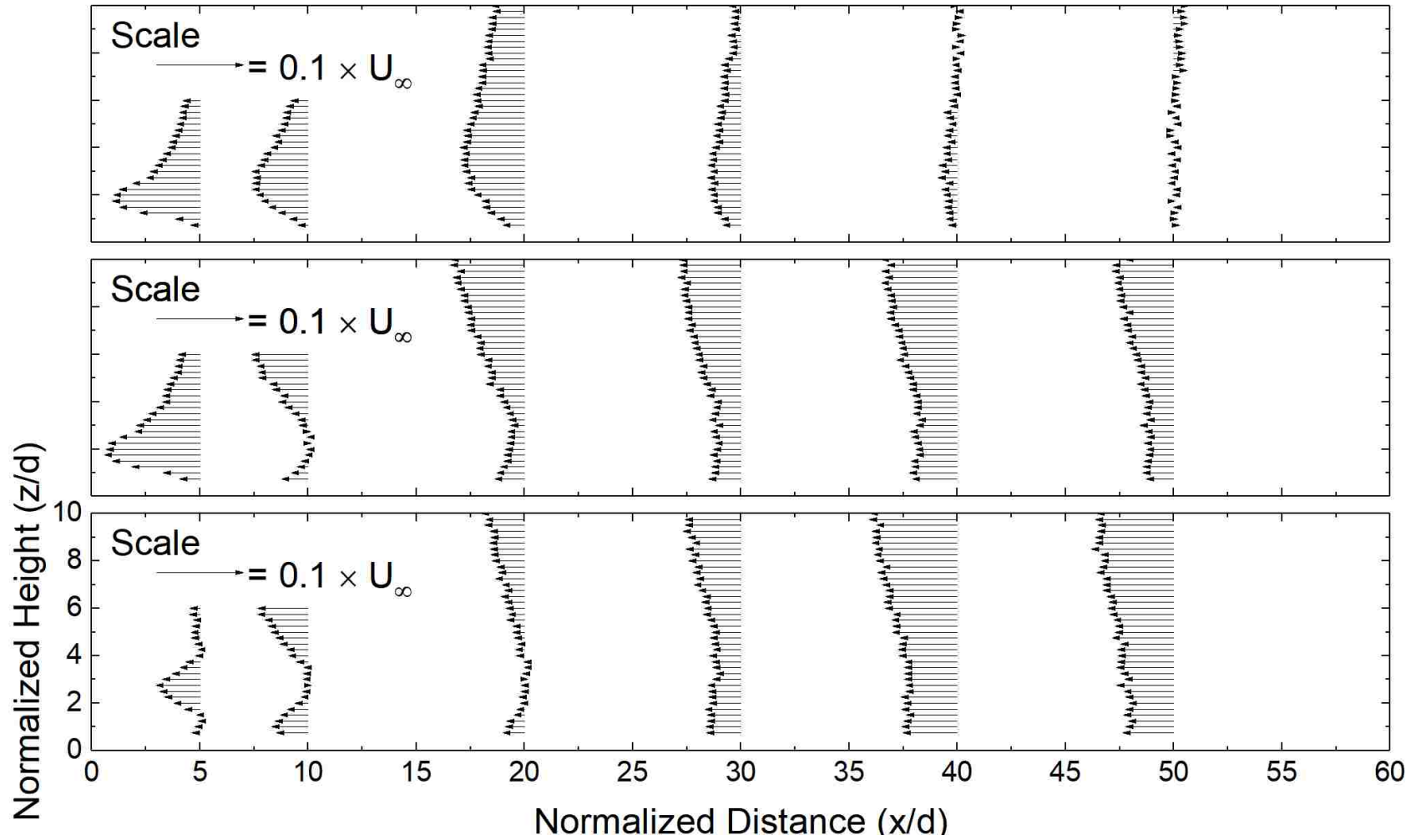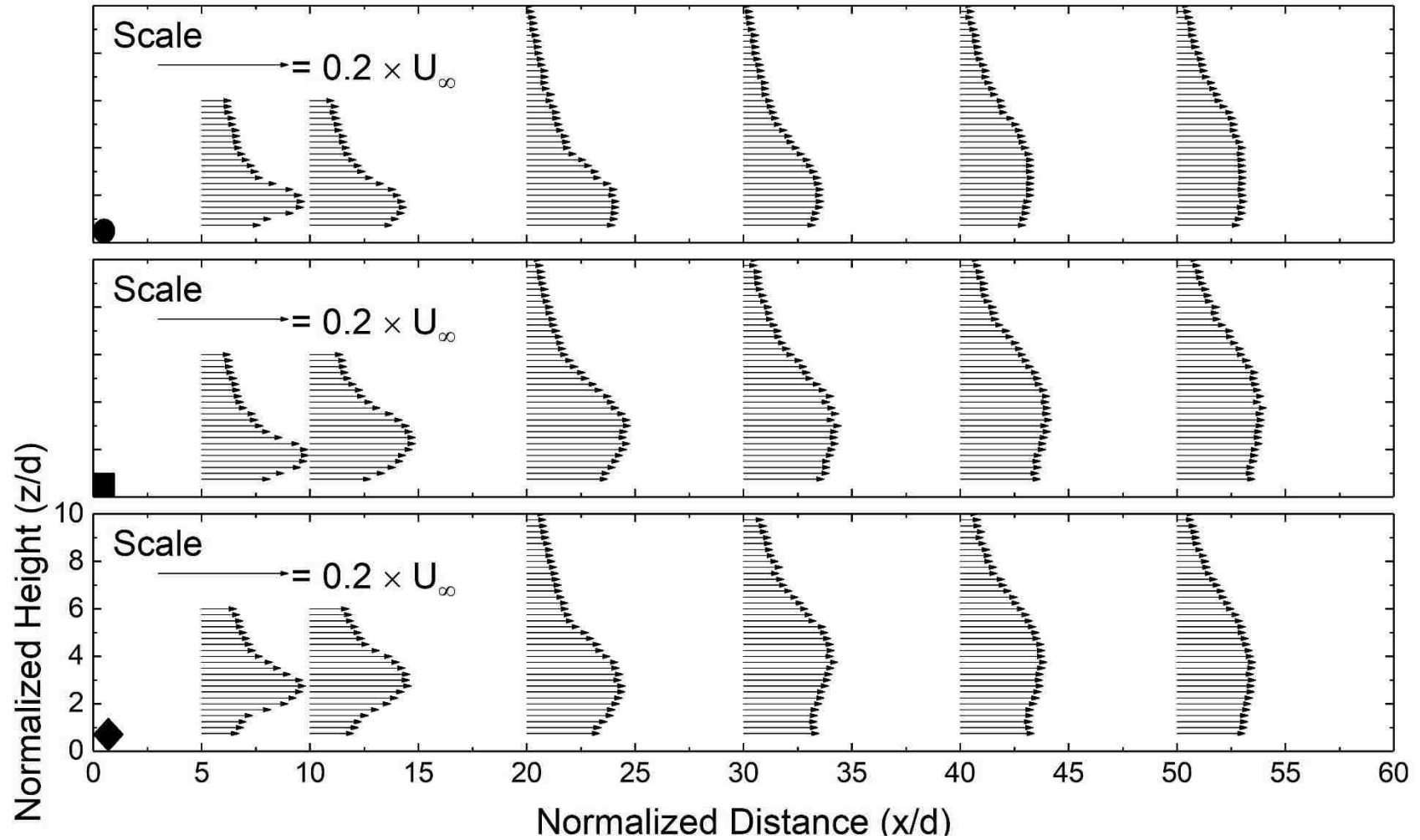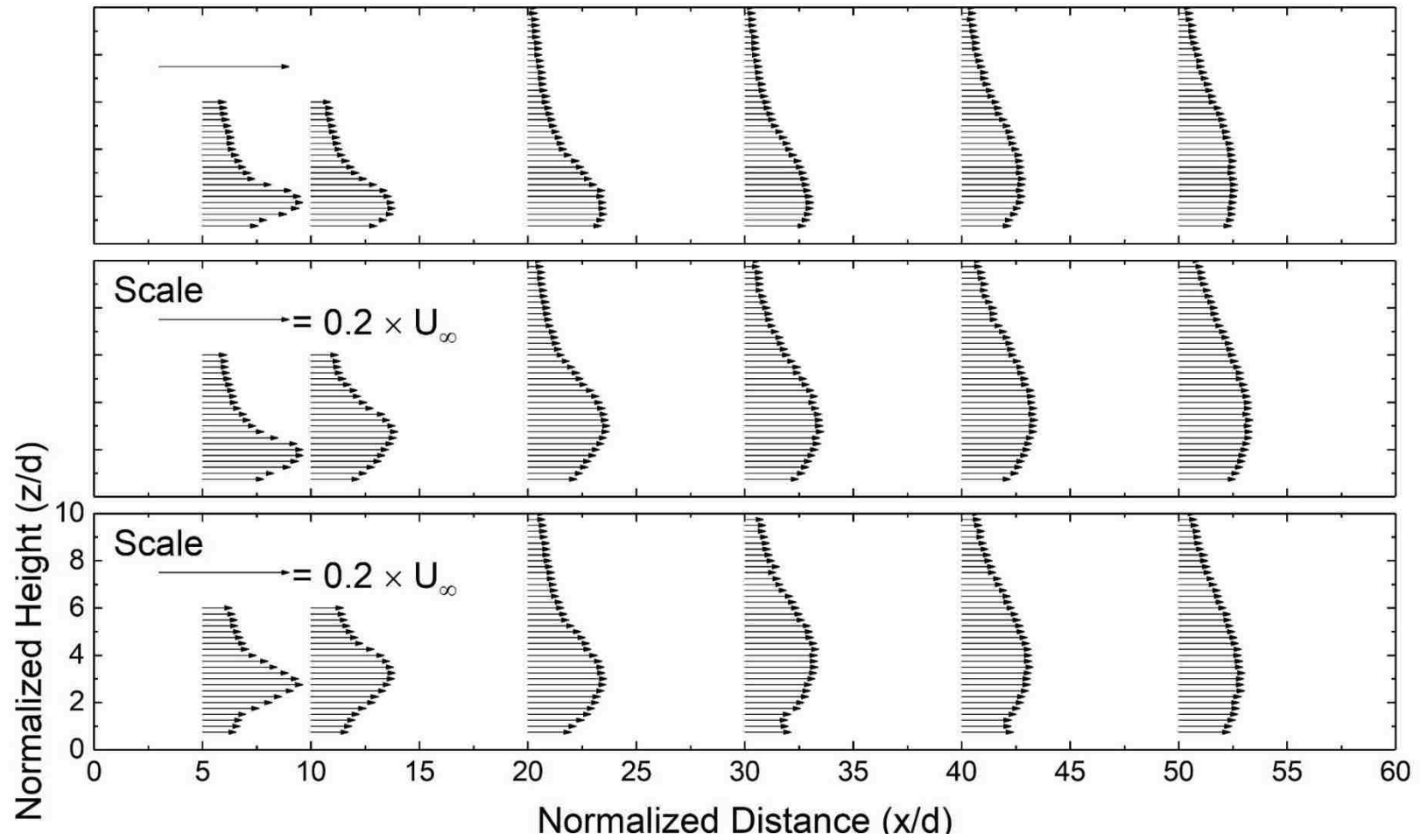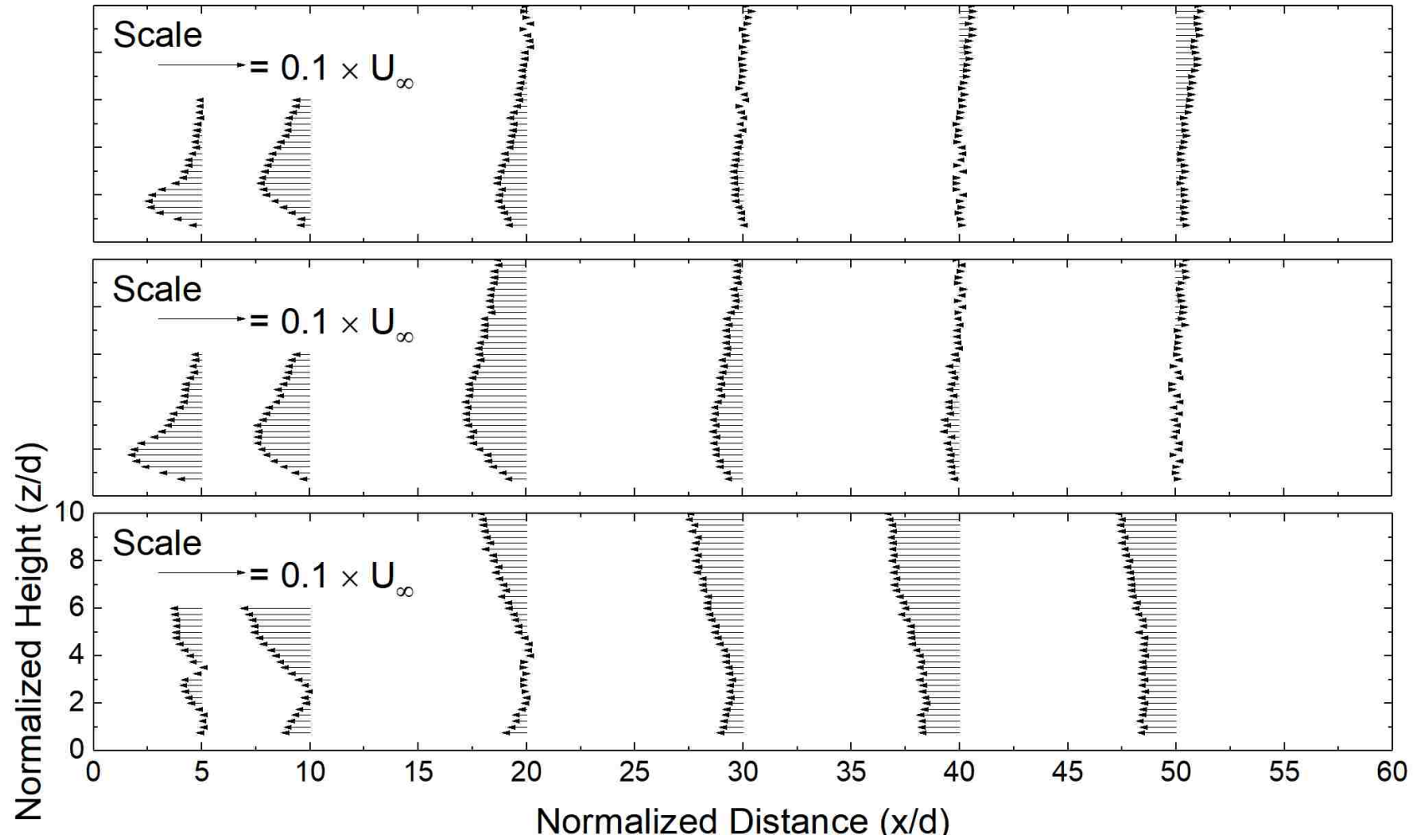
Figure 2.12 Normalized wall-normal velocity profiles. Top graph shows the results for the circular tripwire at $Re_d = 2.8 \times 10^3$, middle shows the results for the square tripwire at $Re_d = 2.8 \times 10^3$, and bottom shows the results for the diamond-shaped tripwire at $Re_d = 2.8 \times 10^3$.
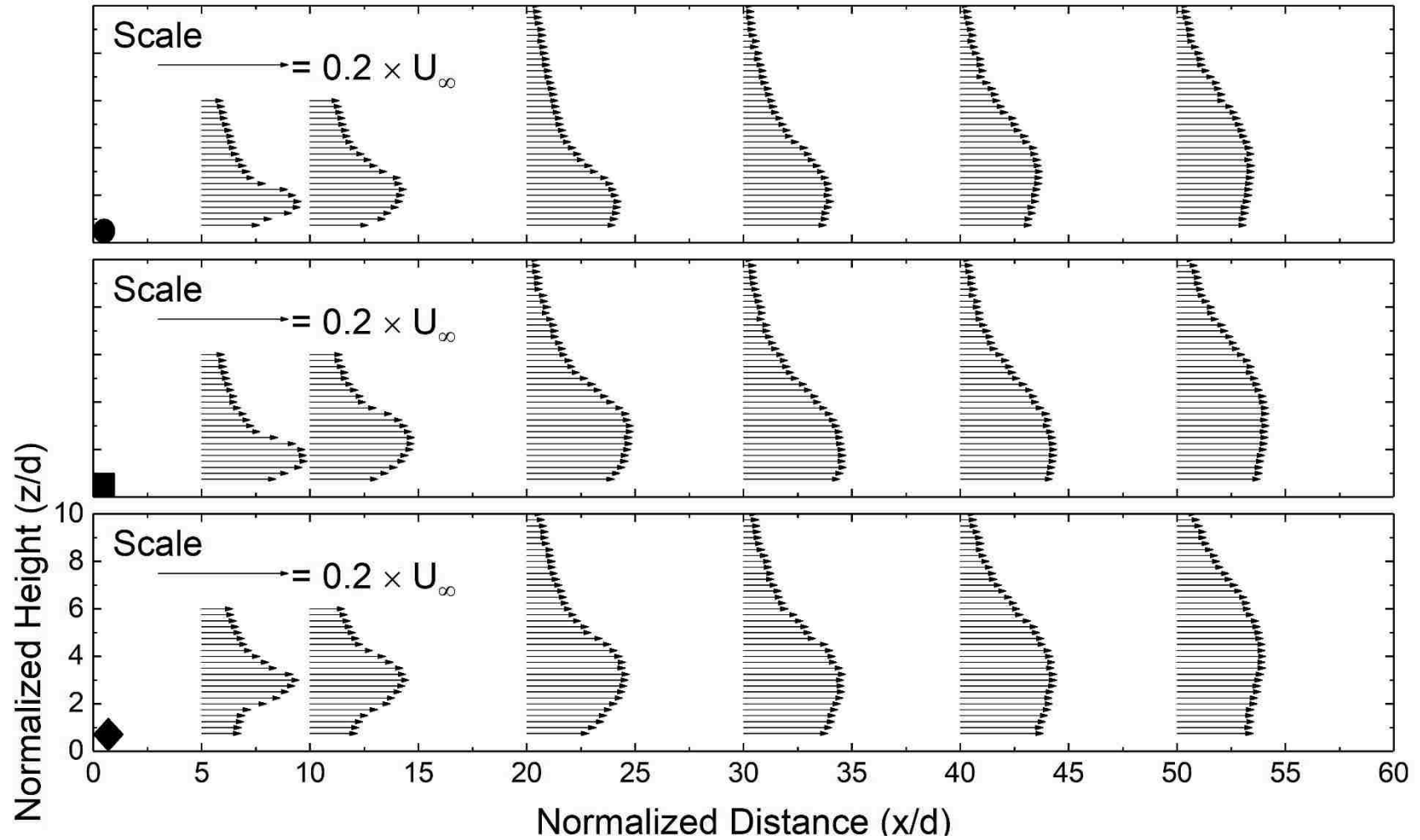
Figure 2.13 Streamwise turbulence intensity profiles. Top graph shows the results for the circular tripwire at $Re_d = 2.8 \times 10^3$, middle shows the results for the square tripwire at $Re_d = 2.8 \times 10^3$, and bottom shows the results for the diamond-shaped tripwire at $Re_d = 2.8 \times 10^3$.
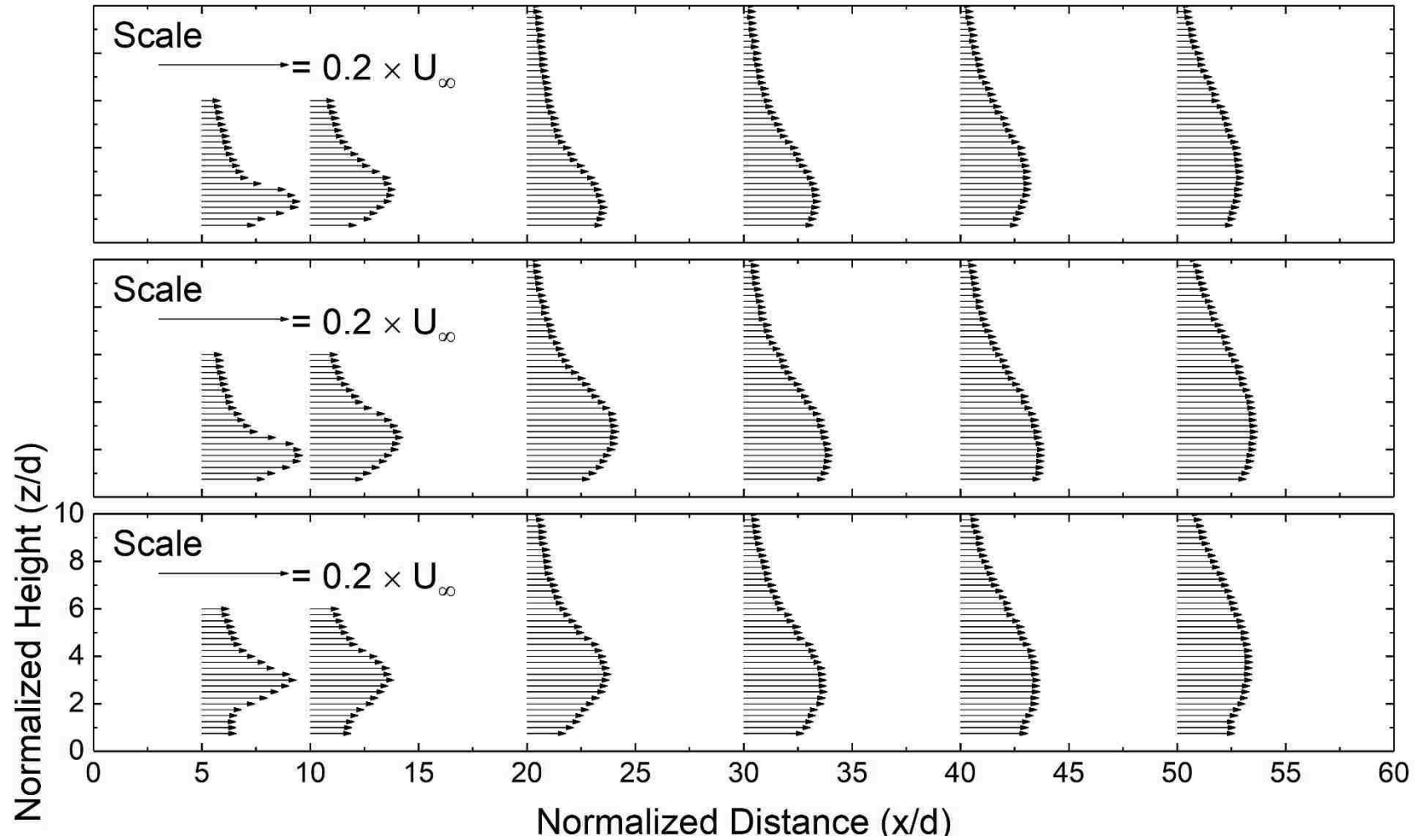
Figure 2.14 Wall-normal turbulence intensity profiles. Top graph shows the results for the circular tripwire at $Re_d = 2.8 \times 10^3$, middle shows the results for the square tripwire at $Re_d = 2.8 \times 10^3$, and bottom shows the results for the diamond-shaped tripwire at $Re_d = 2.8 \times 10^3$.

2.6 Conclusion

Heat transfer augmentation of a flat plate using circular, square and diamond-shaped tripwires was evaluated at two Reynolds numbers. The following observations have been made

1. The Nusselt number was observed to be lower than that of the un-tripped case in the near-wake of each tripwire due to the low streamwise velocity at near plate locations.

2. The Nusselt number increases after achieving the minimum value in the near-wake and terminates in a peak value. The location of this peak depends on the geometry of the tripwire as well as the Reynolds number. Recovery of streamwise velocity at near plate locations is partially responsible for the increase in Nusselt number, even though the turbulence intensity near the plate is higher.

3. Moving farther downstream beyond the peak, the normalized Nusselt number decreases due to a relative decrease in wall-normal velocity. In this region turbulence intensity play a more dominant role in improving heat transfer from the plate.

4. The circular tripwire produced the highest Nusselt number in the near-wake region. In the far-wake region, the Nusselt number started to deteriorate at a closer downstream location compared to other shapes. Among the tested geometries, the boundary layer behind the circular tripwire transitions into an attached turbulent one at a closer downstream location. It also generated the lowest turbulence intensity. The overall effect of the circular tripwire is the lowest among the tested geometries.

5. The square tripwire generated the most consistently improved Nusselt number compared to the tested case. The boundary layer reattachment is delayed until x/d = 50. The increased turbulence in the far-wake improves the intermixing near the plate thus promoting heat transfer from the plate. The cooling effect in the far-wake decays much slower than that of the circular tripwire. It also generated the highest magnitude turbulence downstream among the tested geometries.

6. The diamond-shaped tripwire produced the worst heat transfer augmentation in the near-wake due to the greater velocity deficit created by the diamond shape. The

flow reattaches after 30 diameters downstream, which is the longest among the tested geometries. Downstream, it produced the highest peak Nusselt number. Decay in the Nusselt number in the far-wake did not occur, and the shape factor of the boundary layer at the farthest measured downstream location was higher than 1.4.

Acknowledgements

References

[1]   P.W. Bearman, M. Zdravkovich, Flow around a circular cylinder near a plane boundary, J. Fluid Mech. 89 (1978) 33–47. doi:10.1017/S002211207800244X.

[2]   K. Ryu, S. Yook, K. Lee, Forced convection across a locally heated square cylinder near a wall, Numer. Heat Transf. Part A Appl. 65 (2014) 972–986. doi:10.1080/10407782.2013.850930.

[3]   H. Hu, M. Koochesfahani, Molecular tagging velocimetry and thermometry and its application to the wake of a heated circular cylinder, Meas. Sci. Technol. 17 (2006) 1269–1281. doi:10.1088/0957-0233/17/6/S06.

[4]   L. Wang, B. Sundén, Experimental investigation of local heat transfer in a square duct with continuous and truncated ribs, Exp. Heat Transf. 18 (2005) 179–197. doi:10.1080/08916150590953397.

[5]   S. Price, D. Sumner, J. Smith, K. Leong, M. Païdoussis, Flow visualization around a circular cylinder near to a plane wall, J. Fluids Struct. 16 (2002) 175–191. doi:10.1006/jfls.2001.0413.

[6]   M.S. Akoz, Flow structures downstream of the horizontal cylinder laid on a plane surface, Proc. Inst. Mech. Eng. Part C J. Mech. Eng. Sci. 223 (2009) 397–413. doi:10.1243/09544062JMES1111.

[7]   G.-S. He, J.-J. Wang, C. Pan, L.-H. Feng, Q. Gao, A. Rinoshika, Vortex dynamics for flow over a circular cylinder in proximity to a wall, J. Fluid Mech. 812 (2017) 698–720. doi:10.1017/jfm.2016.812.

[8]   A. Sharma, V. Eswaran, Heat and fluid flow across a square cylinder in the two-dimensional laminar flow regime, Numer. Heat Transf. Part A Appl. 45 (2004) 247–269. doi:10.1080/10407780490278562.

[9]   F. Fouladi, P. Henshaw, D.S.-K. Ting, S. Ray, Flat plate convection heat transfer enhancement via a square rib, Int. J. Heat Mass Transf. 104 (2017) 1202–1216. doi:10.1016/j.ijheatmasstransfer.2016.09.023.

[10]   T.-M. Liou, Y. Chang, D.-W. Hwang, Experimental and computational study of turbulent flows in a channel with two pairs of turbulence promoters in tandem, J. Fluids Eng. 112 (1990) 302. doi:10.1115/1.2909405.

[11]   Y.Z. Liu, F. Ke, H.J. Sung, Unsteady separated and reattaching turbulent flow over a two-dimensional square rib, J. Fluids Struct. 24 (2008) 366–381. doi:10.1016/j.jfluidstructs.2007.08.009.

[12]   S. Bayraktar, S. Yayla, A. Oztekin, H. Ma, Wall proximity effects on flow over cylinders with different cross sections, Can. J. Phys. 92 (2014) 1141–1148. doi:10.1139/cjp-2013-0692.

[13]   R. Kamali, A.R. Binesh, The importance of rib shape effects on the local heat transfer and flow friction characteristics of square ducts with ribbed internal surfaces, Int. Commun. Heat Mass Transf. 35 (2008) 1032–1040. doi:10.1016/j.icheatmasstransfer.2008.04.012.

[14]   J. Liu, S. Hussain, J. Wang, L. Wang, G. Xie, B. Sundén, Heat transfer enhancement and turbulent flow in a high aspect ratio channel (4:1) with ribs of various truncation types and arrangements, Int. J. Therm. Sci. 123 (2018) 99–116. doi:10.1016/j.ijthermalsci.2017.09.013.

41

[15]   A. Yadav, J. Bhagoria, A numerical investigation of square sectioned transverse rib roughened solar air heater, Int. J. Therm. Sci. 79 (2014) 111–131. doi:10.1016/j.ijthermalsci.2014.01.008.

[16]   S. Alfarawi, S.A. Abdel-Moneim, A. Bodalal, Experimental investigations of heat transfer enhancement from rectangular duct roughened by hybrid ribs, Int. J. Therm. Sci. 118 (2017) 123–138. doi:10.1016/j.ijthermalsci.2017.04.017.

[17]   T. Cebeci, G.J. Mosinskis, A.M.O. Smith, Calculation of Separation Points in Incompressible Turbulent Flows, J. Aircr. 9 (1972) 618–624. doi:10.2514/3.59049.

[18]   H. Schlichting, K. Gersten, Boundary-Layer Theory, 9th ed., Springer Berlin Heidelberg, Berlin, Heidelberg, 2017. doi:10.1007/978-3-662-52919-5.

[19]   A. Tariq, P.K. Panigrahi, K. Muralidhar, Flow and heat transfer in the wake of a surface-mounted rib with a slit, Exp. Fluids. 37 (2004) 701–719. doi:10.1007/s00348-004-0861-8.

[20]   M. Ali, A. Tariq, B. Gandhi, Flow and heat transfer investigation behind trapezoidal rib using PIV and LCT measurements, Exp. Fluids. 54 (2013) 1520. doi:10.1007/s00348-013-1520-8.

[21]   S. Acharya, S. Dutta, T.A. Myrum, R.S. Baker, Turbulent flow past a surface-mounted two-dimensional rib, J. Fluids Eng. 116 (1994) 238. doi:10.1115/1.2910261.

CHAPTER 3

ON FLAT PLATE HEAT CONVECTION DOWNSTREAM OF A DIAMOND-SHAPE TRIPWIRE AT VARYING GAP

Nomenclature

d = Diameter of the tripwire

G = Distance between the bottom of the tripwire and the top of plate

h = Heat transfer coefficient

K_{PTFE} = Thermal conductivity of PTFE

K_{air} = Thermal conductivity of air

Nu = Nusselt number

Nu_o = Base Nusselt number without tripwire

PTFE = Polytetrafluoroethylene

Re_d = Reynolds number based on the diameter of the tripwire

Re_x = Reynolds number based on the distance from the leading edge

St = Strouhal number

T_{air} = Temperature of the ambient air

T_{bottom} = Temperature of the bottom surface of PTFE plate

T_{top} = Temperature of the top surface of the PTFE plate

$T_{top,o}$ = Temperature of top surface of the PTFE surface without tripwire

$\bar{U}$ = Time averaged velocity

U_∞ = Free stream velocity

u_{rms} = Friction or fluctuating velocity

x = Downstream distance from the leading edge of the plate

z = Wall-normal distance from the plate surface

δ = Disturbance or 99% × U_∞ boundary layer

ν = Kinematic viscosity

■ Introduction

Heat transfer from a flat plate has garnered much attention due to its application in engineering solutions. A common method to promote heat transfer from a flat surface is to increase surface roughness either randomly with sand grain or by disturbing and discouraging the formation of a laminar boundary layer with a two-dimensional roughness element such as a tripwire. When a tripwire is placed without any gap on a flat surface, the flow separates from the tripwire, forming a separation bubble behind it. The flow velocity inside the separation bubble is very slow, discouraging heat transfer [1–5]. At the termination of this separation bubble, where the flow reattaches itself to the wall, small-scale vortices are generated. These vortices have been proven to improve heat transfer from the plate [6]. In the far-wake of a tripwire placed on a flat surface, the boundary layer becomes turbulent and thus much more conducive to heat transfer. Therefore, a tripwire not only acts as a vortex generator but also as a turbulator. Some important observations regarding heat transfer augmentation by a tripwire are presented in Table 3.1.

The geometry and arrangement of the tripwire have been extensively altered to manipulate the flow structure and improve the rate of heat transfer. Geometries such as a circle [1,7], semicircle [8], rectangle [9], square [10,11], triangle [12], wedge [13] and trapezoid [12] have all been shown to increase heat transfer from a flat plate. In addition, parameters such as width [3], aspect ratio [14], placement angle with respect to flow [15,16], effect of pitch length between tandem tripwires [15,17–19] and impact of a built-in centrally located slit

with various open area ratios [9] have been investigated and demonstrated to provide better Nusselt number readings for limited applications (i.e. this solution is limited to applications where the ribs do not interfere with the function of the plate they are installed on).

As Table 3.1 shows, little attention has been given to the heat transfer and flow mechanics behind a diamond-shaped tripwire. In the current study, heat transfer augmentation from a flat plate through a diamond-shaped tripwire is investigated in order to assess the impact of gap ratio on heat transfer. The heat transfer from six gap ratios (G/d = 0.3, 1.3, 2.3, 3.3, 4.3 and 5.5) at a Reynolds number of 1.6×10^3 was quantified using a thermal camera. The flow behind each case was further measured using an X-probe hotwire at five downstream locations to elucidate the flow mechanics.

Table 3.1 Main findings of the highlighted studies. d = diameter of tripwire, FV = flow visualization experiment, G = tripwire–wall gap, HW = hot wire and/or hot film analysis, LCT = liquid crystal thermaography, LDV = laser doppler velocimetry, p = pitch length between two tripwires, PIV = particle image velocimetry, PM = pressure measurements, r = tripwire radius, Re = Reynolds number, TM = temperature measurements, x = downstream distance from the tripwire.

Geometry	Parameter	Reference	Experiment Details	Main Findings
Semi-circle	Pitch ratio	Alfarawi et al. [8]	$G/d = 0$, $Red = 1.3 \times 104 \sim 8.7 \times 104$	At a lower pitch-to-height ratio (p/r), the separation region occupies a larger area. As the Reynolds number increases, heat transfer improvement decreases. The optimum p/r is 13.3.
Circle	Gap ratio	Marumo et al. [1]	$G/d = 0 \sim 3.69$, $Red = 8.0 \times 103$	At $G/d = 0$, flow separation produces an adverse heat transfer region behind the tripwire. As a gap is introduced between the tripwire and plate, a higher Nusselt number is observed in the near wake.
	Reynolds number	Akoz [20]	$G/d = 0$, $Red = 1.0 \times 103 \sim 7.0 \times 104$	There are two separation regions; the primary region is at 9d ~ 10d downstream, and the secondary is at 0.73d ~ 1.2d. The separation point moves downstream with increasing Red. The separated flow from the second separation bubble moves towards the tripwire, and before reaching it, the flow curls up and causes a vortex to form in the near wake. The structure of the wake changes with Red.
	Gap ratio	Price et al. [21]	$G/d = 0 \sim 2$, $Red = 1.2 \times 103 \sim 4.9 \times 103$	No gap flow occurs and a strong shear layer moves away from the wall without rolling up into a vortex.

Square	Pitch ratio	Liou et al. [2]	$G/d = 0$, $Re_d = 4.2 \times 10^4$	When three pairs of tripwires are placed on the surface of a duct, "velocity overshoot" is observed at 0.5d on the top face of the square tripwire. Reattachment length depends on Re.
	Width of tripwire	Wang et al. [3]	$G/d = 0$, $Re_d = 8.0 \times 10^3 \sim 2.0 \times 10^4$	Local hot spots arise at the rear corner of the rib. A rapid increase in heat transfer occurs in the reattachment zone. Afterwards, the Nusselt number decays as the thermal boundary layer redevelops. The flow structure depends on the Re, and heat transfer augmentation becomes lower with increasing Re.
	Gap ratio and Reynolds number	Ryu et al. [10]	$G/d = 0.25 \sim 3$, $Re_d = 10$ and 5.0×10^4	Flow regime = f(Re, G/d). As G/d increases, the gap flow becomes stronger, leading to vortex shedding. As Re increases, fluid is separated from the top and bottom surfaces of the tripwire.
	V, W and M configurations	Ravi et al. [22]	$G/d = 0$, $Re_d = 2.0 \times 10^4 \sim 7.0 \times 10^4$	A V configuration produced twin vortices. Heat transfer is reduced near the front-facing apex (center of the plate) and increases toward the side walls (in the Y direction). The backward-facing apex in W and M configurations produces a pair of counter-rotating vortices that do not merge together. Due to reduced mixing, low Nusselt numbers are observed behind this type of apex.
Diamond	Gap ratio	Bayraktar et al. [23]	$G/d = 0.1 \sim 0.8$, $Re_d = 2.0 \times 10^4$	Two recirculation zones form behind the diamond-shaped tripwire at the smallest gap ratio. Increasing the G/d ratio gives rise to vortices of different sizes that merge together at $G/d = 0.8$.

				The highest St value is observed for the circular tripwire, and the next highest is observed for the diamond-shaped tripwire.
Triangle	Pitch	Kamali and Binesh [12]	$G/d = 0$, $Red = 8.0 \times 103 \sim 2.0 \times 104$	The Nu/Nuo trends for square and triangular ribs are very similar. However, the recirculation zone for a triangular tripwire has a slightly higher peak Nu/Nuo. As Re increases, the Nusselt number decreases.
	Staggered and in-line configurations	Promvonge and Thianpong [13]	$G/d = 0$, $Red = 4.0 \times 103 \sim 1.6 \times 104$	The inline triangular tripwires enhance heat transfer more than the rectangular tripwires. Increasing the Reynolds number had little effect on the Nusselt number.
Trapezoid	Pitch	Kamali and Binesh [12]	$G/d = 0$, $Red = 8.0 \times 103 \sim 2.0 \times 104$	A trapezoidal tripwire facing downstream (decreasing height) improves overall heat transfer more than an upstream-facing (increasing height) tripwire. Separation from the downstream-facing tripwire is also smaller. As Re increases, the Nusselt number decreases.
Wedge	Staggered and in-line configurations	Promvonge and Thianpong [13]	$G/d = 0$, $Red = 4.0 \times 103 \sim 1.6 \times 104$	Of a variety of tripwires arranged in staggered and inline configurations, the downstream wedge tripwire produces the best results. Inline configurations produce better results. Higher Nusselt numbers are accompanied by higher drops in pressure.

■ Experimental Setup

In this experiment, a square tripwire with a 0.5 cm by 0.5 cm cross section was rotated 45°
to create a diamond-shaped tripwire. The flow data was analyzed at five downstream
locations (x/d = 10, 20, 30, 40 and 50). The hotwire data was not modified to address the
directional insensitivity of hotwire. At each x/d location, the data was acquired from z/d =
0.6 ~ 12 at intervals of 0.2. The centre of the tripwire was positioned at six heights. The
gap ratios for each height are presented in Table 3.2. Experimental setup is shown in Figure
3.1. Before acquiring flow data, the existing boundary of the wind tunnel base without any
flow augmentation was evaluated. The boundary layer was approximately 2.5 cm thick
where the tripwire was placed. The normalized streamwise velocity and turbulence
intensity profiles of the smooth plate are shown in Figure 3.2
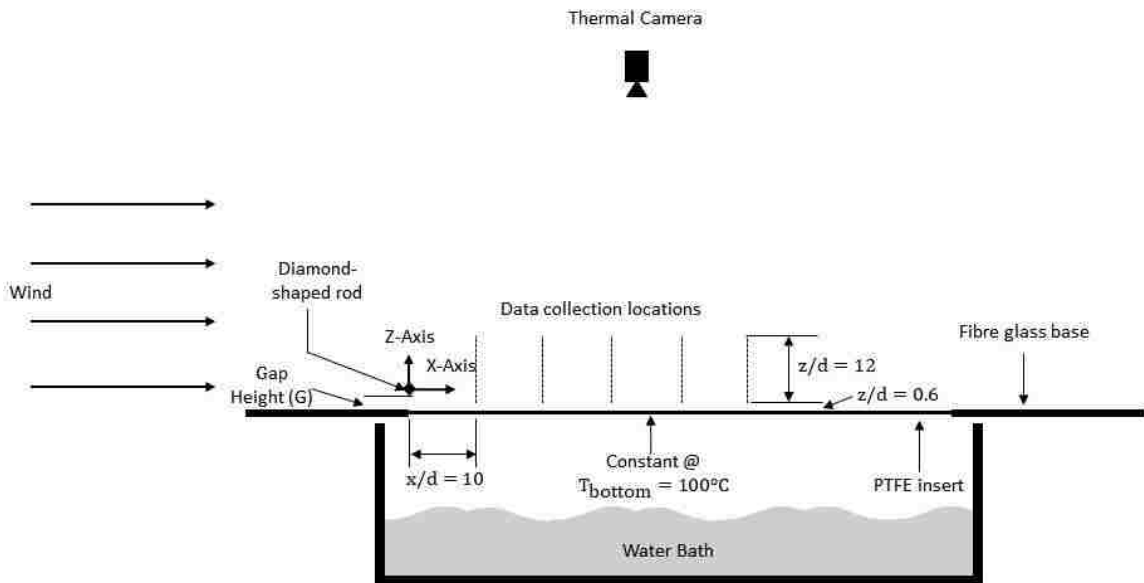
Figure 3.1 Experimental setup showing the placement of the tripwire and data acquisition points.

Table 3.2 Details about the tested gap ratio.

G/d	G/ δ
0.3	0.06
1.3	0.25
2.3	0.44
3.3	0.63
4.3	0.83
5.3	1.02
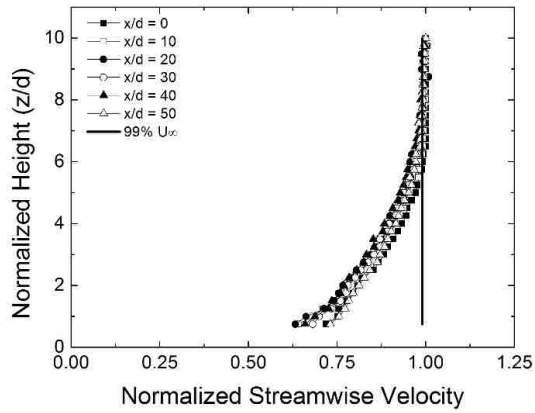
(a)
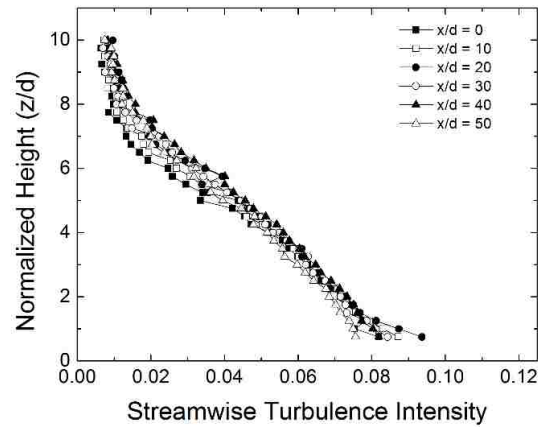
(b)

Figure 3.2 Smooth plate streamwise (a) normalized velocity and (b) turbulence intensity.

The Reynolds numbers based on diameter (Re_d) and downstream distance (Re_x) for each test case are presented in Table 3.3.

The uncertainties associated with each flow parameter are shown in Table 3.4.

Table 3.3 Test matrix presenting studied Reynolds numbers and downstream distances.

Re_d $\diagdown$ Re_x x/d	10	20	30	40	50
1.6×10^3	1.6×10^5	3.2×10^5	4.8×10^5	6.4×10^5	7.9×10^5

Table 3.4 Experimental uncertainties associated with each parameter.

Parameter	$\dfrac{Nu}{Nu_o}$	$\dfrac{\bar{U}}{U_\infty}$	$\dfrac{u_{rms}}{U_\infty}$	$\dfrac{\bar{W}}{U_\infty}$	$\dfrac{w_{rms}}{U_\infty}$	$\left|\dfrac{u \cdot w}{U_\infty{}^2}\right|$
Uncertainty	5%	3%	15%	8%	16%	22%

■ Results and Discussion

3.3.1 Heat Transfer Results

The two-dimensional distribution of the heat transfer results is shown in Figure 3.3, while Figure 3.4 shows the spanwise-averaged results. The results were normalized using the Nusselt number for the smooth plate at the appropriate Reynolds number. The two-dimensional distribution clearly indicates that the vortices interacted with the wall. As the vortices decrease in size, they cool a smaller region downstream. Varying the gap significantly changes the local heat transfer rate. The complex interaction between the shear layers from the plate and the two edges of the tripwire, which leads to suppression or shedding of the von Kármán vortices is responsible for the different heat transfer rates. In addition, G/d = 0.3 generates a higher Nu/Nu$_o$ over a greater normalized distance. However, the heat transfer rate in the near-wake is considerably lower than that of the smooth plate. The flow parameters indicate that vortex shedding was suppressed at this gap height. The role of each flow parameter in heat transfer will be discussed later.

As the gap ratio is increased to 1.3, Nu/Nu_o in the near-wake increases considerably. In addition, the spanwise heat transfer rate is about 1.7 times higher than that of the smooth plate. However, moving downstream, this heat transfer augmentation slowly fades away. The Nusselt number for this gap ratio decreases below one, reaching a minimum Nu/Nu_o of 0.85 at $x/d = 40$. Afterwards, the heat transfer rate slowly increases to that of the smooth plate.
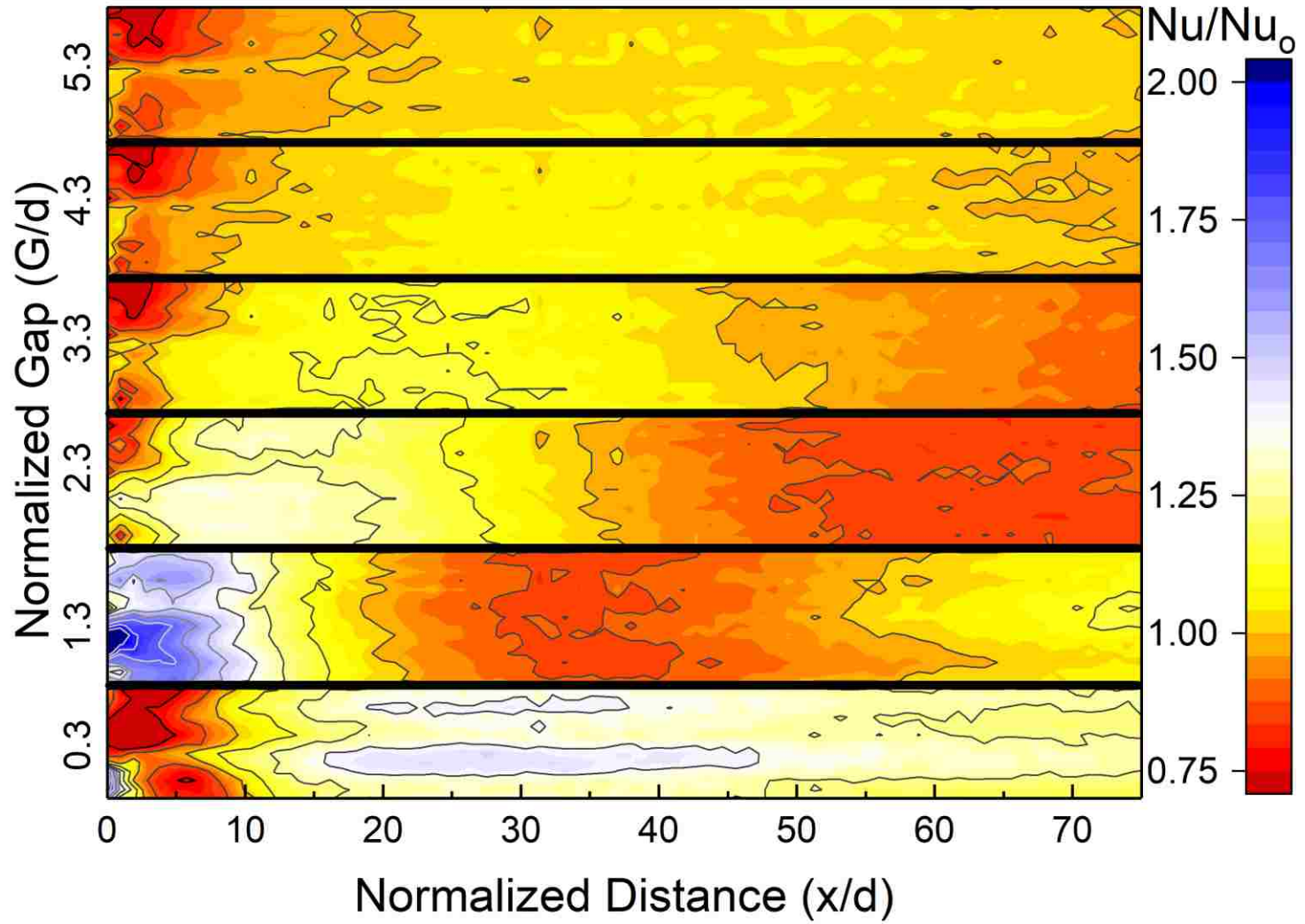
Figure 3.3 Normalized Nusselt number plots.
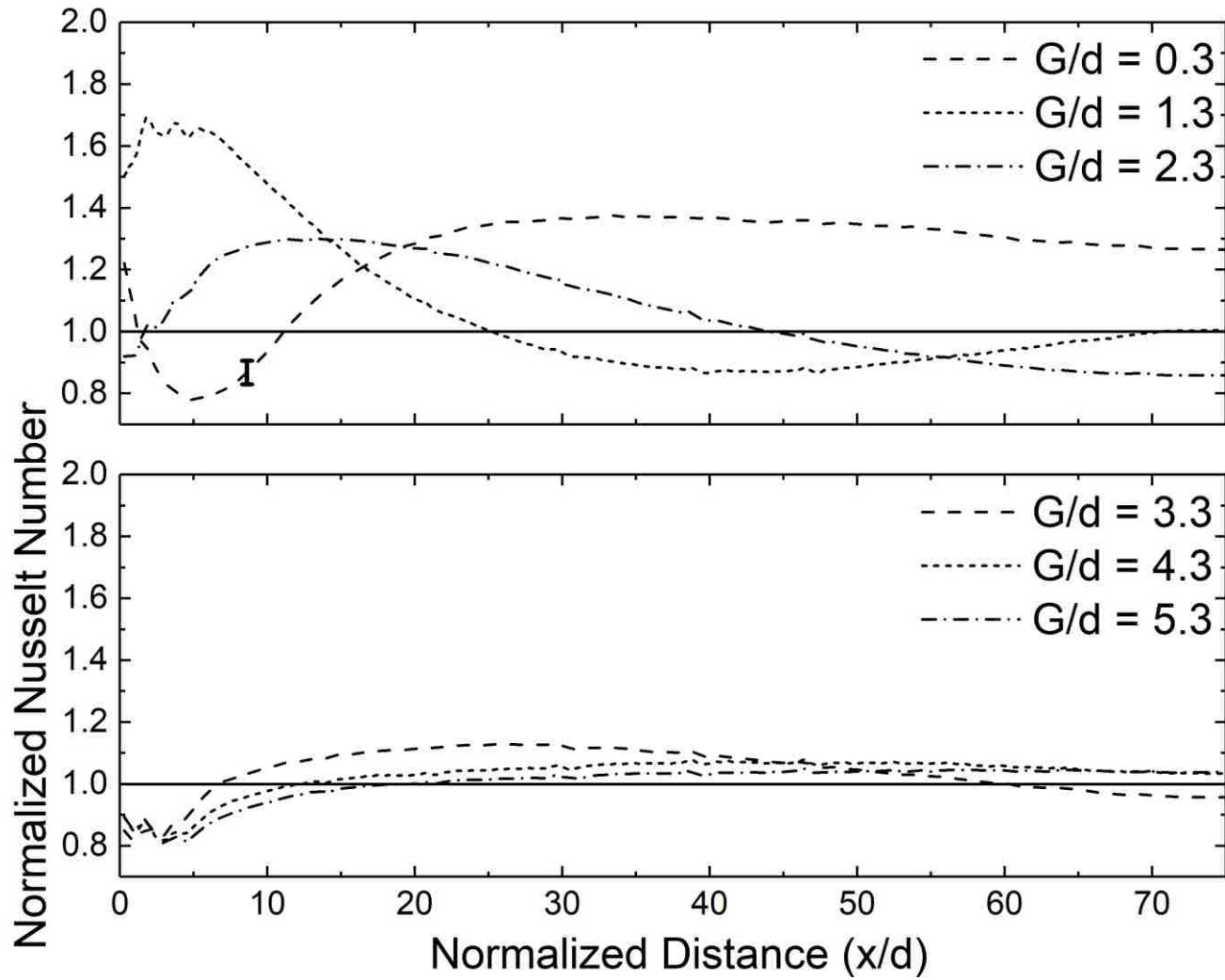
Figure 3.4 Span-averaged normalized Nusselt number.

At a height of G/d = 2.3, the Nusselt number started below 1, increasing to a peak of 1.3 at x/d = 9. Afterwards, it continued to decrease, falling below that of the smooth wall at around x/d = 40. The results for G/d > 2.3 showed that the tripwire does not significantly affect heat transfer. The Nusselt number was almost consistent throughout the span of the wall. In other words, the wake generated by the tripwire does not disturb the flow near the plate.

3.3.2   Discussion of Flow Structure

Flow structure can help us better understand heat transfer trends. The evolution of flow behaviour and the interaction of the shear layer from the plate and the two shoulders of the tripwire are discussed in detail for each normalized gap height. The shaded region in the graphs for each flow parameter indicates the presence of a dominant peak in spectral density. Due to space constraints, a select few sample graphs from selected locations are presented in Figure 3.6.

He et al. [24] found that, as G/d increased from 0, the jet-like flow coming from between a circular tripwire and the wall separated the shear layers coming from the cylinder and the separation bubble attached on the wall. Similar results were obtained for a square tripwire. Huang et al. [25] discovered that the separation bubble behind the rod was attached to the wall below G/d = 0.5. A similar phenomenon can be proposed to occur in the case of G/d = 0.3 in the current study, a sketch of the flow structure is shown in Figure 3.5. As the flow comes into contact with the diamond-shaped tripwire, part of the flow goes over the top shoulder of the tripwire, creating a separation in the flow that reattaches itself further downstream. The other portion of the flow was deflected through the gap between the tripwire and flat plate, forming a jet-like flow. This jet-like flow then splits the separation bubble into two parts. One part is attached on the flat plate, the other one is behind the tripwire.

(a)   (b)
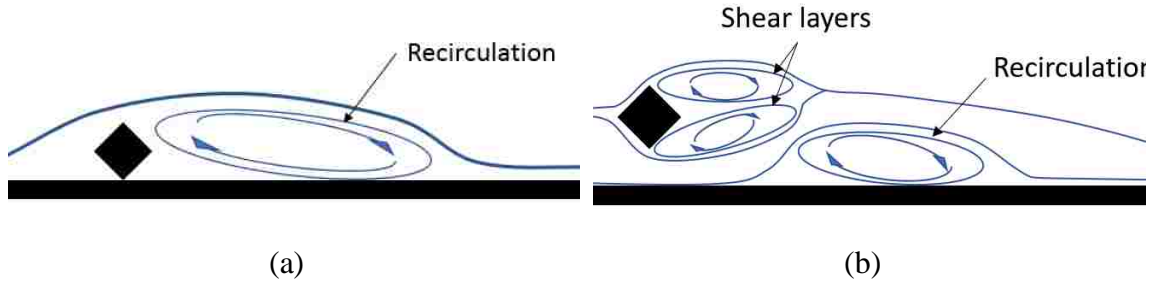
Figure 3.5 Sketch of flow regimes at (a) G/d = 0, and (b) G/d = 0.3.

(a)   (b)

(c)   (d)
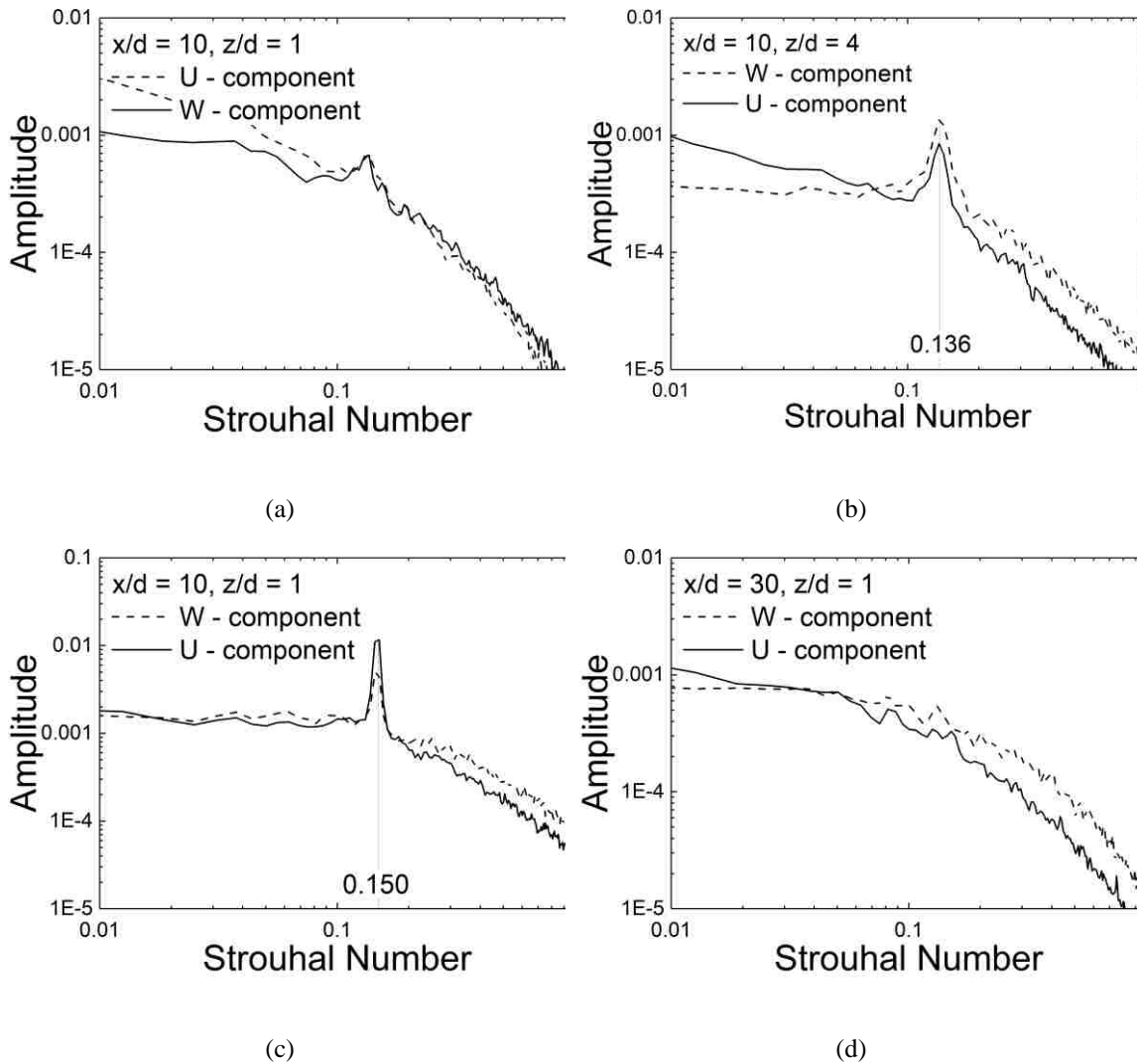
Figure 3.6 Sample spectral density plots for (a) G/d = 0.3, x/d = 10 and z/d = 1; (b) G/d = 0.3, x/d = 10 and z/d = 4; (c) G/d = 1.3, x/d = 10 and z/d = 1 and (d) G/d = 1.3, x/d = 30 and z/d = 1.

This suggest that the improvement in the Nusselt number in the near-wake occurred because the gap flow impinged on the flat plate. Moving downstream, the flow no longer impinged and the cooling process was reduced. The decrease in heat transfer in the near-wake of the tripwire was due to the separation bubble attached to the wall. In the current study, vortex shedding frequency came from the top shoulder of the tripwire, indicating that the shear layer was rolling up to form vortices. It can be theorized that the cooling process was adversely affected by the separation behind the tripwire but was marginally compensated by the vortices in the upper shear layer.

The velocity profiles (streamwise and wall-normal) at $x/d = 10$ and $G/d = 0.3$ showed a velocity-deficient region behind the tripwire. The streamwise velocity (Figure 3.7) in this region fell below 25% of the freestream velocity, producing high turbulence in the shear layer. The wall-normal velocity (Figure 3.8) profile not only experienced a deficit immediately behind the tripwire but also exhibited overshoot near the top shoulder of the tripwire. The shear in the wall-normal component produced higher turbulence than the streamwise component. Due to the high turbulence produced in the shear layer, the Nusselt number was observed to be marginally better than the undisturbed case. The Reynolds stresses (Figure 3.11) indicate that the shear layer from the bottom shoulder of the tripwire failed to form due to the interaction between the boundary layer, resulting in suppression of vortex shedding.
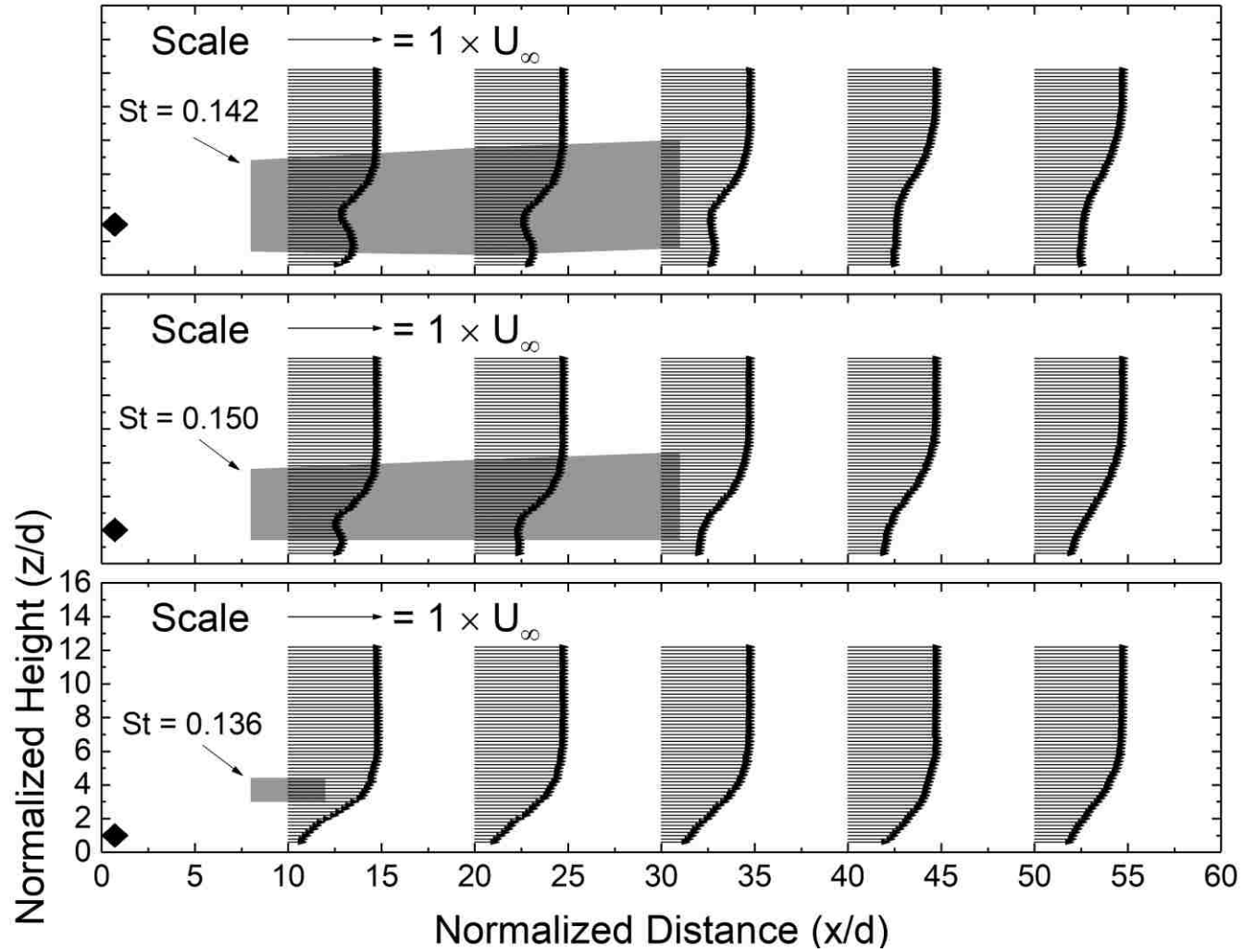
Figure 3.7 Normalized streamwise velocity. Top graph represents G/d = 2.3, middle represents G/d = 1.3 and bottom represents G/d = 0.3. Shaded portions indicate vortex shedding.
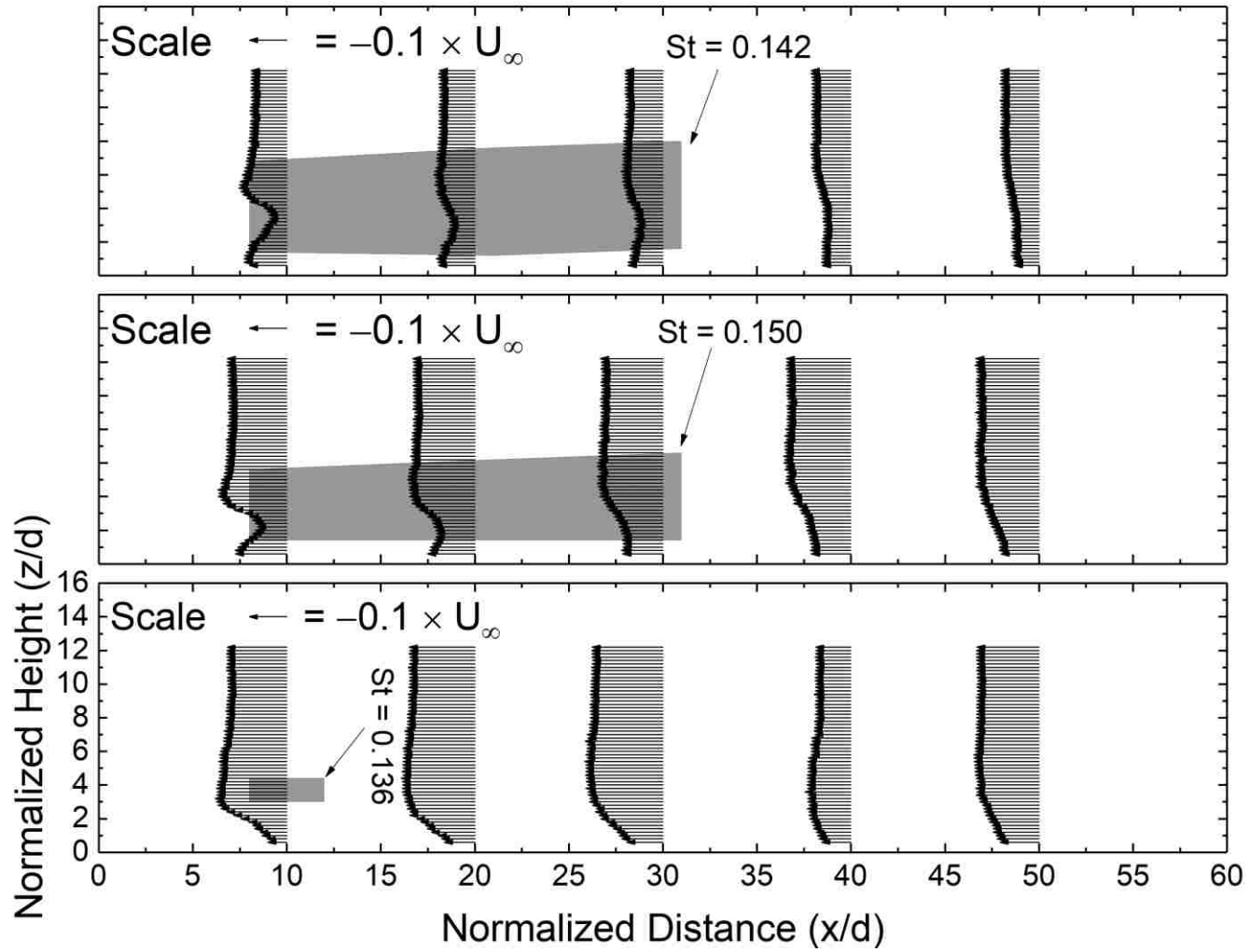
Figure 3.8 Normalized wall-normal velocity. Top graph represents G/d = 2.3, middle represents G/d = 1.3 and bottom represents G/d = 0.3. Shaded portions indicate vortex shedding.
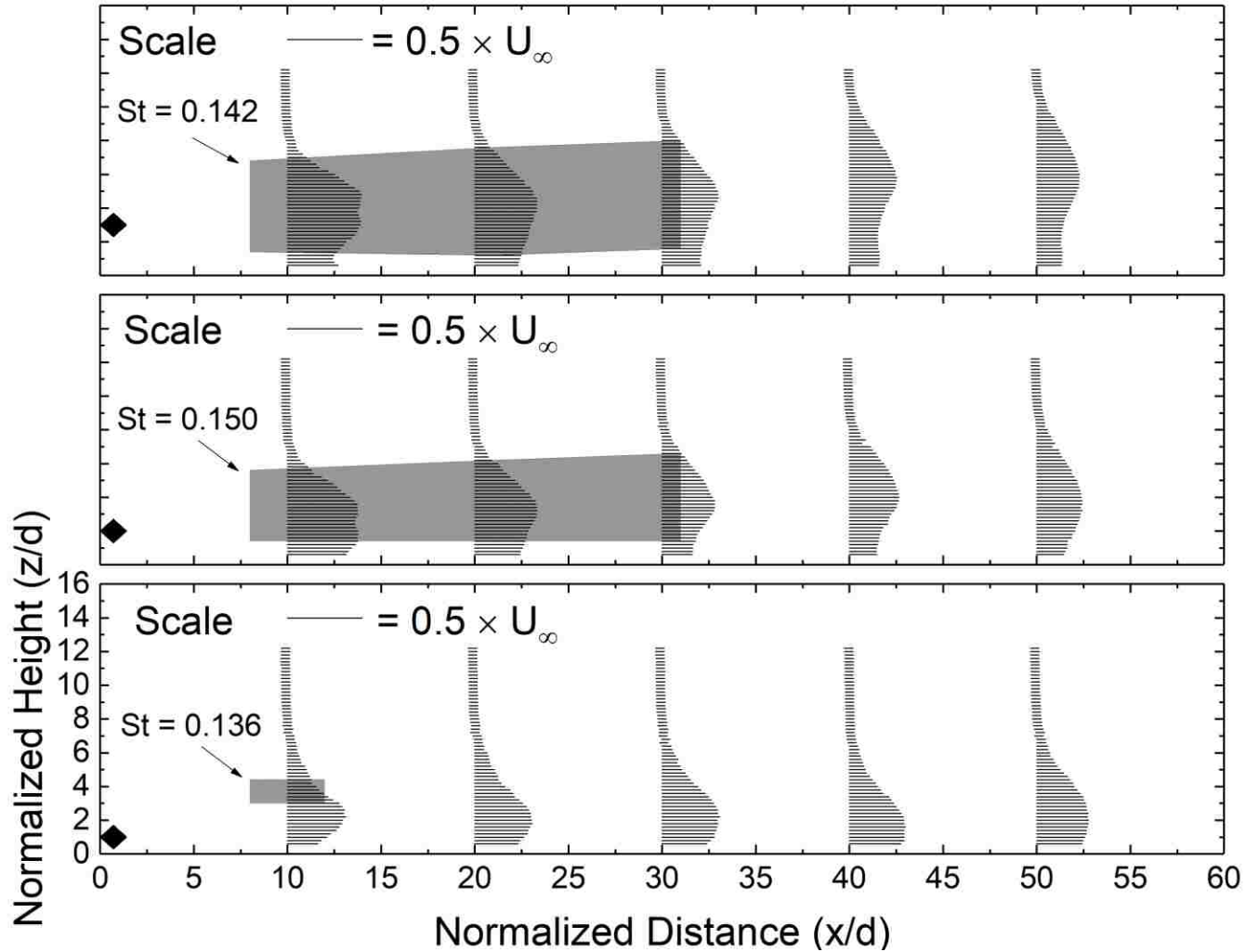
Figure 3.9 Streamwise turbulence intensity profiles. Top graph represents G/d = 2.3, middle represents G/d = 1.3 and bottom represents G/d = 0.3. Shaded portions indicate vortex shedding.
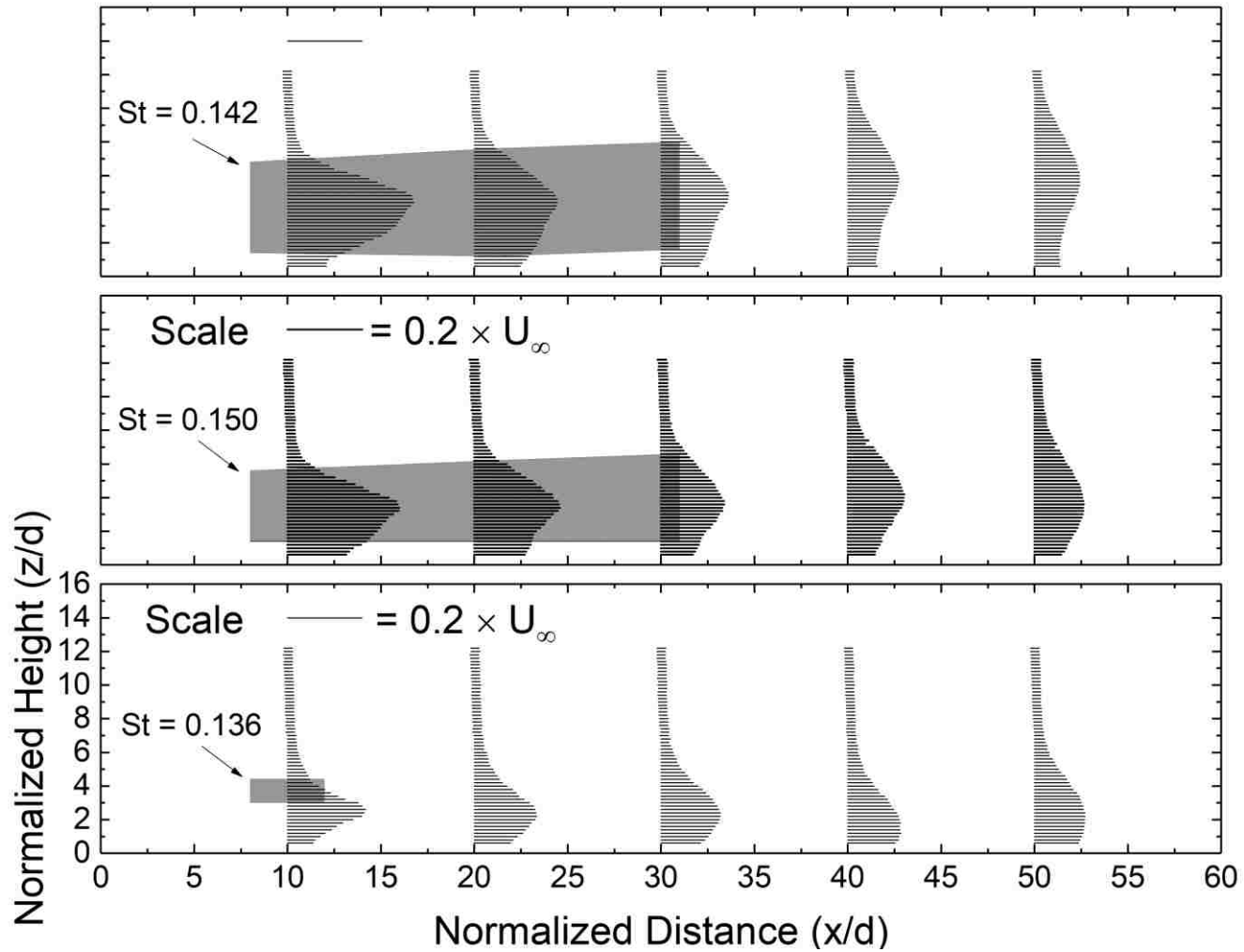
Figure 3.10 Wall-normal turbulence intensity plots. Top graph represents G/d = 2.3, middle represents G/d = 1.3 and bottom represents G/d = 0.3. Shaded portions indicate vortex shedding.
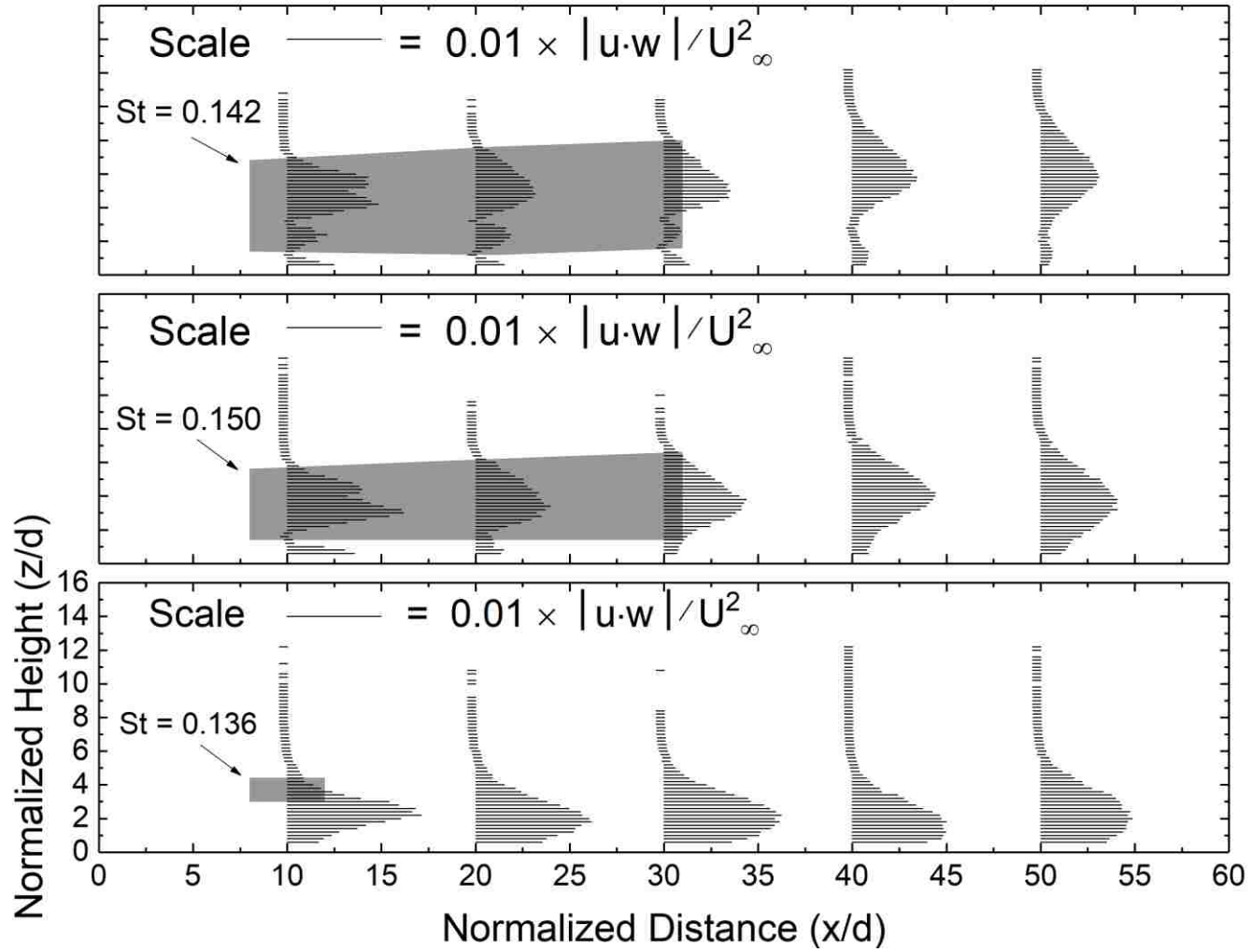
Figure 3.11 Absolute normalized Reynolds stress profiles. Top graph represents G/d = 2.3, middle represents G/d = 1.3 and bottom represents G/d = 0.3. Shaded portions indicate vortex shedding.

Moving downstream, the normalized Nusselt number increased to a maximum value of 1.3, presumably due to reattachment as the vortices observed at x/d = 10 were not measured as x/d increased from 10 to 20. The streamwise velocity near the wall was still below 50% of the freestream value for all measured locations as the thickness of the wake area increased, but the turbulence produced in the streamwise velocity decreased in strength.

The wall-normal velocity near the wall was also around 50% of the freestream value, but the velocity overshoot observed just above the upper shoulder of the tripwire at x/d = 10 remained a feature of wall-normal velocity, even at the location that was farthest downstream. As the wall-normal velocity near the wall recovered, more fluid was introduced towards the wall, increasing the Nusselt number. The turbulence in the wall-normal component slowly decayed as the boundary layer transitions into a turbulent boundary layer, similar to the streamwise component.

As the G/d ratio is increased from 0.3 to 1.3, a dominant vortex shedding frequency is observed in the vicinity of the top and bottom shoulders of the tripwire. In addition, streamwise velocity experienced a small peak near the wall. Turbulence (Figure 3.9) in this component had a symmetric profile on both sides of the centre of the tripwire. The Reynolds stresses at x/d = 10 also peaked near the wall. At x/d = 20, the weak velocity peak and symmetric turbulence intensity were lost. Wall-normal velocity was also higher near the wall, but the wall-normal turbulence intensity profile was asymmetric. These observations indicate that the bottom shoulder of the tripwire was producing a weaker shear layer that rolled up to form von Kármán vortices. The von Kármán vortices are the vortices shed from a cylinder placed in a fluid flow. In the current study, a dominant frequency observed in the spectral density plots (Figure 3.5) indicated the presence of the von Kármán vortices, while the non-dimensionalized Strouhal number represents the frequency of shedding of these vortices.

The von Kármán vortices were in close proximity to and interacted with the wall, causing heat to be transported away from the wall. Due to this interaction, the Nusselt number was greatly increased in the near-wake. At around x/d = 25, the Nusselt number falls below 1. In the same downstream region (i.e., x/d = 20 to 30), the peaks associated with the vortices were absent from the flow data (compare Figure 3.5 (c) and (d)).

A similar phenomenon was responsible for cooling at G/d = 2.3. Higher-frequency von Kármán vortices are observed until x/d = 20. However, weaker small-scale vortices are present at x/d = 30. A deficit in streamwise velocity occurred at a location higher away from the flat plate. In addition, a small peak was observed before the velocity deficit. However, this peak was observed for a longer distance downstream (i.e., until x/d = 30). The wall-normal velocity overshot (i.e. the local velocity magnitude was greater than that of the freestream velocity magnitude) from both the top and bottom shoulders of the tripwire. Velocity deficit still occurred behind the tripwire, and the velocity profiles at x/d = 40 still showed the remnants of the initial overshoot and deficit. All these factors worked together to positively augment heat transfer.

As the G/d ratio increased beyond 2.3, the von Kármán vortices and wake were generated higher above the wall. Thus, the vortices did not interact with the wall. Additionally, the streamwise velocity (Figure 3.12) and turbulence (Figure 3.14) near the top of the wall experienced less and less disturbance in the near and far wakes.

The wall-normal velocity (Figure 3.13) decreased in magnitude as G/d increased beyond 2.3, but overshoot from the shoulders still occurred. Similar to the streamwise velocity deficit, this wall-normal velocity overshoot followed the tripwire to a higher z/d location. The produced wall-normal turbulence (Figure 3.15) was also centred at a higher z/d location. The turbulence intensity near the wall, however, was around 0.075 at all the investigated locations, indicating a lack of disturbance. Due to the lack of flow

enhancement, the heat transfer at these gap ratios is very close to that of the smooth wall under experimental uncertainty.

Figure 3.17 compares the Strouhal number for various gap heights with those found in similar studies on circular and square tripwires. The Strouhal number at $G/d = 0.3$ coincides reasonably well with that found by Bayraktar [23]. It should be noted that Bayraktar performed their experiments at $G/d = 0.1, 0.2, 0.4$ and 0.8 and that their initial conditions do not indicate the presence of a boundary layer. As the gap ratio was increased from 0.3 to 1.3, the vortex shedding frequency increased slightly. There was a visible dip in the observed frequency at $G/d = 2.3$, after which it slowly recovered. Sheard et al. [26] observed a vortex shedding frequency of around 0.18 for a square tripwire rotated at 45º and placed in a freestream at a Reynolds number of 100. In the current experiments, the maximum observed value is St = 0.15 at $G/d = 5.3$, which is still far from the value of an isolated case. There are two main reasons for this discrepancy: the tripwire is still under the influence of the boundary layer, and vortex shedding frequency is dependent on the Reynolds number. According to Hwang et al. [25], the Strouhal number is lower when the thickness of the boundary layer increased from $\delta/d = 0.8$ to 5. However, the vortex shedding frequencies from both cases converged at a gap ratio of 5.5. Therefore, the fact that a smaller Strouhal numbers were observed in the current study is likely due to the existence of different Reynolds numbers.
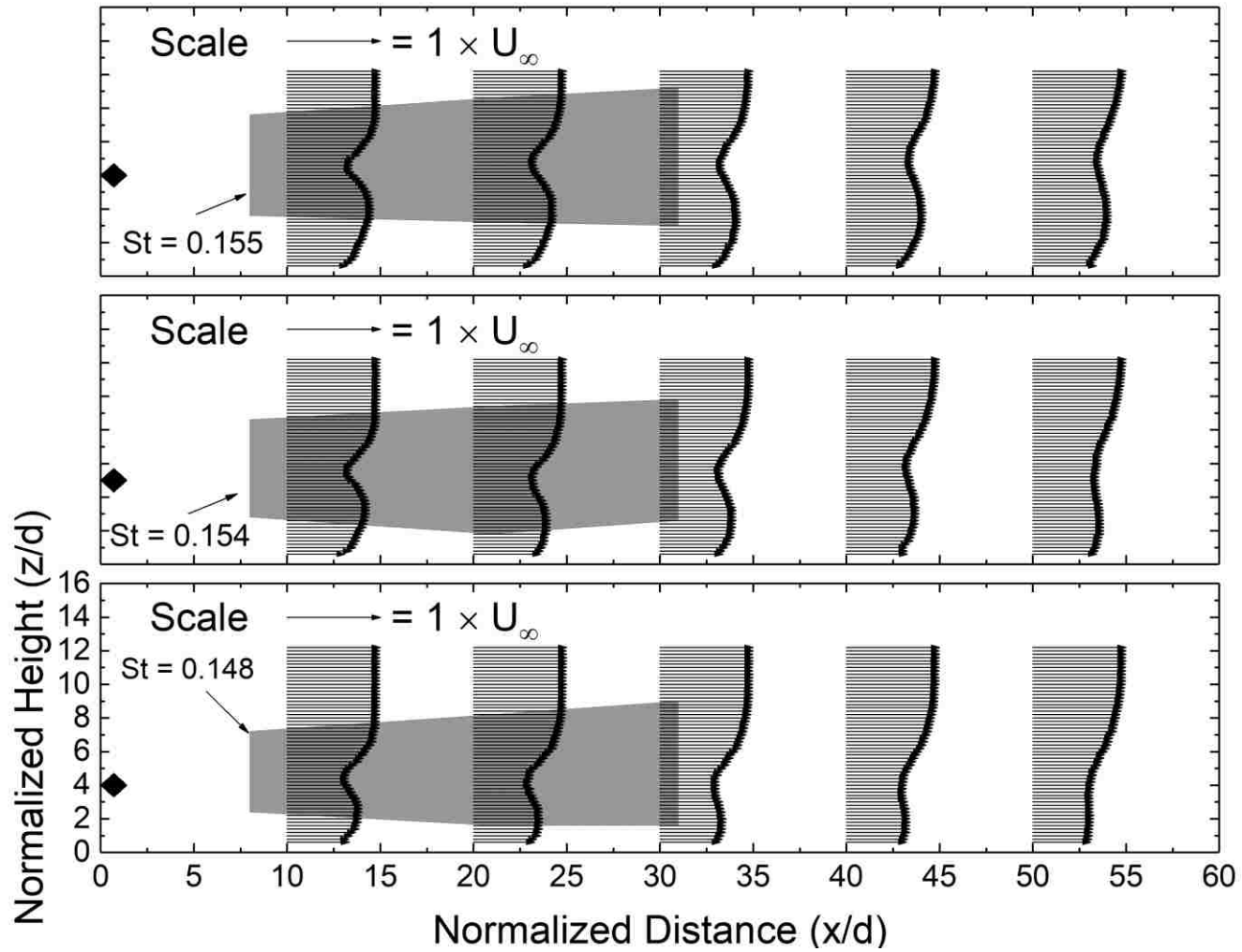
Figure 3.12 Normalized streamwise velocity. Top graph represents G/d = 5.3, middle represents G/d = 4.3 and bottom represents G/d = 3.3. Shaded portions indicate vortex shedding.
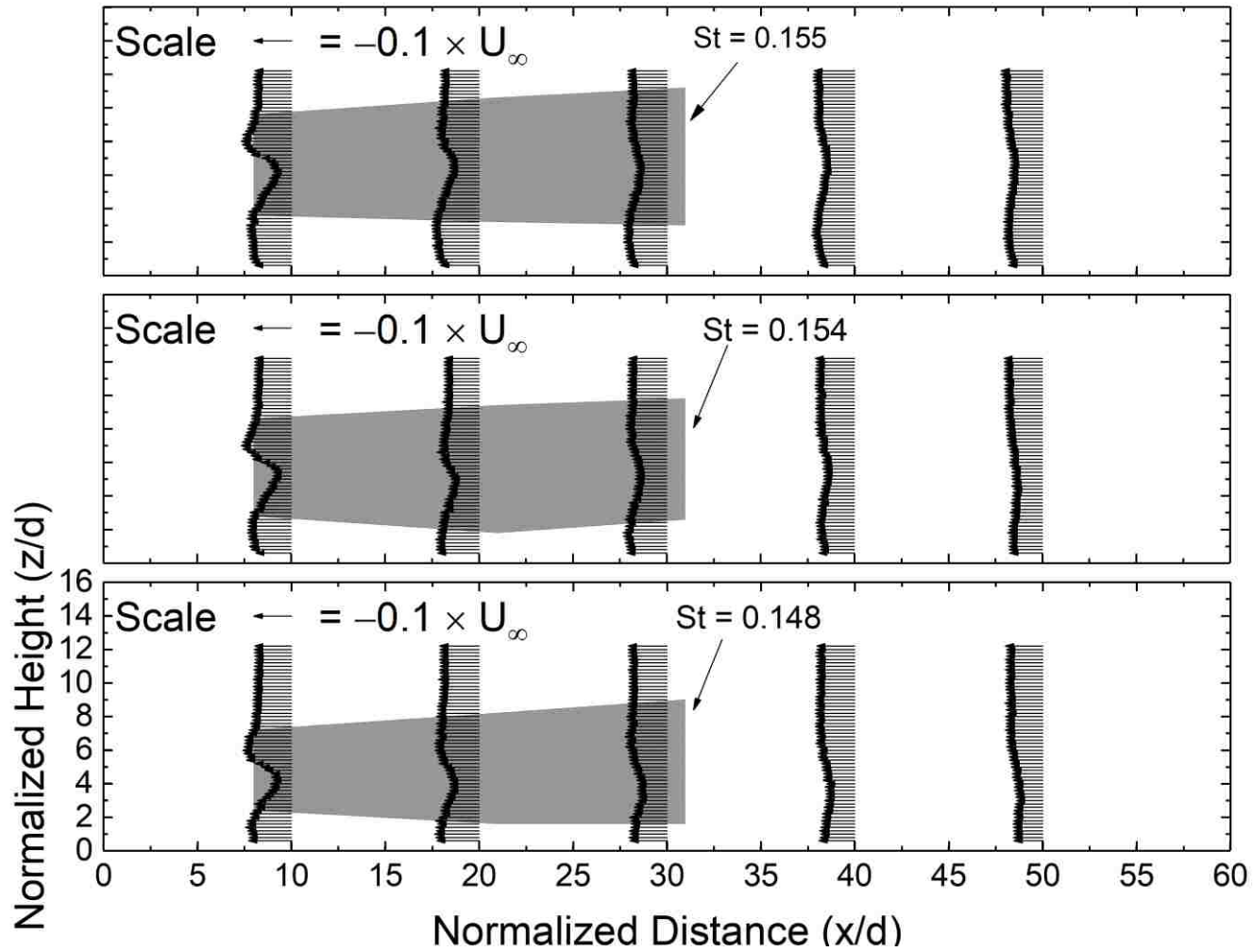
Figure 3.13 Normalized wall-normal velocity profiles. Top graph represents G/d = 5.3, middle represents G/d = 4.3 and bottom represents G/d = 3.3. Shaded portions indicate vortex shedding.
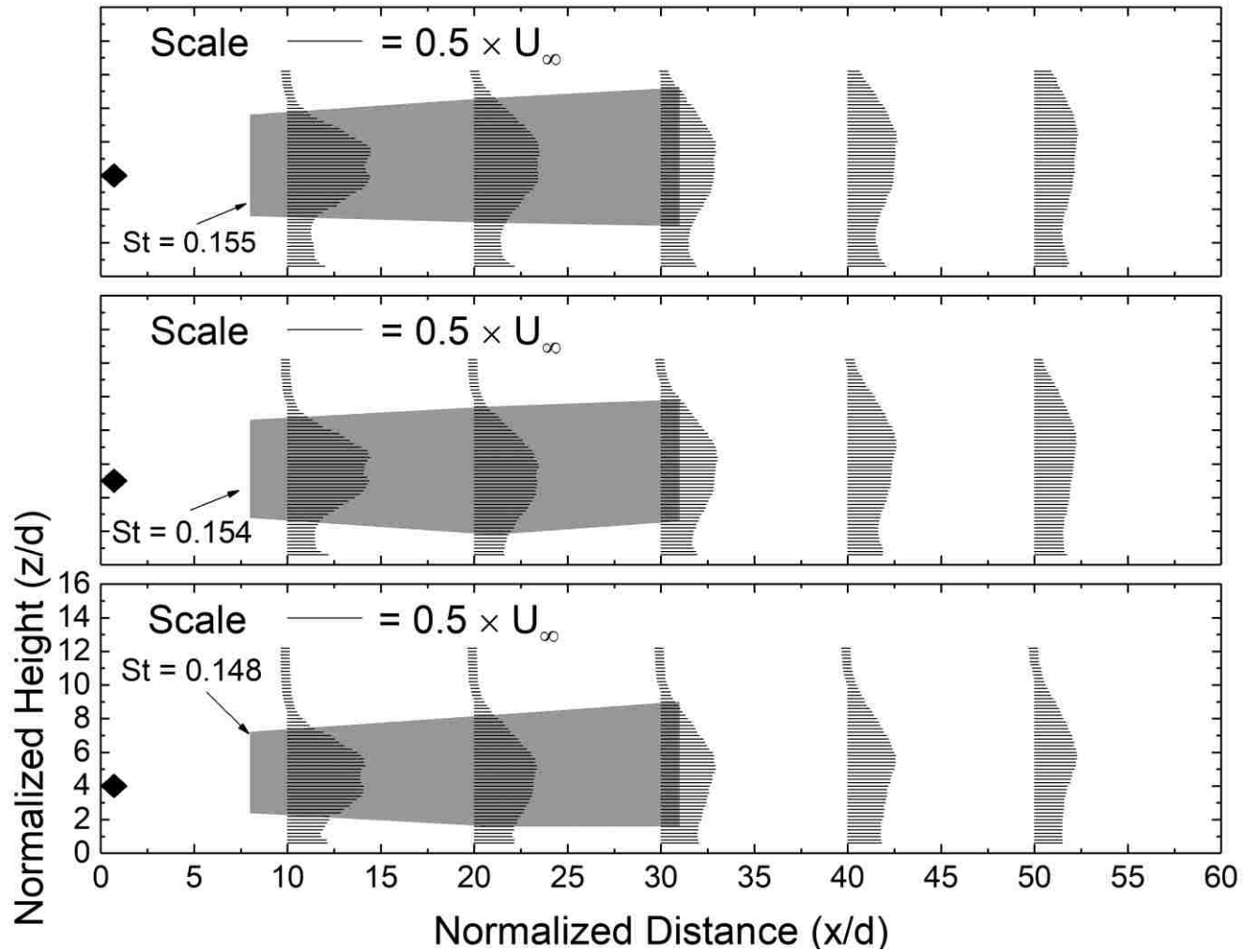
Figure 3.14 Streamwise turbulence intensity profiles. Top graph represents G/d = 5.3, middle represents G/d = 4.3 and bottom represents G/d = 3.3. Shaded portions indicate vortex shedding.
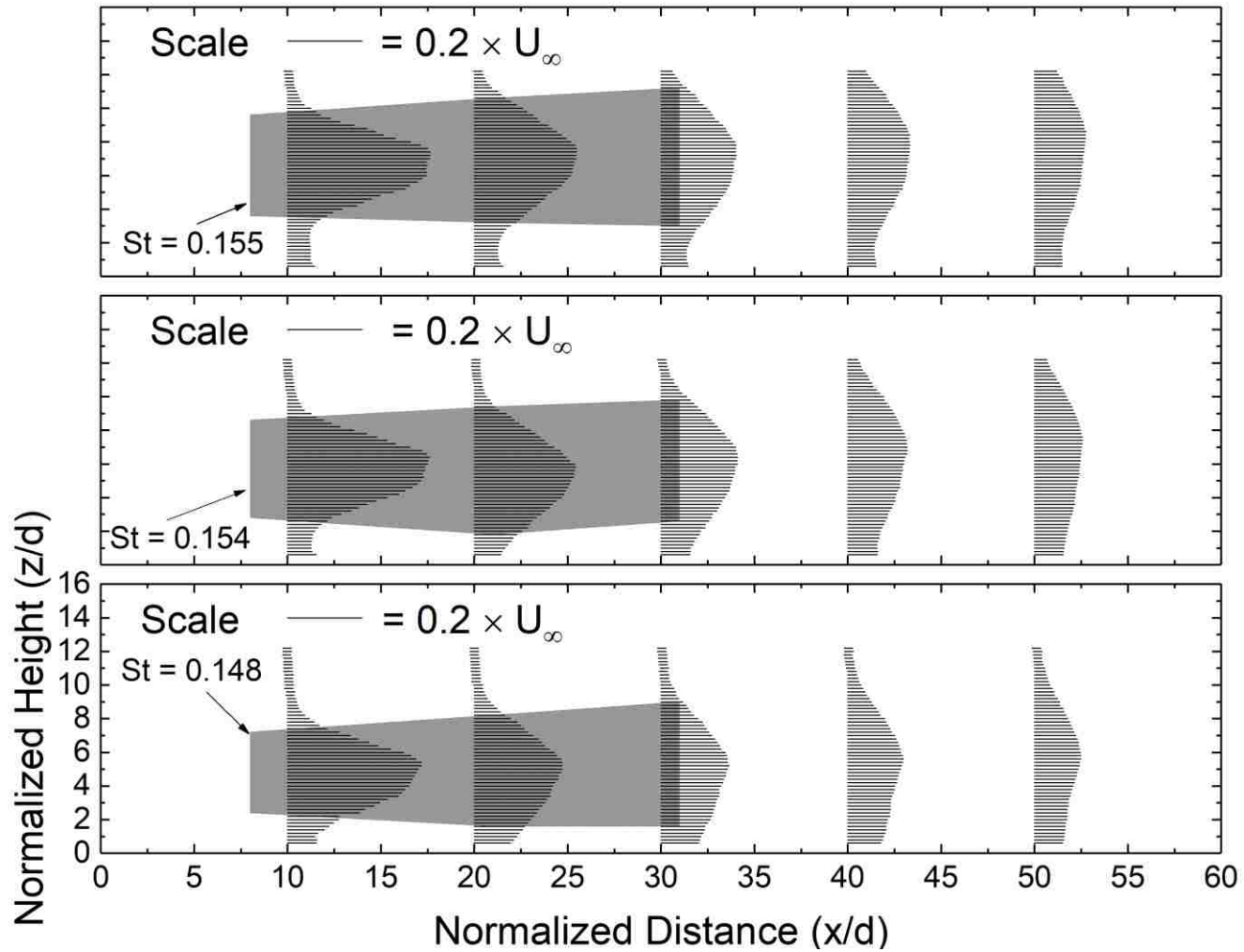
Figure 3.15 Wall-normal turbulence intensity profiles. Top graph represents G/d = 5.3, middle represents G/d = 4.3 and bottom represents G/d = 3.3. Shaded portions indicate vortex shedding.
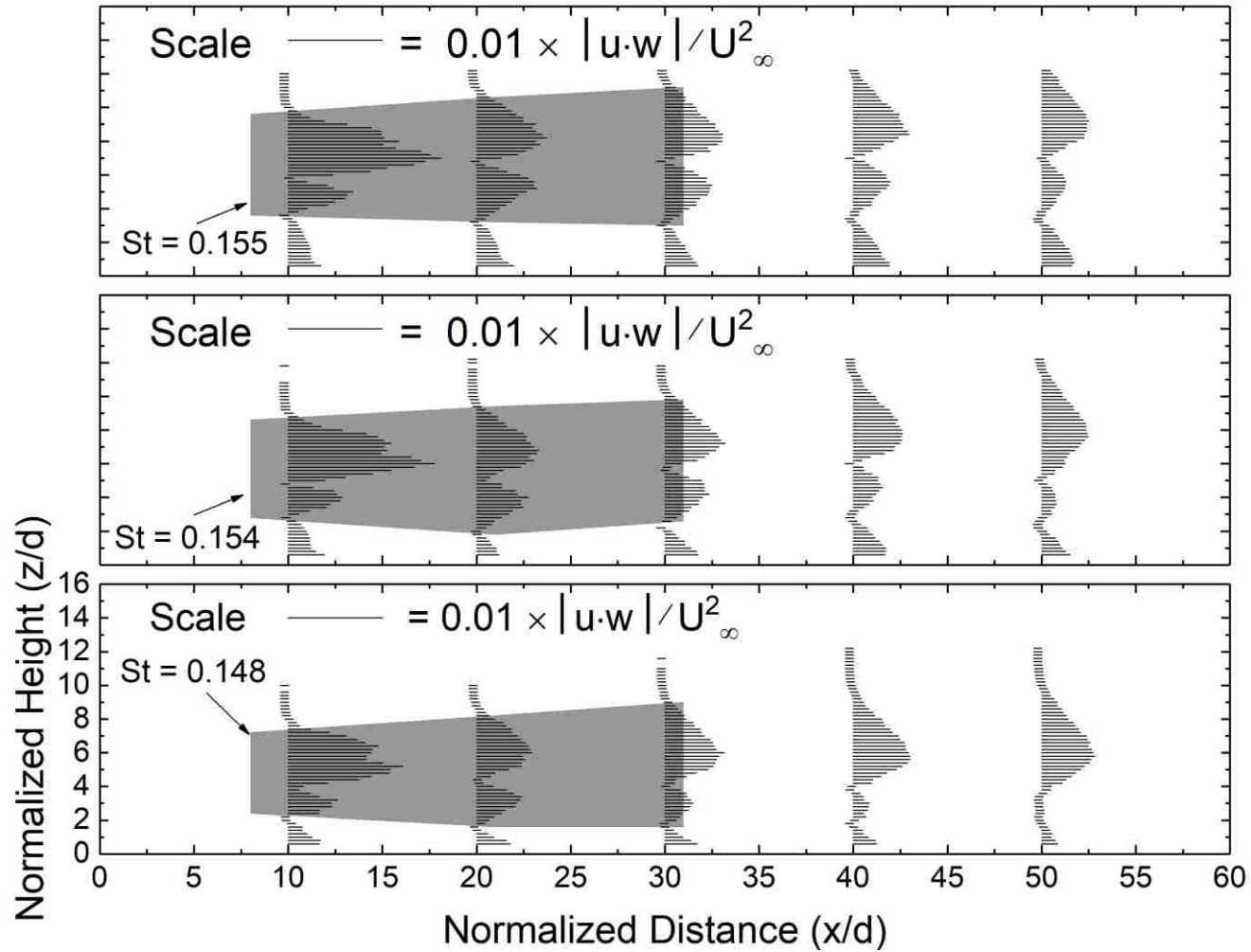
Figure 3.16 Absolute normalized Reynolds shear stress plots. Top graph represents G/d = 5.3, middle represents G/d = 4.3 and bottom represents G/d = 3.3. Shaded portions indicate vortex shedding.
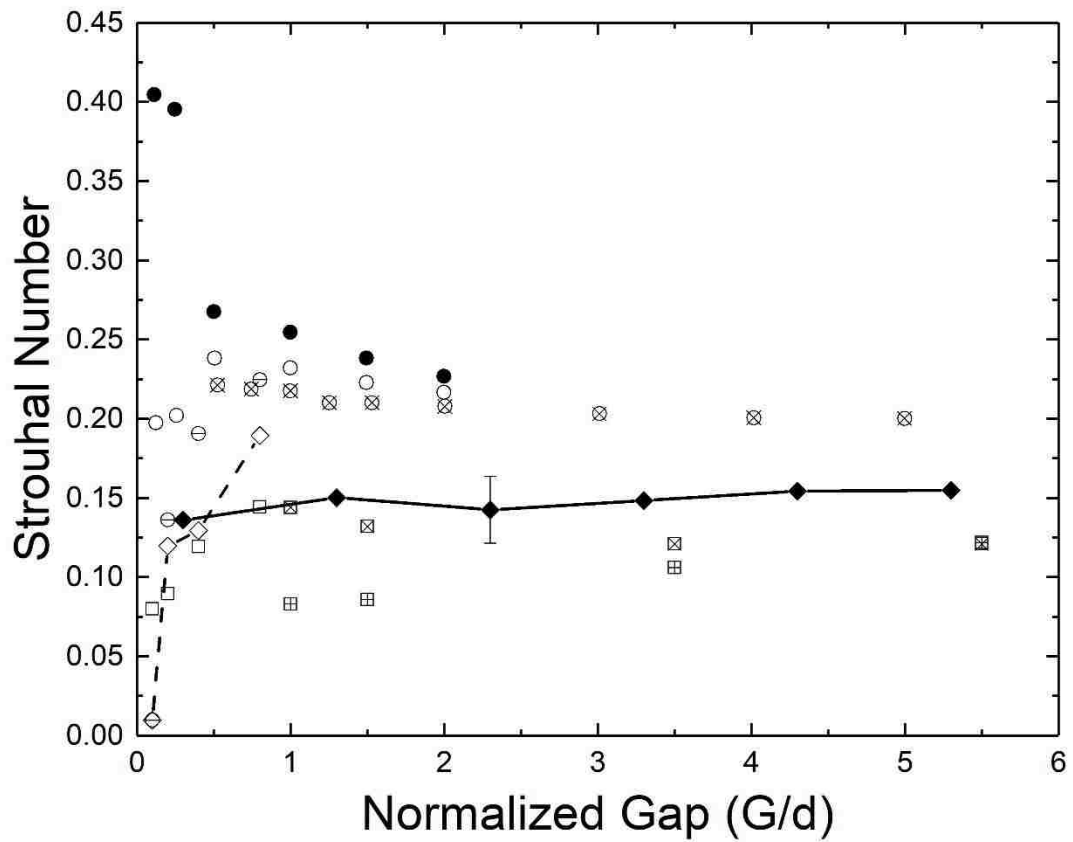
Figure 3.17 Summary of Strouhal data: ●, Price et al. [21], $Re_d = 1.2 \times 10^3$, $\delta = 0.45d$; ○, Price et al. [21], $Re_d = 4.9 \times 10^3$, $\delta = 0.45d$; ⊗, Angrilli et al. [27], $Re_d = 3.8 \times 10^3$, $\delta = 0.4d$; ⊖, Bayraktar et al. [23], circular tripwire, $Re_d = 2.0 \times 10^4$; ⊠, Hwang et al. [25], square tripwire, $Re_d = 10^3$, $\delta = 0.8d$; ⊞, Hwang et al. [25], square tripwire, $Re_d = 10^3$, $\delta = 5.0d$; □, Bayraktar et al. [23], square tripwire, $Re_d = 2.0 \times 10^4$; ◇, Bayraktar et al. [23], diamond tripwire, $Re_d = 2.0 \times 10^4$; ◆, present study.

71

◼ Conclusion

Heat transfer from a flat plate near a diamond-shaped tripwire was analyzed using a thermal camera. The results showed that, at $G/d = 0.3$, the near-wake region experienced little improvement as a separation bubble originating from the top shoulder of the tripwire was attached to the wall. The far-wake, on the other hand, was extremely conducive to cooling a flat surface due to higher turbulence and shear stresses. As the gap ratio was increased to 1.3, vortical activity and higher streamwise velocity near the plate surface substantially improved heat transfer in the near-wake. In the far-wake the Nusselt number decreases and a vortex shedding frequency is not observed. Increasing the gap ratio to 2.3 also increased the distance where a dominant frequency in the spectral density plots were observed. An improved Nusselt number was observed from $x/d = 5$ to 40. At $G/d > 2.3$, the Nu/Nu_o was near 1. The tripwire-generated wake was positioned farther away from the wall and did not disturb the flow near the wall. In addition, the vortices had no influence on heat transfer when G/d increased from 2.3.

References

[1]   E. Marumo, K. Suzuki, T. Sato, Turbulent heat transfer in a flat plate boundary layer disturbed by a cylinder, Int. J. Heat Fluid Flow. 6 (1985) 241–248. doi:10.1016/0142-727X(85)90056-6.

[2]   T.-M. Liou, Y. Chang, D.-W. Hwang, Experimental and computational study of turbulent flows in a channel with two pairs of turbulence promoters in tandem, J. Fluids Eng. 112 (1990) 302. doi:10.1115/1.2909405.

[3]   L. Wang, B. Sundén, Experimental investigation of local heat transfer in a square duct with continuous and truncated ribs, Exp. Heat Transf. 18 (2005) 179–197. doi:10.1080/08916150590953397.

[4]   M. Shafiqul Islam, M. Kaminaga, R. Hino, M. Monde, Prediction of turbulent flow structure in a fully developed rib-roughened narrow rectangular channel, J. Therm. Sci. 18 (2009) 126–136. doi:10.1007/s11630-009-0126-1.

[5]   S.U. Onbasioglu, H. Onbaşıoğlu, On enhancement of heat transfer with ribs, Appl. Therm. Eng. 24 (2004) 43–57. doi:10.1016/S1359-4311(03)00216-3.

[6]   A. Yadav, J. Bhagoria, A numerical investigation of square sectioned transverse rib roughened solar air heater, Int. J. Therm. Sci. 79 (2014) 111–131. doi:10.1016/j.ijthermalsci.2014.01.008.

[7]   S. Eiamsa-ard, W. Changcharoen, Analysis of turbulent heat transfer and fluid flow in channels with various ribbed internal surfaces, J. Therm. Sci. 20 (2011) 260–267. doi:10.1007/s11630-011-0468-3.

[8]   S. Alfarawi, S.A. Abdel-Moneim, A. Bodalal, Experimental investigations of heat transfer enhancement from rectangular duct roughened by hybrid ribs, Int. J. Therm. Sci. 118 (2017) 123–138. doi:10.1016/j.ijthermalsci.2017.04.017.

[9]   A. Tariq, P.K. Panigrahi, K. Muralidhar, Flow and heat transfer in the wake of a surface-mounted rib with a slit, Exp. Fluids. 37 (2004) 701–719. doi:10.1007/s00348-004-0861-8.

[10]   K. Ryu, S. Yook, K. Lee, Forced convection across a locally heated square cylinder near a wall, Numer. Heat Transf. Part A Appl. 65 (2014) 972–986. doi:10.1080/10407782.2013.850930.

[11]   G.J. Poitras, L.-E. Brizzi, Y. Gagnon, Structure of channel flows with surface mounted ribs, J. Therm. Sci. 13 (2004) 213–219. doi:10.1007/s11630-004-0034-3.

[12]   R. Kamali, A.R. Binesh, The importance of rib shape effects on the local heat transfer and flow friction characteristics of square ducts with ribbed internal surfaces, Int. Commun. Heat Mass Transf. 35 (2008) 1032–1040. doi:10.1016/j.icheatmasstransfer.2008.04.012.

[13]   P. Promvonge, C. Thianpong, Thermal performance assessment of turbulent channel flows over different shaped ribs, Int. Commun. Heat Mass Transf. 35 (2008) 1327–1334. doi:10.1016/J.ICHEATMASSTRANSFER.2008.07.016.

[14]   D.K. Maiti, Numerical Study on Aerodynamic Characteristics of Rectangular Cylinders Near a Wall, Ocean Eng. 54 (2012) 251–260. doi:10.1016/j.oceaneng.2012.07.012.

[15]   J. Liu, S. Hussain, J. Wang, L. Wang, G. Xie, B. Sundén, Heat transfer enhancement and turbulent flow in a high aspect ratio channel (4:1) with ribs of various truncation types and arrangements, Int. J. Therm. Sci. 123 (2018) 99–116. doi:10.1016/j.ijthermalsci.2017.09.013.

[16]   W. Peng, P.-X. Jiang, Y.-P. Wang, B.-Y. Wei, Experimental and numerical investigation of convection heat transfer in channels with different types of ribs, Appl. Therm. Eng. 31 (2011) 2702–2708. doi:10.1016/j.applthermaleng.2011.04.040.

[17]   D. Chatterjee, G. Biswas, The Effects of Reynolds and Prandtl Numbers on Flow and Heat Transfer Across Tandem Square Cylinders in the Steady Flow Regime, Numer. Heat Transf. Part A Appl. 59 (2011) 421–437. doi:10.1080/10407782.2011.552374.

[18]   V. SriHarsha, S.V. Prabhu, R.P. Vedula, Influence of rib height on the local heat transfer distribution and pressure drop in a square channel with 90° continuous and 60° V-broken ribs, Appl. Therm. Eng. 29 (2009) 2444–2459. doi:10.1016/j.applthermaleng.2008.12.015.

[19]   G. Xu, Y. Li, H. Deng, Effect of rib spacing on heat transfer and friction in a rotating two-pass square channel with asymmetrical 90-deg rib turbulators, Appl. Therm. Eng. 80 (2015) 386–395. doi:10.1016/j.applthermaleng.2015.02.011.

[20]   M.S. Akoz, Flow structures downstream of the horizontal cylinder laid on a plane surface, Proc. Inst. Mech. Eng. Part C J. Mech. Eng. Sci. 223 (2009) 397–413. doi:10.1243/09544062JMES1111.

[21]   S. Price, D. Sumner, J. Smith, K. Leong, M. Païdoussis, Flow visualization around a circular cylinder near to a plane wall, J. Fluids Struct. 16 (2002) 175–191. doi:10.1006/jfls.2001.0413.

[22]   B.V. Ravi, P. Singh, S. V. Ekkad, Numerical investigation of turbulent flow and heat transfer in two-pass ribbed channels, Int. J. Therm. Sci. 112 (2017) 31–43. doi:10.1016/J.IJTHERMALSCI.2016.09.034.

[23]   S. Bayraktar, S. Yayla, A. Oztekin, H. Ma, Wall proximity effects on flow over cylinders with different cross sections, Can. J. Phys. 92 (2014) 1141–1148. doi:10.1139/cjp-2013-0692.

[24]   G.-S. He, J.-J. Wang, C. Pan, L.-H. Feng, Q. Gao, A. Rinoshika, Vortex dynamics for flow over a circular cylinder in proximity to a wall, J. Fluid Mech. 812 (2017) 698–720. doi:10.1017/jfm.2016.812.

[25]   R.R. Hwang, C.-C. Yao, A Numerical Study of Vortex Shedding From a Square Cylinder With Ground Effect, J. Fluids Eng. 119 (1997) 512. doi:10.1115/1.2819274.

[26]   G.J. Sheard, M.J. Fitzgerald, K. Ryan, Cylinders with square cross-section: wake instabilities with incidence angle variation, J. Fluid Mech. 630 (2009) 43. doi:10.1017/S0022112009006879.

[27]   F. Angrilli, S. Bergamaschi, V. Cossalter, Investigation of Wall Induced Modifications to Vortex Shedding From a Circular Cylinder, J. Fluids Eng. 104 (1982) 518. doi:10.1115/1.3241896.

CHAPTER 4

CONCLUSIONS

4.1   Summary and Conclusions

Solar power is one of the most promising renewable energy technologies. Operating temperature is one factor adversely affecting the efficiency of PV panels. One method of cooling PV panels is to increase convective heat transfer by disturbing the existing flow and increasing the rate of heat transfer with a tripwire. Thus, the aim of this study was to increase the rate of heat transfer from a PV panel by disturbing the existing flow configuration using a tripwire.

The effect of three tripwire geometries placed on a flat plate was evaluated at two Reynolds numbers in Chapter 2. The general flow structure behind a tripwire involved separation of the flow from the tripwire and a recirculation region immediately behind the tripwire, followed by reattachment of the flow and then redevelopment of the boundary layer. The normalized Nusselt number (Nu/Nu_o) in the recirculation region is lower than 1 due to the lower velocity in the recirculation region. As the flow reattached to the plate, small-scale vortices were generated, leading to a higher heat transfer rate in this region. The wall-normal velocity and turbulence generated after reattachment improves Nu/Nu_o in the far-wake. It was found that the square and diamond-shaped tripwires improved the heat transfer rate more than the circular tripwire. This is because the boundary layer behind the circular tripwire transitions into a turbulent boundary layer closer to the tripwire than the other two geometries. The distance of this boundary layer transition was further shortened at the increased Reynolds number.

In Chapter 3, the effect of introducing a gap between the bottom of a diamond-shaped tripwire and the flat plate was evaluated. Six normalized gap heights (G/d = 0.3, 1.3, 2.3,

3.3, 4.3 and 5.3) were tested at a single Reynolds number ($Re_d = 1.6 \times 10^3$). The interaction between the shear layer from the flat plate and the two shear layers from the top and bottom shoulder of the tripwire dictated the flow structure at each normalized gap. At G/d = 0.3, the flow structure was similar to that described in Chapter 2. However, the near-wake heat transfer rate was increased due to the flow coming from the gap between the tripwire and flat plate. The tripwire generated more intense turbulence near the plate and wall-normal velocity towards the plate in the far-wake. As the normalized gap was increased, von Kármán vortex shedding started. These vortices interacted with the flat plate to increase Nu/Nu_o, and they decayed after x/d = 30. When the tripwire is placed at G/d > 2.3, the vortices and turbulence; and the wake in general; were produced farther away from the flat plate. The flow structure near the plate was not disturbed by the wake, and thus the heat transfer rate was not augmented.

The overall normalized Nusselt number from the results of the two experiments discussed in Chapter 2 and 3 are published in the Table 4.1 below. It can be seen that the best heat transfer rate was observed behind the diamond shaped tripwire when there was no gap between the tripwire and the flat plate.

In order to calculate the effect of the enhanced heat transfer rate, the data and procedure used by Wu [1] was followed. Since, the best overall heat transfer results were observed behind the diamond shaped tripwire placed on the PV panel. The result of this configuration was used to calculate the operating temperature and the efficiency of the PV panel. It is assumed that the tripwire produces the averaged heat transfer rate over the complete span of the PV panel. Figure 4.1 below shows the efficiency of a PV panel calculated without and with a turbulator. The calculated improvement in the efficiency was found be in the range of 0.17 % to 0.57 %.

Table 4.1 Averaged normalized Nusselt number from experiments discussed in Chapter 2 and 3.

	Geometry	G/d	Nu/Nu$_0$		Geometry	G/d	Nu/Nu$_0$
Chapter 2	Circle	0	1.15	Chapter 3	Diamond	0.3	1.25
			1.05			1.3	1.07
	Square		1.26			2.3	1.02
			1.21			3.3	1.02
	Diamond		1.29			4.3	1.02
			1.41			5.3	1.01
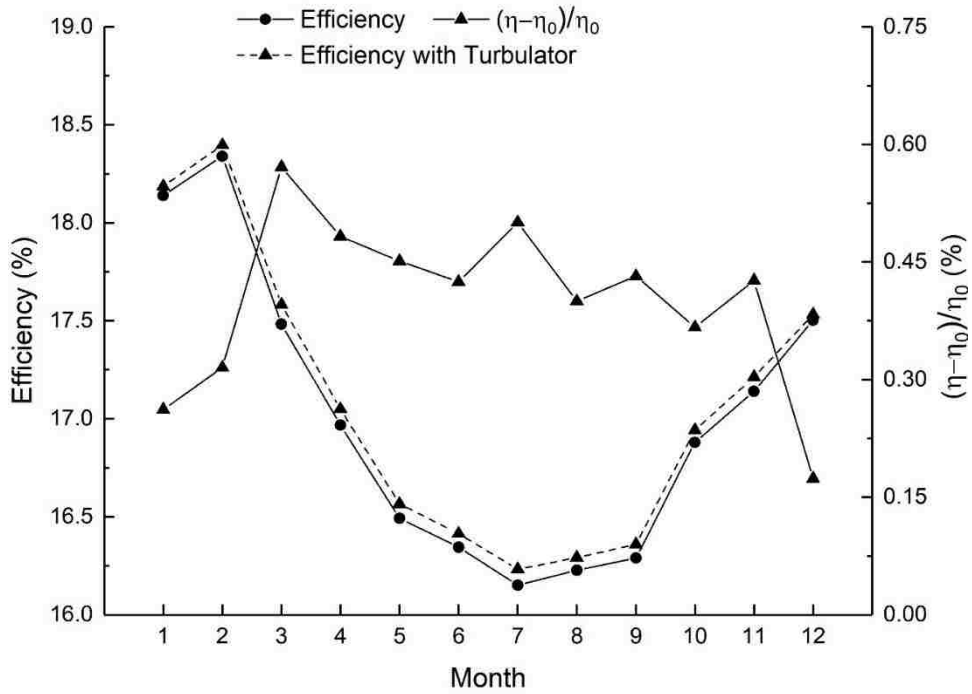
Figure 4.1 Calculated efficiency without and with a turbulator and the percentage improvement.

78

4.2 Future Work Recommendations

Based on the current study, it is clear that tripwires can positively augment heat transfer from a flat plate. Thus, they can be applied to cool PV panels. A diamond-shaped tripwire on a flat plate produced the best heat transfer rate compared to square and circular tripwires. Introducing a gap between the tripwire and the flat plate did not increase the overall heat transfer rate. However, few questions still remain that need to be addressed.

First, the square shaped tripwire was rotated 45° to make the diamond shape. This orientation generated the best heat transfer rate. However, other orientations may reduce the near-wake separation and thus increase the heat transfer rate.

Second, in the current study, an X-probe hotwire was utilized to identify the flow parameters. However, as mentioned in Chapter 2 and 3, the X-probe hotwire is not sensitive to the direction of flow. Thus, recirculation and reattachment could not be studied in depth. It is recommended that these topics should be analyzed using a directionally sensitive split-fibre probe to better understand the flow mechanism.

Third, gap heights from 0 to 1.3 should be evaluated at smaller increments. It is clear that the heat transfer rate changes drastically. The optimum gap height for the best heat transfer augmentation seems to be in this normalized gap range.

Increasing the level of turbulence in the oncoming flow changes the location of flow separation from a tripwire and also the vortex shedding frequency. The current work did

not investigate the effect of the oncoming flow parameters, but it should be studied in future work.

References

[1] Wu, Hao, "Engineering Flow Turbulence for Transport Enhancement" (2017). Electronic Theses and Dissertations. 7306. https://scholar.uwindsor.ca/etd/7306

APPENDICES

Appendix A. Promoting Vortical Flow Over a Flat Plate Using a Cylindrical Rod on the Leading Edge

Ashhar Ahmed[1], David S-K. Ting[1†] & Steve Ray[2]

1. Turbulence and Energy Laboratory, Centre for Engineering Innovation, University of Windsor, 401 Sunset Ave, Windsor, Ontario, N9B 3P4, Canada

2. Essex Energy Corporation, 2199 Blackacre Dr, Suite #2, Oldcastle, Ontario, N0R 1L0, Canada

† corresponding author, dting@uwindsor.ca

A.1 Introduction

The flow over a cylinder placed on or near a flat surface has been the subject of numerous studies [2–29] due to its real-world applications such as a submerged pipeline, electrical poles, and supporting structures of bridges. The interaction of a bluff body wake in a boundary layer also sheds light on complex aerodynamics components such as multi-element airfoils and turbo machinery. Existing studies have focused on the near wake flow interaction between the obstruction and flow, and its effect on the classical von Karman streets. Little attention has been given to the vortical activities farther downstream, which is critical when sustained near-surface turbulence is desirable. Selected observations from highlighted studies are summarized in Table A.1. The flow over a cylinder near a flat surface is comprised of interaction between three shear layers, two from the cylinder shoulders and the boundary layer over the flat surface. The shear layer from the cylinder shoulder near the flat surface has counter-vorticity with respect to the boundary layer [24]. When there is no gap between the cylinder and the surface, the boundary layer rolls up and forms a separation bubble in front of the cylinder [3,5–7]. The shear layer from the upper shoulder of the cylinder twirls up and then attaches itself to the flat surface. Since there is

81

no gap between the flat surface and the cylinder, the third shear layer does not form. Some recent studies have also found the presence of a secondary separation bubble just downstream of the cylinder [16,24].

When there is a gap between the cylinder and the plate, the flow behind the cylinder can be characterized into three regimes. For $0 < G/d \le 0.25$ (where G is the gap between the bottom of the cylinder and the flat surface, and "d" is the diameter of cylinder), the flat plate boundary layer and the shear layer from the bottom of the cylinder interact, forming a weak gap flow [14]. Due to the opposing vorticity of these shear layers, the gap flow is transient, and a separation bubble is sporadically formed upstream [19]. As the gap widens, the coupling between these shear layers weakens. The shear layer from the bottom surface of the cylinder whirls into vortices. These vortices are skewed towards the flat surface. The fluctuations in the lift coefficient of the cylinder are irregular with a severely reduced amplitude [30]. The vortices shed behind the cylinder are a function of the Reynolds number. This flow regime is frequently compared to the flow behind a backward facing step [14,17,31]. The gap flow becomes stronger for $0.25 < G/d \le 1.5$, which reduces the size of the separation bubble on the wall. The separation bubble behind the cylinder is skewed toward the wall due to the boundary layer. The amplitude of the fluctuating lift coefficient is reduced as compared to an isolated cylinder, but the fluctuations are regular [30]. Vortices are shed from all three shear layers at a similar Strouhal number. For G/d larger than 1.5, the Strouhal number resembles that of an isolated cylinder and does not depend on the gap ratio.

Table A.1 Chronological highlights of cylinder near wall studies. BL = Boundary layer, d = diameter of cylinder, e = exponent of 10, i.e 10^e, FV = flow visualization experiment, FM = force measurements, G = cylinder – wall gap, H = shape factor of BL, HW = hot wire and/or hot film analysis, PIV = particle image velocimetry, PM = pressure measurements, TM = temperature measurements, x = downstream distance from the cylinder, X_l = cylinder placement from the leading edge, δ = boundary layer thickness .

Reference	Experiment Details	Measurement	Main Findings
Bearman & Zdravkovich [3]	X_l = 32d, Re_d = 2.5e4 ~ 4.8e4, G/d = 0 ~ 3.5, x/d = 0.4 ~ 8	PM, HW, FV	Separation bubble forms both upstream and downstream of cylinder. It is attached to cylinder at G/d = 0.
Zdravkovich et al [6]	X_l = 0.77d and 1.43d, Re_d = 4.4e4, 7.2e4 ~ 1.4e5	FM	The drag coefficient is unaffected by G/d ratio until δ/d becomes comparable to G/d. Lift coefficient is highly affected by G/d.
Marumo et al [7]	X_l = 175d, Re_d = 7.7e3, G/d = 0 ~ 3.69, x/d = 117.5	HW, TM, PM, FV	Heat transfer deteriorates just downstream of cylinder for G/d = 0, due to separation bubble and flow reversal. The eye of separation bubble occurs at x/d = 0.375 downstream. FV results shows that the flow reattaches before x/d = 12.5.
Lei at al [11]	X_l = 11d, Re_d = 1.3e4 ~ 1.45e4, G/d= 0 ~ 3	PM	Cylinder pressure distribution = f(δ/d, G/d) As G/d increases — Stagnation point moves away from plate; Wake shrinks As δ/d increases — Stagnation point moves away from plate; $(G/d)_{cr}$ decreases
Price et al [14]	X_l = 10d, Re_d = 1.2e3 ~ 4.9e3, G/d = 0 ~ 2, x/d = 4.8	FV, HW, PIV	No gap flow, a strong shear layer moving away from the wall without rolling up into a vortex.
Akoz [16]	Re_d = 1.0e3 ~ 7.0e3, G/d= 0,	PIV	2 separation regions, primary at 9d ~ 10d downstream, secondary at 0.73d ~ 1.2d. Separation point moves downstream with increasing Re_d.

	x/d = 11		The separated flow from the second separation bubble moves towards the cylinder, and before reaching the cylinder, the flow curls up and causes a vortex formation in cylinder near-wake.
He et al. [18]	$X_l = 15d$, $Re_d = 1.1e3$, $G/d = 1.8$, $x/d = 2.5 \sim 45$	PIV	The u_{rms} peak inside the boundary layer increases rapidly after x/d = 12.5, implying the onset of the boundary layer transition. At x/d = 45, the mean velocity deficit and rms velocity contained within the wake become insignificant and the BL achieves a shape factor of H = 1.50.
He et al [19]	$X_l = 15d$, $Re_d = 1.1e3$, $G/d = 1$, $x/d = 2.5 \sim 45$	PIV	At moderate gap ratios, the cylinder wake induces secondary vortices inside the boundary layer. The wake/ BL interaction can be characterized as the interaction between the secondary vortex in the near-wall region and the lower roller sheds from the cylinder. The secondary vortex experiences a linear lift-up due to mutual induction from the lower roller.
He et al [24]	$X_l = 15d$, $Re_d = 1.1e3$, $G/d = 1$, $x/d = 0 \sim 14$	PIV	G/d = 0, flow resembles the flow behind a backward step. G/d = 0.25, jet-like gap flow G/d = 0.5, stronger gap flow which deflects away from the wall and maintains considerable momentum when it makes contact with the upper shear layer of the cylinder. G/d = 1, the separation bubble behind the cylinder remains asymmetric, but the separation bubble on the wall shrinks. The mean vorticity is symmetric in upper and lower shear layers, with asymmetric u_{rms} due to the interaction of flat plate boundary layer and lower shear layer. G/d = 1.5, the asymmetry is not evident, and a periodic separating bubble on the wall forms which is coupled with the formation of secondary vortices in the BL. At G/d=2, the local periodic separation is close to the wall in instantaneous flow field. G/d > 2, there is no BL separation, although the growth of BL thickness downstream of the cylinder is obvious.

As discussed above and shown in Table A.1, previous studies have focused on the interaction between the cylinder, wall and boundary layers and the mechanism of vortex formation. Very little attention has been paid on the near-wall flow farther downstream. The goal of this paper is to scrutinize the vortical structures and flow mechanics moderately far downstream a cylinder placed on the leading edge of a flat plate. The analysis includes a detailed study of vortex shedding frequencies at x/d = 6.25, 12.5, 18.75, 25 and 31.25 downstream, of a cylinder placed on the leading edge of a flat plate.

Nomenclature

BL = Boundary layer

d = Diameter of the cylinder

G = Distance between the bottom of the cylinder and the top of plate

H = Shape factor of boundary layer. H $\cong$ 1.4 for turbulent BL and H = 2.59 for laminar BL [1]

Re_d = Reynolds number based on the diameter of the cylinder

Re_x = Reynolds number based on the distance from the leading edge

St = Strouhal number

$\overline{U}$ = Time averaged velocity

U_∞ = Free stream velocity

u_{rms} = Friction or fluctuating velocity

X_l = Distance of cylinder from the leading edge of plate

x = Downstream distance from the leading edge of plate

z = Azimuthal distance from the plate surface

ε = Turbulent energy dissipation rate

η = Kolmogorov length scale

ν = Kinematic viscosity

A.2 Experimental Setup

The experiments were performed in a closed loop wind tunnel as shown in Figure A.1. The test section is 1.83 m long with a 0.762 m by 0.762 m cross section. The plate was 33.5 cm wide, 52.5 cm long, and 2.35 cm thick with a leading edge tapered at 21° to reduce flow separation. A 0.4 cm stainless steel rod was placed on the leading edge of the plate. The combined blockage ratio of the fixture and the model is around 4%.

A hot-wire anemometer was used to measure the instantaneous velocity at x/d = 6.25, 12.50, 18.75, 25.00 and 31.25 downstream of the leading edge. At each position, data was acquired at a height range from z/d = 0.75 to 8.75 at 0.25 intervals as shown in Figure 1. The free stream velocities were set at 2.5, 5.2, and 7.5 m/s. A Dantec hot wire X-probe (55P61) was utilised to acquire 10^6 samples of instantaneous velocity. The probe was connected using support (55H25) to two Dantec constant temperature anemometers (model 55C90) modules on a StreamLine Pro frame. Data was acquired using Streamware software and was sampled at 80 kHz and low-pass filtered at 30 kHz to avoid aliasing. In this study, the Reynolds number is calculated based on the diameter of the rod as well as the downstream distance (x) using Equation A - 1

$$Re_d = \frac{U_\infty \times d}{\nu} \qquad \text{(A - 1)}$$

where ν is the kinematic viscosity of air, and d is the diameter of cylinder. Another way to compare flow parameters at certain locations of flow field requires the Reynolds number calculated based on the downstream distance from the leading edge of the plate, x, instead

of the cylinder diameter, d, in Equation A - 1. The Reynolds numbers based on diameter and downstream distance for each test case are presented in Table A.2.
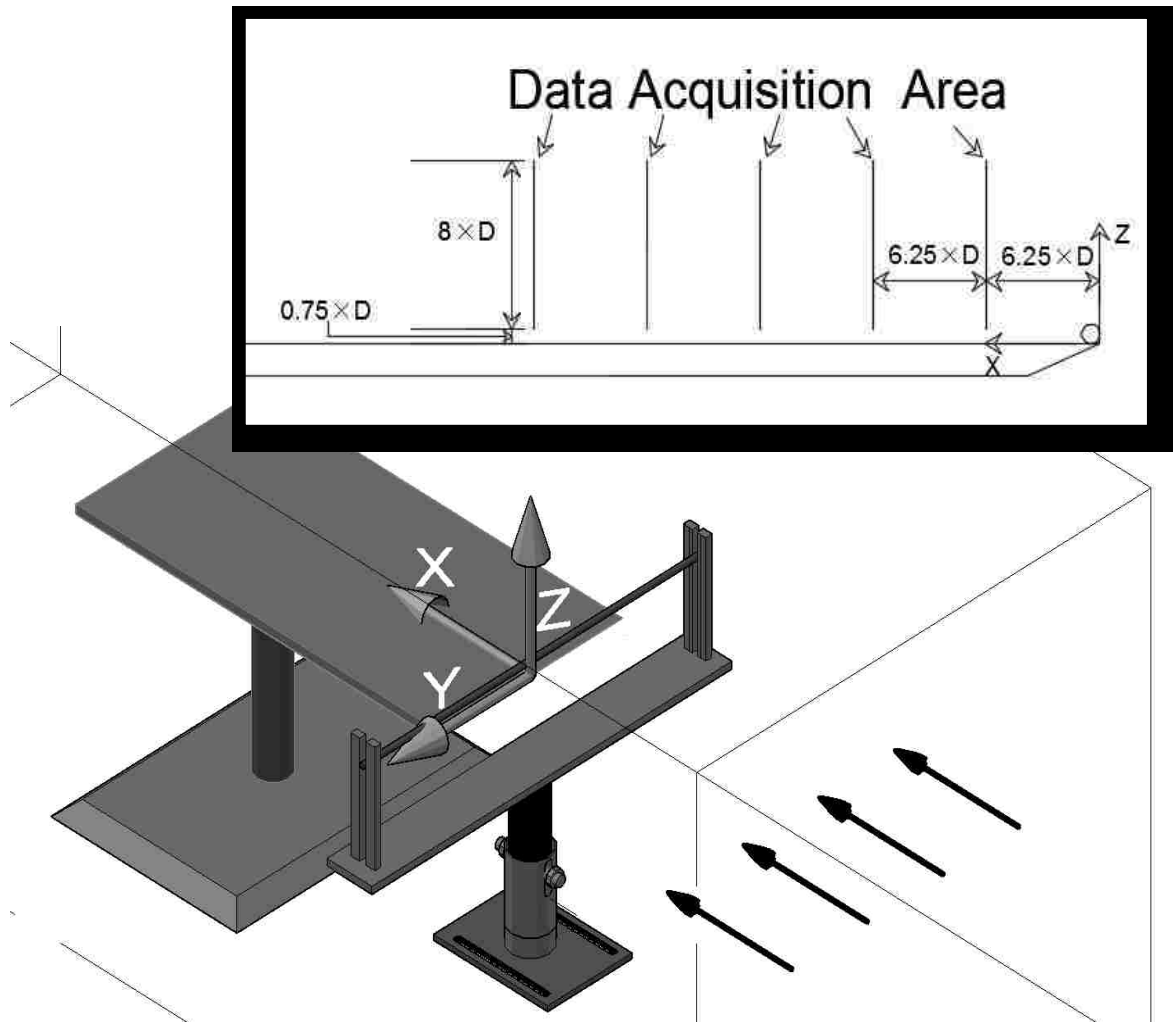

Figure A.1 Test setup, showing the placement of trip wire, and data acquisition points.

Table A.2 Test matrix presenting studied Reynolds number and downstream distances.

Re_d	x/d = 6.25	x/d = 12.5	x/d = 18.75	x/d = 25	x/d = 31.25
0.7×10^3	$Re_x = 4.4 \times 10^4$	8.7×10^4	1.3×10^5	1.8×10^5	2.2×10^5
1.4×10^3	$Re_x = 8.7 \times 10^4$	1.7×10^5	2.6×10^5	3.6×10^5	4.4×10^5
2.0×10^3	$Re_x = 1.3 \times 10^5$	2.5×10^5	3.7×10^5	5.0×10^5	6.2×10^5

A.3 Flow Parameters of Interest and Their Formulae

The frequencies associated with the vortical structures embedded in the velocity signal can be determined using spectral density analysis. The periodic vortices shed from the cylinder show up as a dominant peak in the spectral density plot. These vortices promote intermixing in the flow. The Spectrum Density Analysis was performed by processing the velocity signal from the hotwire using "pwelch" command in MatLAB. The signal was windowed at 2^{14} samples and the number of discrete Fourier transform points in the resultant frequency spectrum was fixed at 2^{15}. The dimensional vortex shedding frequency can be nondimensionalized into the Strouhal number,

$$St = \frac{f \times d}{\overline{U}}$$

(A - 2)

where $\overline{U}$ is the local time-averaged velocity

By the definition of a turbulent flow, the output signal is comprised of a mean and a fluctuating component of velocity. Local time-averaged velocity is the most fundamental parameter which can provide the velocity profile. The locations of shear in the flow can be easily determined from velocity profile plots. Mean velocity can be calculated from

$$\bar{U} = \frac{1}{N-1} \sum_{i=1}^{N} U_i \tag{A - 3}$$

Due to fluctuations in the velocity, mean calculated using the above formula does not adequately reflect the flow regime. The fluctuating or root mean square velocity calculated from Equation A - 4 reflects the variance of velocity from the mean.

$$u_{rms} = \sqrt{\sum_{i=1}^{N} \frac{(u_i)^2}{N-1}} \tag{A - 4}$$

The fluctuating velocity can be nondimensionalized using the free stream velocity (Equation A - 5). The turbulence intensity thus obtained can be further expressed in term of percentage.

$$Tu = \frac{u_{rms}}{U_\infty} \tag{A - 5}$$

The Reynolds Stresses matrix can be categorised into normal and tangential stresses,

$$Reynolds\ Stress = \begin{bmatrix} u \cdot u & u \cdot v & u \cdot w \\ v \cdot u & v \cdot v & v \cdot w \\ w \cdot u & w \cdot v & w \cdot w \end{bmatrix} \tag{A - 6}$$

Each of the component (u, v and w) are computed using Equation A - 7 combined with Equation A - 4.

$$u \cdot u = \frac{1}{N-1} \sum_{i=1}^{N} \overline{u_i \cdot u_i} \tag{A - 7}$$

The diagonal components, (u·u, v·v and w·w) are considered normal stresses and act parallel to the surfaces in X, Y and Z direction respectively. The remaining six components act perpendicular to surfaces, and represent the friction or shear.

Skewness factor and Kurtosis factor are two normalized parameters which provide valuable information about the probability distribution of a signal [26]. Skewness represents the symmetry of the velocity signal. A perfectly symmetric signal has a skewness factor of zero. On the other hand, if the magnitudes of fluctuations are clustered either higher or lower than mean velocity, a positive or negative skewness factor would result. Kurtosis factor reflects the distribution of fluctuations. A signal with high kurtosis tends to have fluctuations in the "tail" section of the distribution curve.

$$Skewness\ Factor = \frac{\overline{u^3}}{u_{rms}^{\ 3}} \qquad (A - 8)$$

$$Kurtosis\ Factor = \frac{\overline{u^4}}{u_{rms}^{\ 4}} \qquad (A - 9)$$

Energy dissipation rate ($\mathcal{E}$) is the parameter characterizing the amount of energy lost via viscosity into heat [32]. Based on the Taylor's frozen hypothesis [33], the dissipation rate can be deduced from

$$\mathcal{E} = \frac{15\nu}{\overline{U}^2} \overline{\frac{\partial u}{\partial t}}^2 \qquad (A - 10)$$

For discrete data points, the above equation can be rewritten as

$$\mathcal{E} = \frac{15\nu}{\overline{U}^2} \left[\frac{1}{N} \sum_{i=1}^{N-1} \left(\frac{U_{i+1} - U_i}{\Delta t} \right)^2 \right] \qquad (A - 11)$$

The turbulence energy dissipation rate can then be utilized to estimate the size of eddies responsible for the viscous dissipation of energy using

$$\eta = \left(\frac{\nu^3}{\varepsilon} \right)^{1/4} \qquad (A - 12)$$

A.4 Results and Discussion

A.4.1 Spectral Density Analysis

The vortex shedding frequency in terms of Strouhal number for the tested Reynolds numbers are shown in Figure A.2. No dominant frequency was observed in the height range of z/d = 0.75 to 2 at x/d = 6.25 for all the tested velocities. The obvious, dominant frequencies observed at first downstream position are related to the shear layer of the top shoulder of the cylinder. The magnitude of Strouhal number is a function of Re_d and maximizes at $Re_d = 2.0 \times 10^3$. Part of the increase in St is possibly due to the small U_{local} in the wake region at x/d = 6.25; noting that the U_∞ and not the local mean velocity has been used in the normalizing of the shedding frequency. For $Re_d = 0.7 \times 10^3$, the Strouhal number is much larger at x/d = 6.25 and 12.5 (St = 0.14 ~ 0.12 versus 0.07 ~ 0.05 at the other x/d distances). The implication of this observation is that the wake region for Re_d = 0.7×10^3 persists to $x/d \cong 12.50$. The vortical activity is observable in the range of z/d = 1.75 to 4.25 for x/d = 6.25. The trend for $Re_d = 0.7 \times 10^3$ at x/d = 12.50 is similar to that at x/d = 6.25, the only difference being the value (St = 0.14 versus 0.13). Afterwards, at x/d = 18.75, 25.00 and 31.25, the Strouhal number stays in the range of 0.04 ~ 0.06.

A detailed analysis of spectrum density graphs is presented in this section. The spectral density graphs for selected individual positions at the tested Reynolds numbers are given in Figure A.3 (due to space constraints, graphs corresponding to the other cases are not included). The frequency spectrums from x/d = 6.25 in the z/d = 0.75 ~ 3 confirm the "stationary" separation bubble as no dominant frequency is observed until $z/d > 2$ for Re_d = 0.7×10^3 and 2.0×10^3, and $z/d > 1.75$ for $Re_d = 1.4 \times 10^3$. This region of flow with no vortex shedding frequency is coupled with lower mean local velocity and high turbulence intensity.

A comparison between the frequency spectrums of U and W components at x/d = 6.25 and z/d = 2.75 is also shown Figure A.3 (a). Another observation is the presence of a higher

frequency, weaker peak in the spectral density plots from W-component of velocity from $Re_d = 0.7 \times 10^3$ and 2.0×10^3. For $Re_d = 1.4 \times 10^3$ and 2.0×10^3, the vortical structures are mainly concentrated below $St = 0.1$ at $x/d = 12.5$ to 31.25. This is considerably lower than the case for an isolated cylinder ($St = 0.21$). The Strouhal number tends to decrease, while the range of z/d with a vortex shedding frequency enlarges, as x/d increases. These weak vortices observed farther downstream will potentially augment the heat transfer characteristics positively via enhanced mixing.

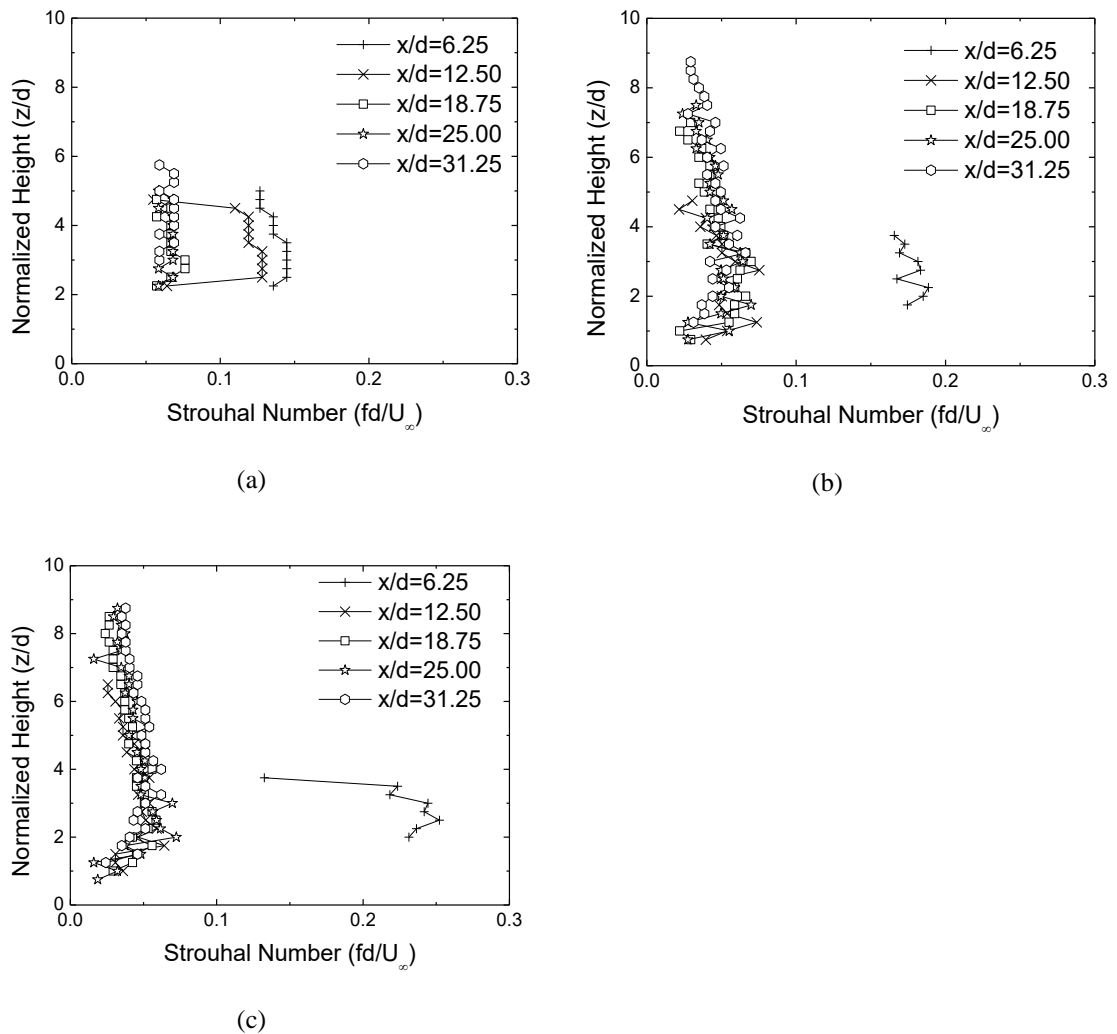(a)   (b)

(c)

Figure A.2 Strouhal number variation for (a) $Re_d = 0.7 \times 10^3$, (b) $Re_d = 1.4 \times 10^3$ and (c) $Re_d = 2.0 \times 10^3$

The spectrum density results from $Re_d = 1.4 \times 10^3$ show much greater fluctuation as compared to the results from $Re_d = 0.7 \times 10^3$; Figure A.3 (a) versus (b). At x/d = 6.25, the St is observed to fluctuate between 0.16 and 0.19 in the z/d = 1.75 ~ 3.75 range. The highest magnitude of Strouhal number is found at this Re_d at z/d = 2.25. There is no vortex shedding frequency detected after z/d = 4.25. At higher x/d distances the St is observed to be lower than 0.1 for all z/d values.

For the largest studied Re_d, the highest Strouhal number measured is 0.25 at x/d = 6.25 and z/d = 2.5. The Strouhal number stays around 0.22 ~ 0.25 until z/d = 3.5, after which St decreases rapidly to 0.13 at z/d = 3.75. Afterwards, no dominant frequency is observed at this x/d position. Similar to $Re_d = 1.4 \times 10^3$, the calculated St is below 0.1 at all z/d positions for x/d = 12.5 ~ 31.25.

It is worth mentioning that the general flow presumably transforms from a largely laminar into a relatively turbulent one as Re_d increases from 0.7×10^3 to $Re_d = 1.4 \times 10^3$, as can be inferred from the corresponding spectrum density plots. Along with the increasing fluctuations in the flow, the St number value increases. These trends intensified with a further increase in Re_d to 2.0×10^3. We shall invoke other results to provide a fuller picture of the underlying happenings.
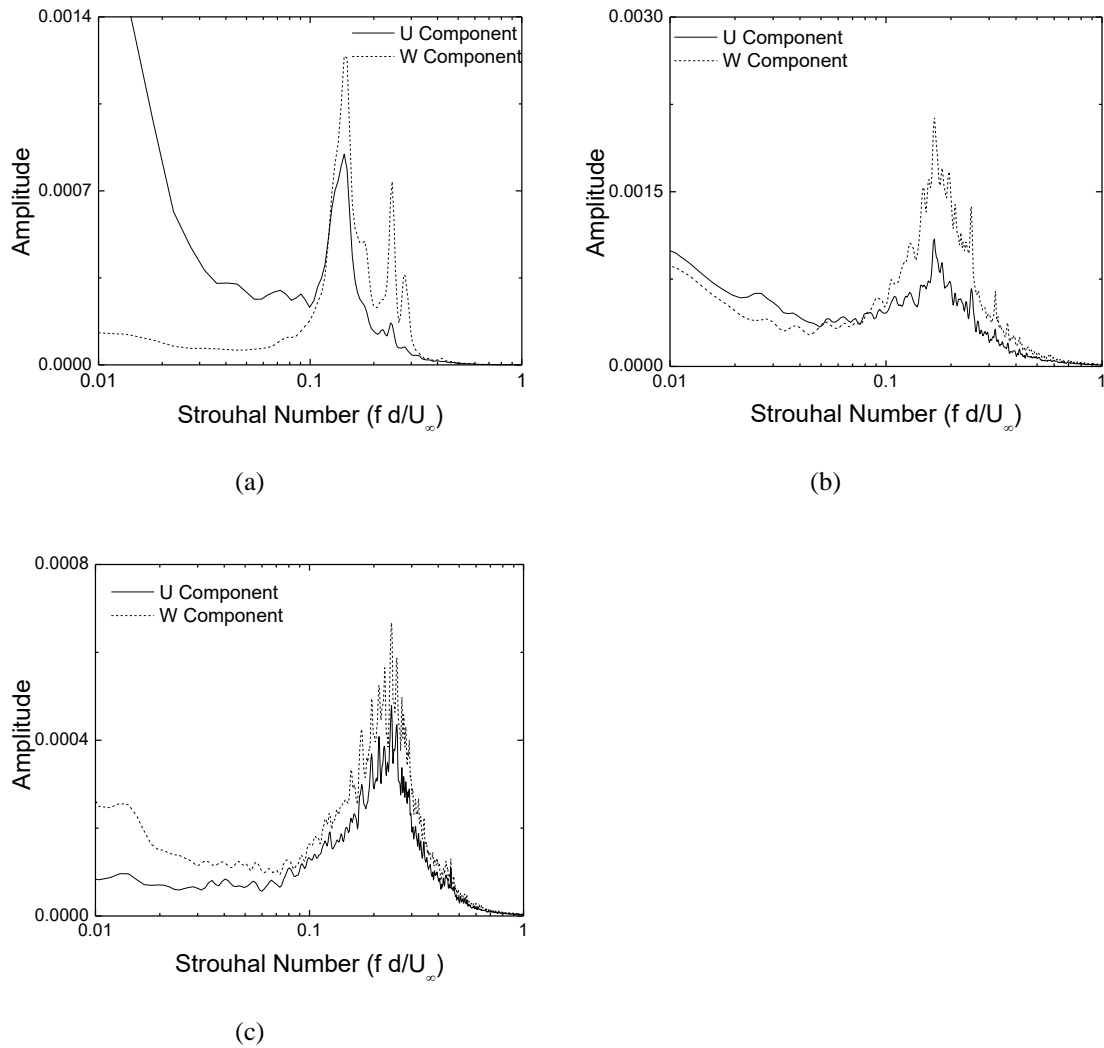
(a)

(b)

(c)

Figure A.3 Sample spectral density results from (a) $Re_d = 0.7 \times 10^3$, x/d = 06.25 and z/d = 2.75, (b) $Re_d = 1.4 \times 10^3$, x/d = 6.25 and z/d = 2.5 and (c) $Re_d = 2.0 \times 10^3$, x/d = 6.25 and z/d = 3.0

A.4.2 Time-Averaged Velocity Profiles

The time-averaged velocity represents the flow characteristics at a macro level. The effect of disturbances on the flow can be seen in the mean velocity graphs. The plots for U and W component are shown in Figure A.4 and Figure A.5, respectively. Starting off with $Re_d = 0.7 \times 10^3$, the first downstream position has a large velocity deficit area near the plate surface. The flow slows down substantially, although there appears to be no flow reversal in the streamwise direction at the studied locations. The results from Fourier transform confirm that there are no dominant vortex shedding frequencies in this area. The U-mean

velocity is seen to increase beyond the freestream value, with a peak of $U/U_\infty = 1.15$ at $z/d = 2.75$. The highest magnitude of St is also observed at this location. Afterwards, the U component slowly decreases to the free stream velocity. The flow adjusts accordingly to the blockage of the obtrusive cylinder and accelerates off the shoulder. The complementary W/W_∞ plots significantly further elucidate the flow retardation and recovery. A large gradient in W/W_∞ corresponds to the largest streamwise adjustment. Nevertheless, due to directional insensitivity, the directions of the smallest magnitude W/W_∞ vectors are uncertain. By approximately the second downstream location, the effect of the cylinder diminishes and the flow does not accelerate beyond the free stream velocity in the U direction.
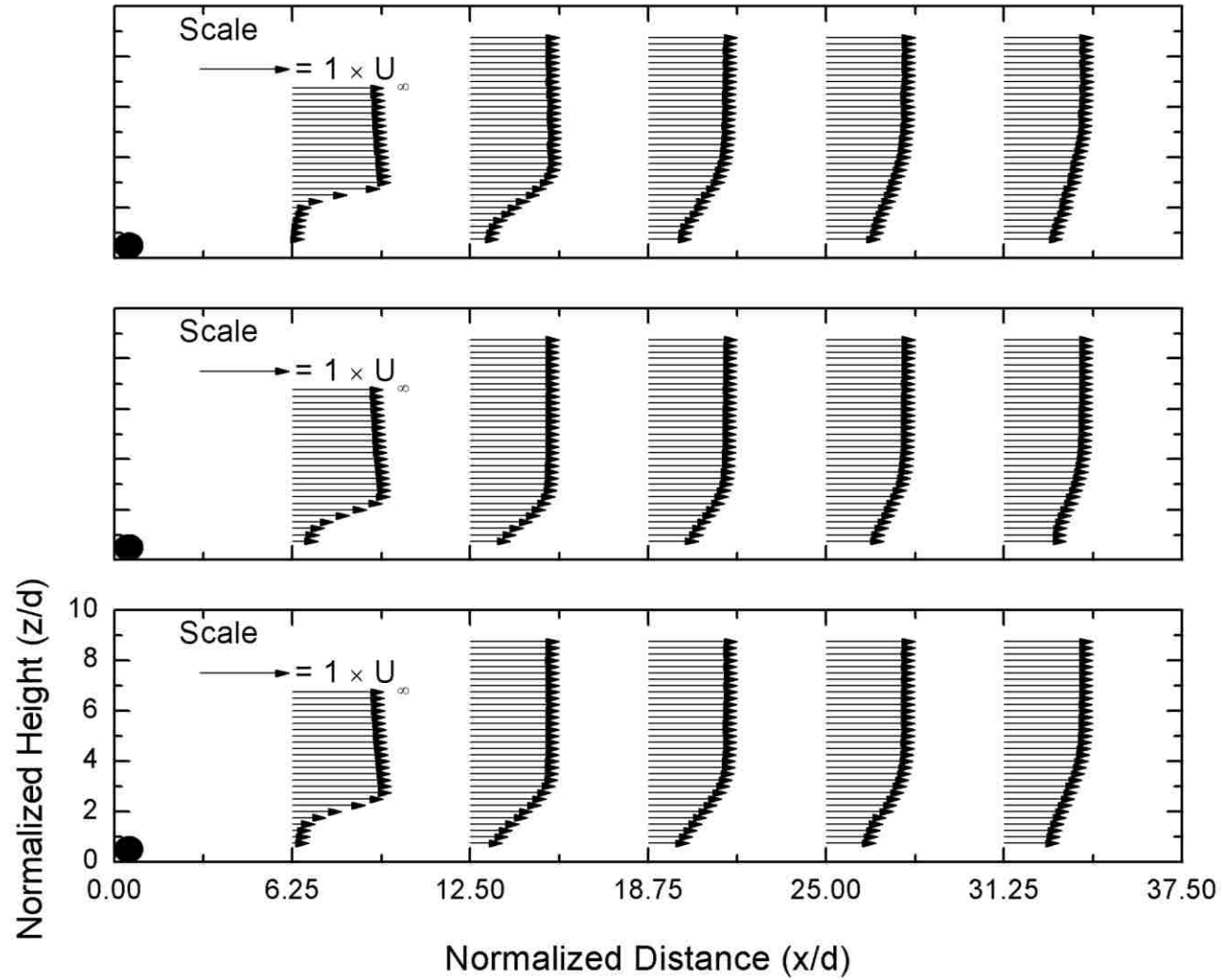
Figure A.4 Normalized U velocity profiles, top is $Re_d = 0.7 \times 10^3$, middle is $Re_d = 1.4 \times 10^3$ and bottom is $Re_d = 2.0 \times 10^3$. The values have been enhanced for clarity and ease of comparison.
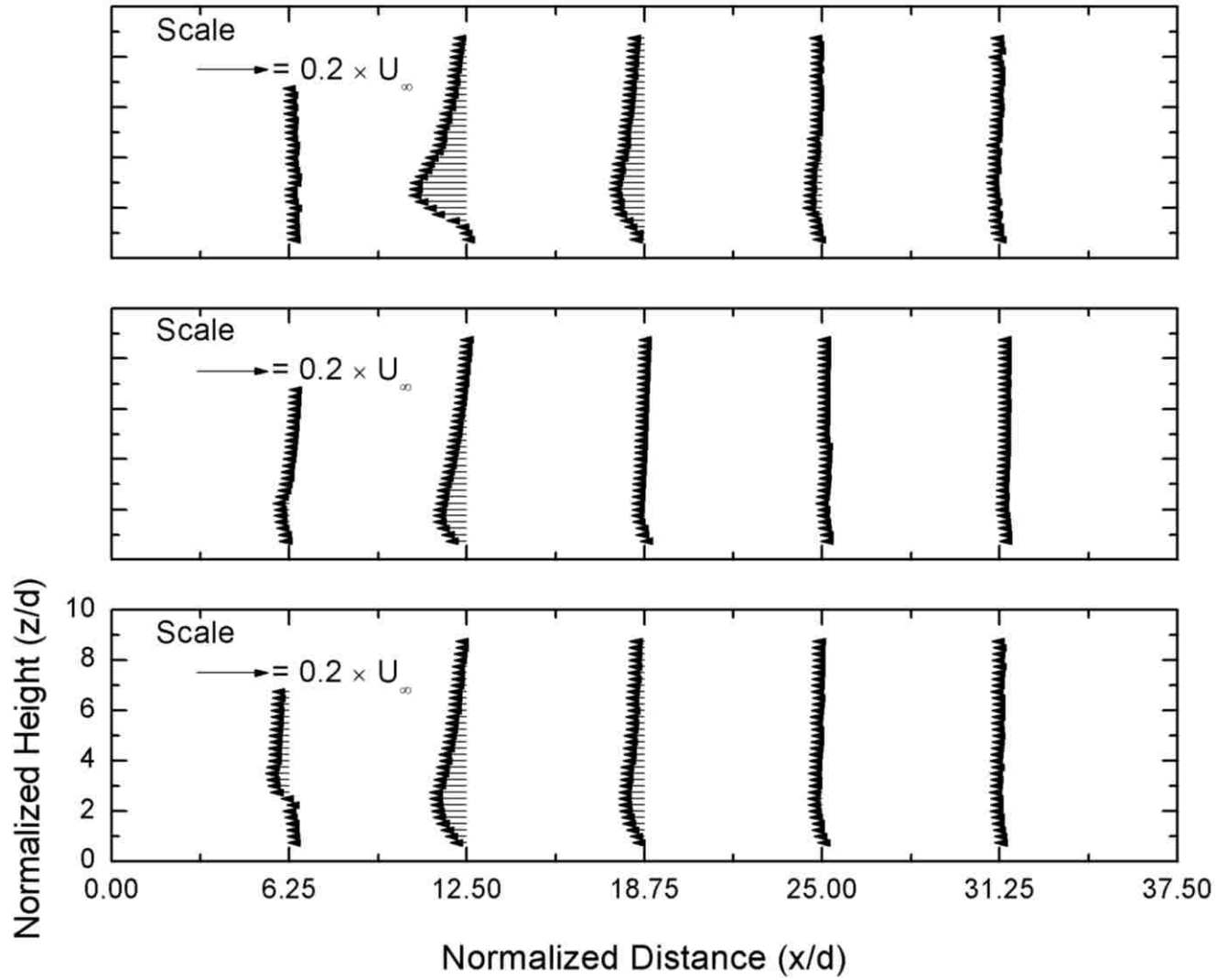
Figure A.5 Normalized W velocity profiles, top is $Re_d = 0.7 \times 10^3$, middle is $Re_d = 1.4 \times 10^3$ and bottom is $Re_d = 2.0 \times 10^3$. The values have been enhanced for clarity and ease of comparison.

A.4.3 RMS Velocity Profiles

Together with the mean velocity, the fluctuating velocity are the basic parameters for comprehending the flow characteristics. The blockage caused by the trip wire produces a shear in the flow field. Vortices are produced inside the shear layer as well as increased fluctuating velocity. Figure A.6 shows the trends for normalized u_{rms} velocity for the range of studied Reynolds numbers. The general trend for the u_{rms} plots can be concluded as follows.

At the first downstream location, $x/d = 6.25$, the peak turbulence intensity occurs at $z/d \approx$ 2, and it decreases sharply, resulting in a considerable gradient in the z direction. As expected, this maximum u_{rms} z location coincides with the maximum U gradient in Figure A.4. In other words, a large amount of turbulence is generated by flow shear in the streamwise direction. The reduction in flow shear with increasing Re_d (Figure A.4) leads to lower u_{rms} as portrayed in Figure A.6. As the wake prevails some distance downstream (Figure A.4), the amount of turbulence fluctuations increases, and more significantly, turbulence spreads across the wake. The decay of turbulence (Figure A.6) more or less corresponds to the fading of the wake (Figure A.4) farther downstream.

Turbulence intensities for W velocity are depicted in Figure A.7. The trends for w_{rms} generally corroborate with u_{rms}. Large w_{rms} occurs at large W shear in Figure A.5. It is worth noting that both W and w_{rms} are expected to be beneficial when it comes to enhancing heat and mass transfer.
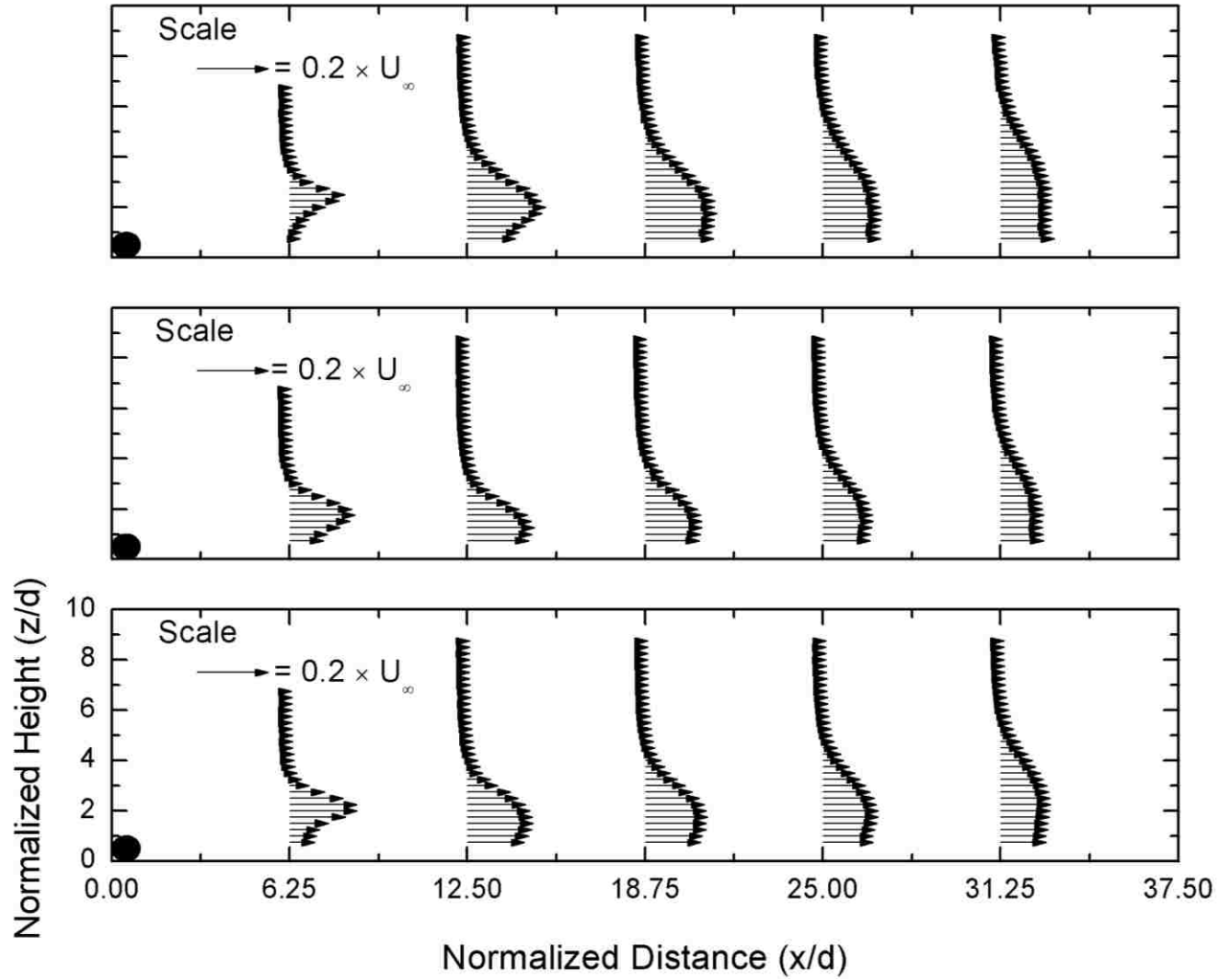
Figure A.6 Turbulence Intensity profile in stream-wise direction, top is $Re_d = 0.7 \times 10^3$, middle is $Re_d = 1.4 \times 10^3$ and bottom is $Re_d = 2.0 \times 10^3$
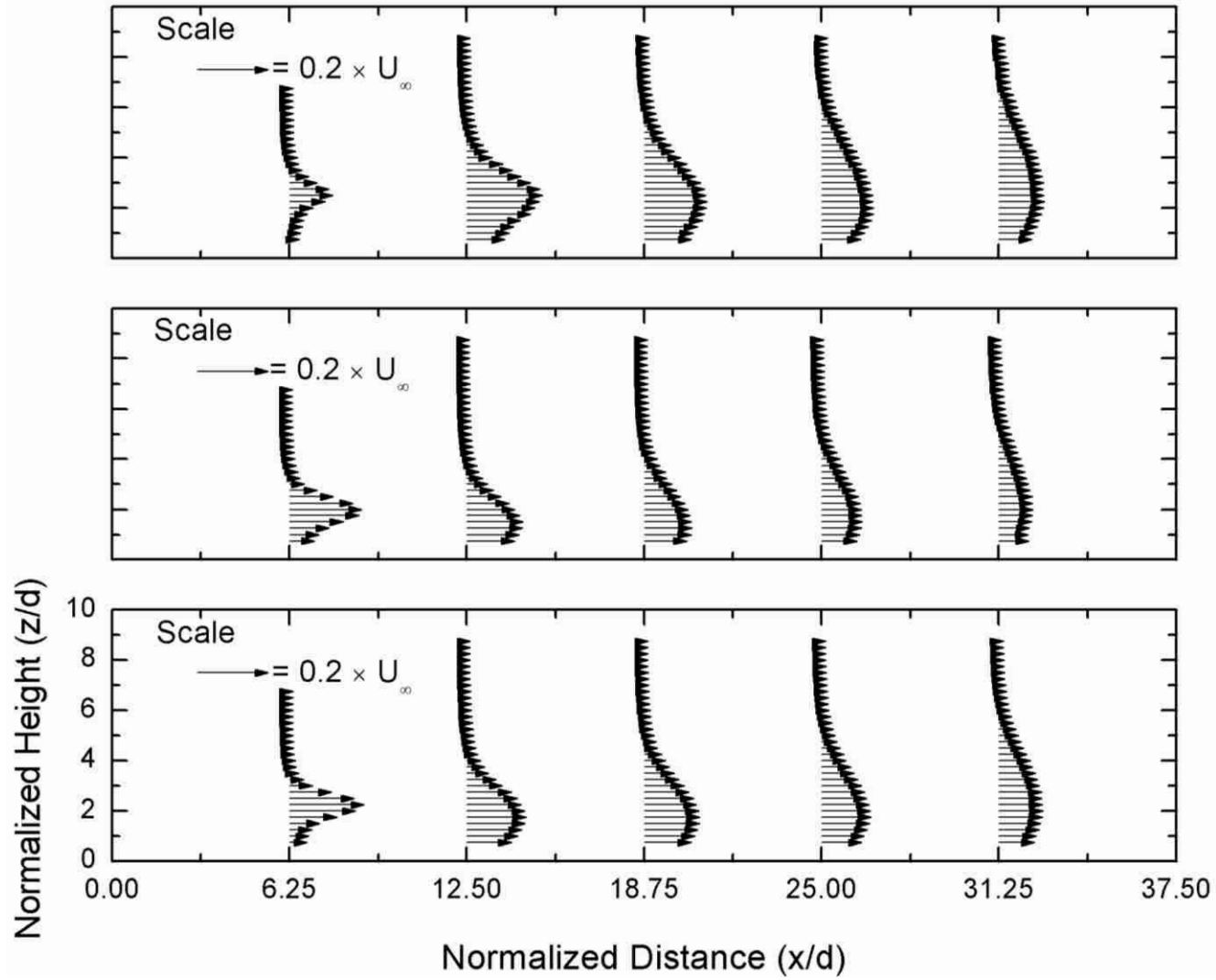
Figure A.7 Turbulence Intensity profile in cross-stream direction, top is $Re_d = 0.7 \times 10^3$, middle is $Re_d = 1.4 \times 10^3$ and bottom is $Re_d = 2.0 \times 10^3$

A.4.4 Tangential Reynolds Stresses

The tangential stresses indicate the straining and/or stretching in the X-Z direction and they transport mass between the otherwise parallel streamlines in the X direction. Just like the previously discussed parameters, the tangential stresses are observed to be localized around the upper edge of the cylinder. The z location of the peak stress approaches the plate before it moves away as the flow moves downstream. In the absence of significant turbulence generation, the tangential Reynolds stresses not only spread, but diminish farther downstream. The relatively long-lasting shear stresses near the plate are expected to augment the transfer of heat away from a heated plate.
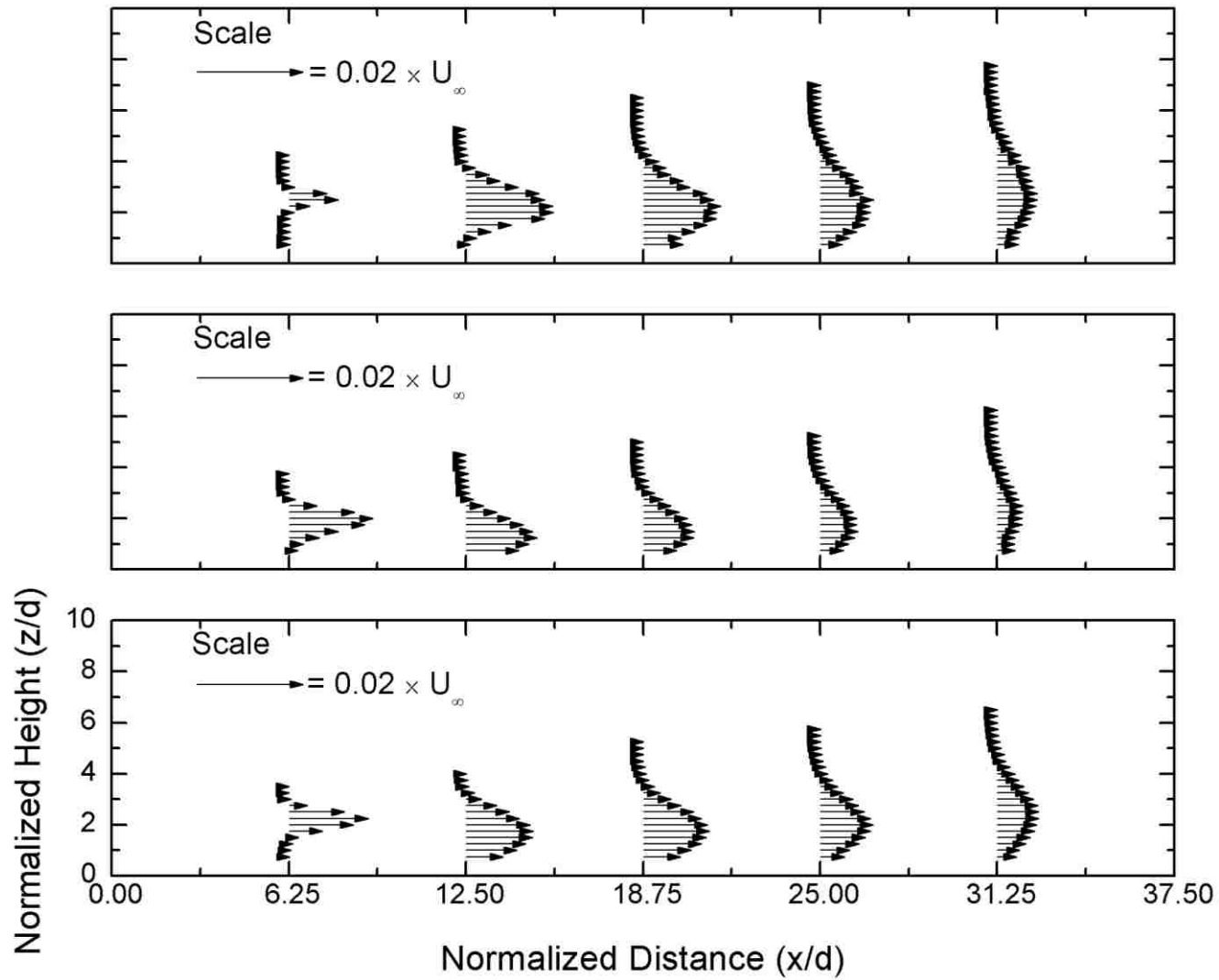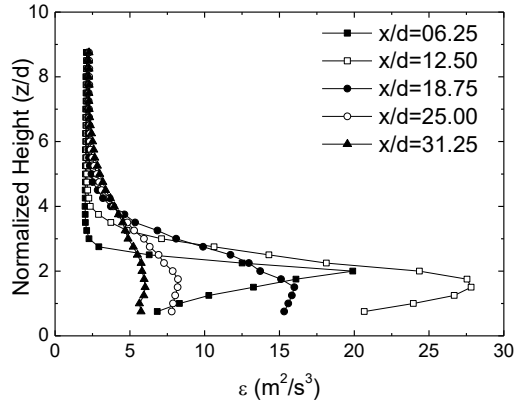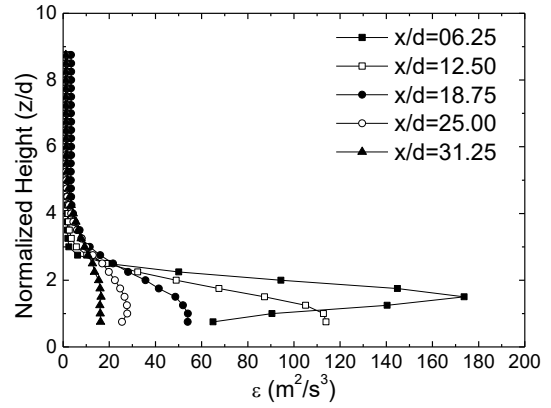
Figure A.8 Absolute Tangential Reynolds Stresses ($\frac{|u \cdot w|}{U_\infty^2}$), top is Re_d=0.7×10^3, middle is $Re_d = 1.4 \times 10^3$ and bottom is $Re_d = 2.0 \times 10^3$
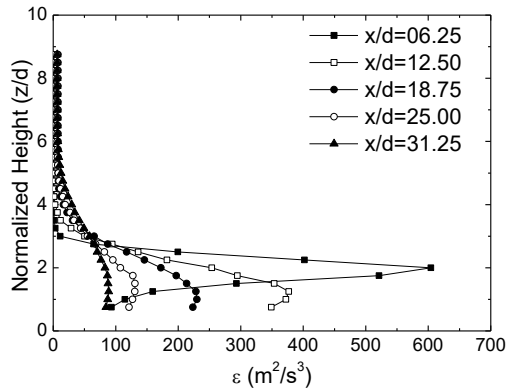
A.4.5 Dissipation Rate

(a)

(b),

(c)

Figure A.9 Energy dissipation rates trends for (a) $Re_d = 0.7 \times 10^3$, (b) $Re_d = 1.4 \times 10^3$ and (c) $Re_d = 2.0 \times 10^3$.

The trends of the dissipation rate are depicted in Figure A.9. Dissipation rate represents the rate at which turbulent kinetic energy is lost via viscosity to heat. This typically occurs most significantly when there is a lot of turbulence and/or viscosity. With the air viscosity remaining fixed, the peak dissipation rate conforms to the maximum turbulence location (see Figure A.6). For the lowest studied Reynolds number ($Re_d = 0.7 \times 10^3$) case, the

dissipation rate peaks around x/d of 12.50, instead of x/d = 6.25, implying that much turbulence is still being generated in the wake downstream of x/d = 6.25. This is not the situation at the higher Reynolds number ($Re_d = 1.4 \times 10^3$ & $Re_d = 2.0 \times 10^3$) cases, where the maximum dissipation rate rapidly subsides in the stream-wise direction.

A.4.6 Skewness

The deviation from a Gaussian distribution of data can be qualified by the skewness. Snapshots of three velocity signals, along with the skewness and kurtosis values are presented in Figure A.10. Figure A.10 (a) shows a more or less un-skewed signal with a skewness factor of 0.16. Signal (b) is positively skewed; when the velocity fluctuates in the positive direction (above the mean), it goes very positive, whereas it spends most of its time in the negative direction with a low magnitude. As far as the skewness is concerned, the opposite is true for Signal (c), except that the distribution is substantially more 'peaked.'
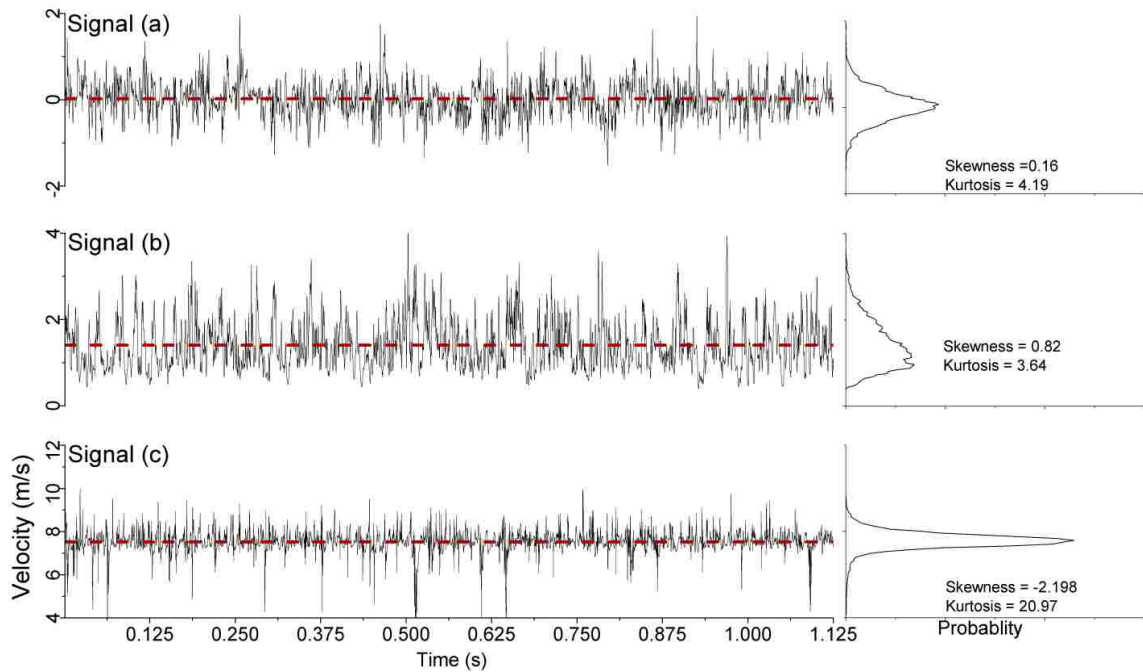

Figure A.10 Snippets of $Re_d = 2.0 \times 10^3$ velocity data. Signal (a) is W component at x/d = 06.25 and z/d = 0.75, signal (b) is U component at x/d = 06.25 and z/d = 02.25, and signal (c) is U component at x/d = 12.50 and z/d = 03.25. Probability distribution, Skewness and Kurtosis values for each signal are also presented

104

Skewness for the studied conditions is detailed in Figure A.11. Within the scatter of experimental data, it can be seen that the U skewness factor in the free-stream stays around zero. Approaching the plate, it tends toward a negative value, indicating less-frequent but sharp downward fluctuations in the midst of more-frequent but mild forward fluctuations. This coincides with the upper velocity shear (Figure A.4) and the turbulence gradient (Figure A.6). Note that at each x/d position, the skewness factor reaches zero at the vertical (z) location where peak turbulence intensity is detected. This is similar to the findings of Fouladi et al [34] for turbulence downstream of a partial grid. Further decrease in z/d leads to crossing the zero skewness and subsequently, somewhat positive skewness factor, before it levels out to zero again. The lowest studied Reynolds number case in Figure A.11 (a) is somewhat unique. The near-surface skewness factor is very positive, larger than 3, at x/d=6.25. As discussed earlier, there is still a lot of turbulence generation occurring at this location.
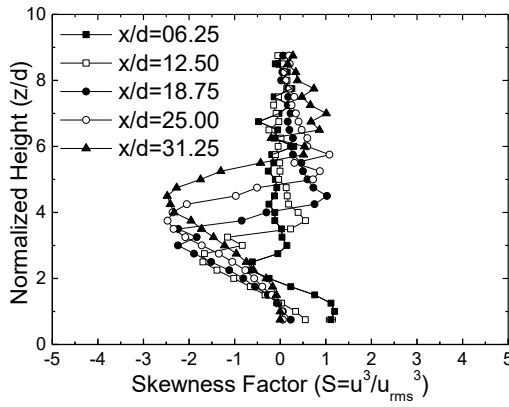
Observations comparable to those of the u component are noted for the w component, though with less consistency, presumably due to the lack of a prevailing flow in the z direction. As mentioned earlier, there is also more uncertainty regarding the direction of the fluctuation.
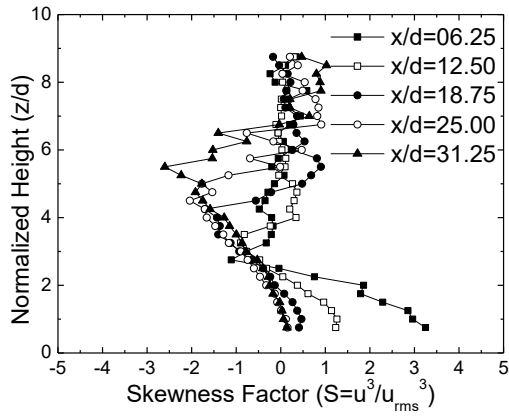
(a) U-component at $Re_d = 0.7 \times 10^3$
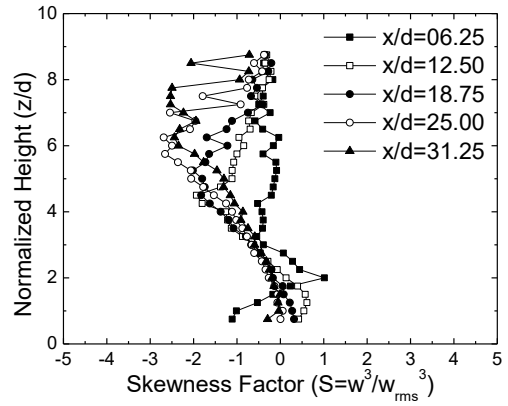
(b) W-component at $Re_d = 0.7 \times 10^3$

(c) U-component at $Re_d = 1.4 \times 10^3$

(d) W-component at $Re_d = 1.4 \times 10^3$

(e) U-component at $Re_d = 2.0 \times 10^3$

(f) W-component at $Re_d = 2.0 \times 10^3$

Figure A.11 u and w Skewness factors for the different studied Reynolds numbers
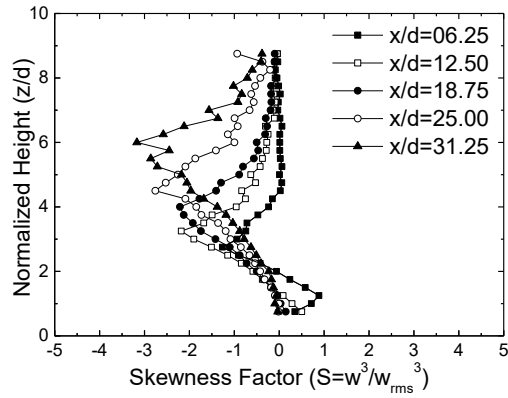
A.4.7 Kurtosis

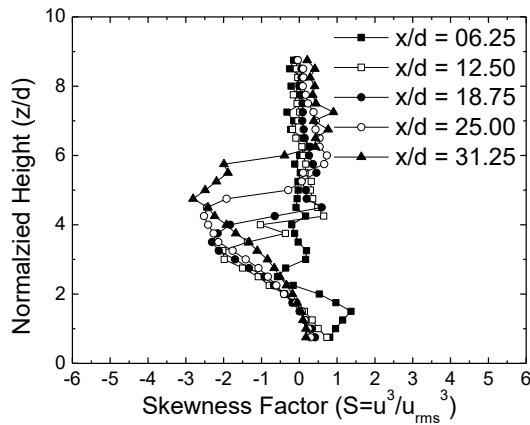(a) U-component at $Re_d = 0.7 \times 10^3$

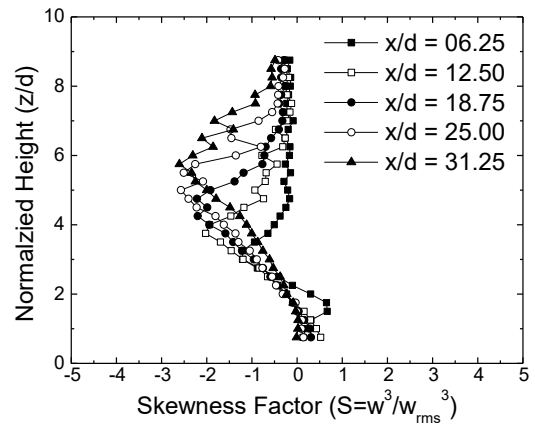(b) W-component at $Re_d = 0.7 \times 10^3$

(c) U-component at $Re_d = 1.4 \times 10^3$
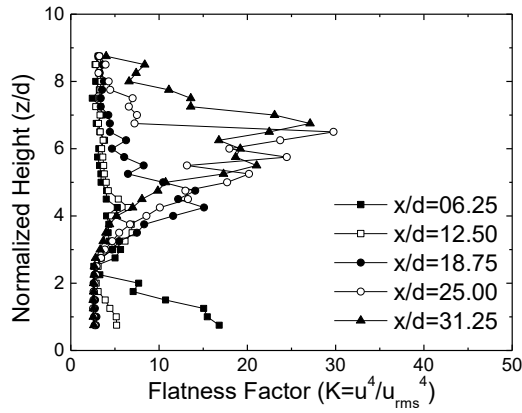
(d) W-component at $Re_d = 1.4 \times 10^3$

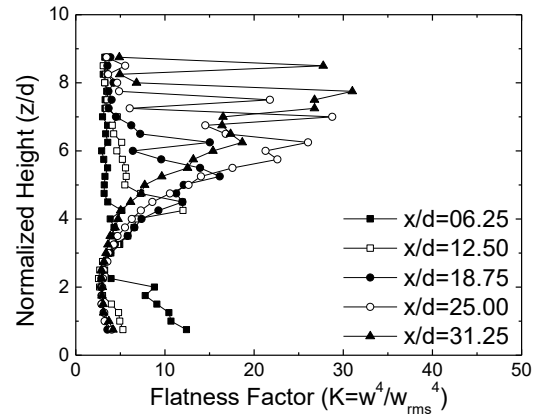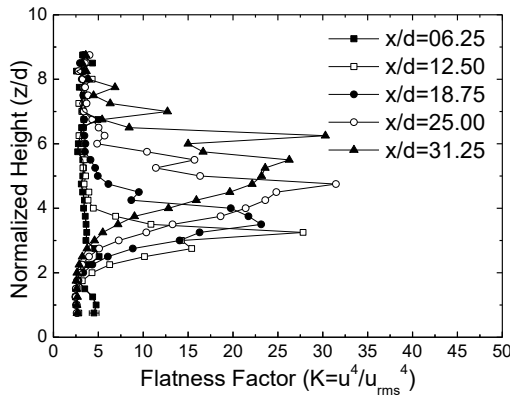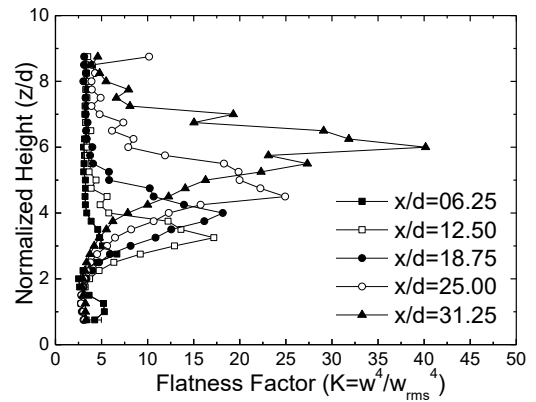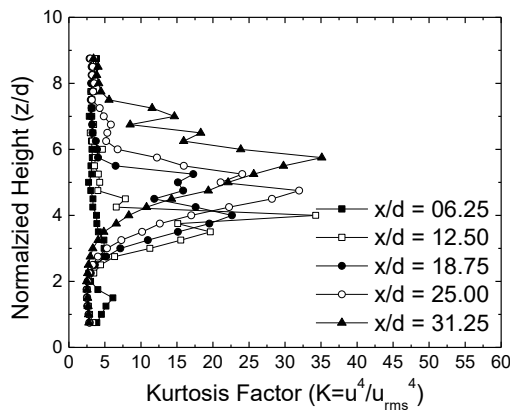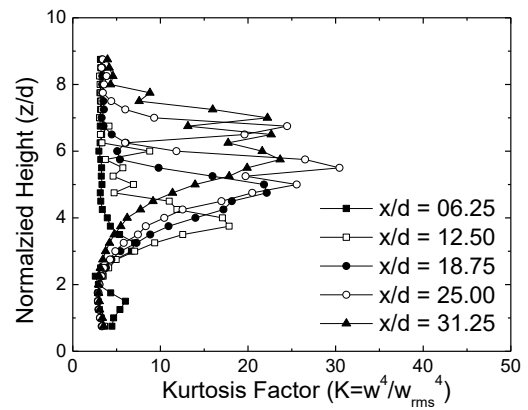(e) U-component at $Re_d = 2.0 \times 10^3$

(f) W-component at $Re_d = 2.0 \times 10^3$

Figure A.12 u and w Kurtosis factors for the studied Reynolds numbers

Other than the skewness factor, Figure A.10 also shows the flatness or Kurtosis factor of the three sample velocity data sets. It is clear that the value of kurtosis factor indicates how peaked the probability distribution density is. A completely random, Gaussian variation will give a kurtosis value of 3; which is the case in the free stream, where the skewness factor is zero. As the fluctuating velocity is raised to the fourth power, kurtosis is a highly sensitive parameter, and thus larger variations and uncertainties. The kurtosis factor has also been employed to indicate the intermittency of the velocity fluctuations.

It is clear that in general, the upper shear region has relatively large Kurtosis factor. Beyond the uncertainties, this suggests that vortex shedding tends to substantially increase the flatness, resulting in a signal with acute infrequent fluctuations similar to that shown in Figure A.10(c). It is interesting to note that the kurtosis factor approaches the Gaussian flatness of 3 where the maximum turbulence occurs, below this height (z/d) it tends to slightly increase, especially for the $Re_d = 0.7 \times 10^3$ case at x/d = 6.25.

A.4.8 Kolmogorov length

A smaller value of Kolmogorov scale is associated with intense turbulence [35] and indicates higher energy dissipation. Not surprisingly, the smallest Kolmogorov scale occurs where the velocity shear is the greatest, i.e., where most turbulence is generated. With the largest scales bounded within the wake and/or the boundary layer, the corresponding 'turbulent energy cascade' is truncated, and thus the Kolmogorov scale remains small. Above the inflection point of the velocity profile, the turbulence decreases, and therefore, in the absence of confinement, the Kolmogorov length enlarges. The general increase in Kolmogorov length farther downstream is also evident, concurring with the decay of far wake turbulence. Beyond a height of z/d = 4, the turbulence is not intense enough to grant consistent and accurate deduction of Kolmogorov length, and hence, no data is presented for z/d > 4.

(a)   (b)

(c)
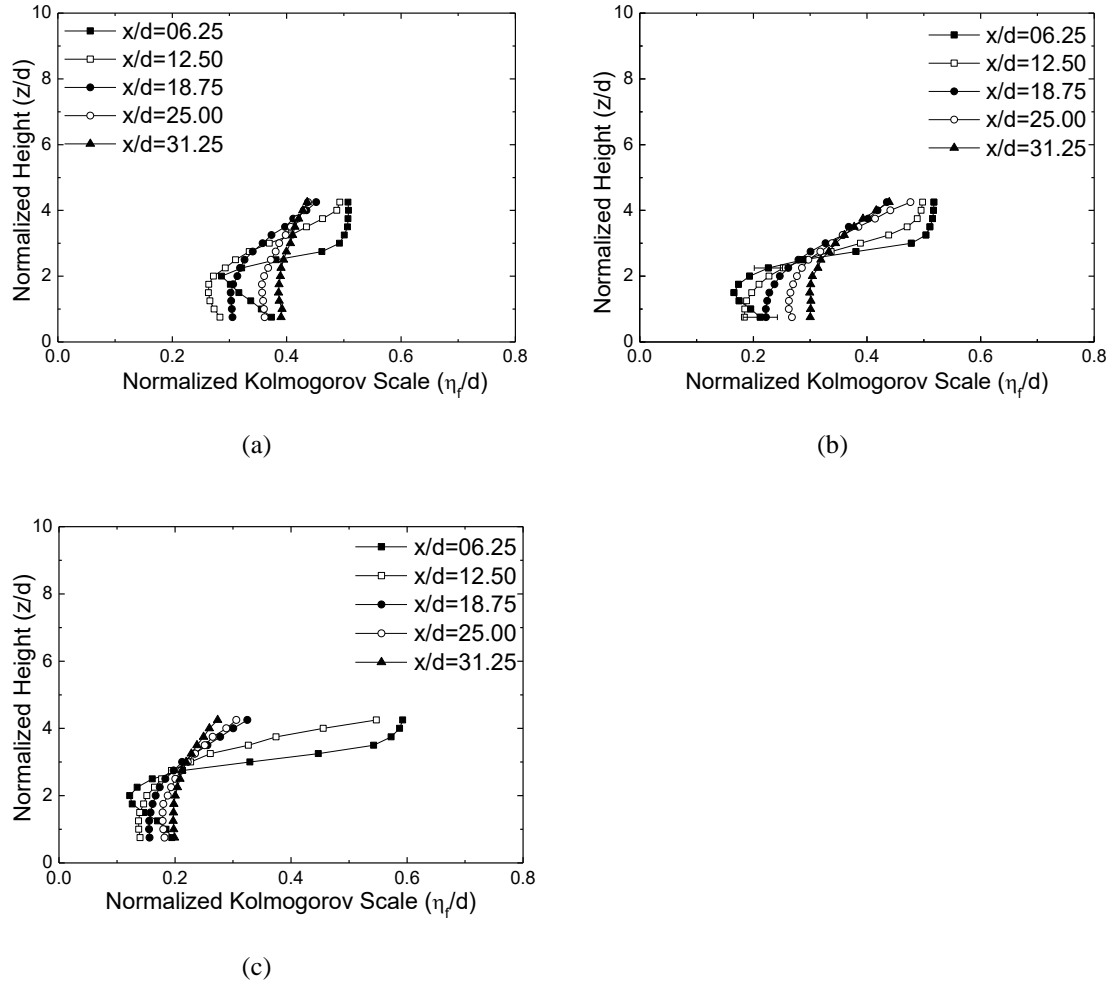
Figure A.13 Normalized Kolmogorov scale for (a) $Re_d = 0.7 \times 10^3$, (b) $Re_d = 1.4 \times 10^3$ and (c) $Re_d = 2.0 \times 10^3$

A.5 Conclusion

The flow behind a cylindrical rod placed at the leading edge of a flat plate was evaluated using hotwire measurements at $x/d = 6.25$ to 31.25 and $Re_d = 0.7 \times 10^3$ to 2.0×10^3; where x = distance downstream and d = cylinder diameter. Strong vortex shedding with near-isolated cylinder Strouhal number ($St \approx 0.2$) was detected at near wake, over the upper shoulder of the cylinder where the highest velocity shear took place. Some faint vortex shedding appeared to linger along in the neighborhood of this vortex and turbulence formation region. The turbulence wake expanded and merged unto the flat plate boundary

layer. The near-surface turbulence remained notable beyond the farthest studied distance of x/d = 31.25.

Acknowledgements

References

[1]   H. Schlichting, K. Gersten, Boundary-layer theory, 9th ed., Springer Berlin Heidelberg, Berlin, Heidelberg, 2017. doi:10.1007/978-3-662-52919-5.

[2]   E. Achenbach, Influence of surface roughness on the cross-flow around a circular cylinder, J. Fluid Mech. 46 (1971) 321. doi:10.1017/S0022112071000569.

[3]   P. Bearman, M. Zdravkovich, Flow around a circular cylinder near a plane boundary, J. Fluid Mech. 89 (1978) 33–47. doi:10.1017/S002211207800244X.

[4]   F. Angrilli, S. Bergamaschi, V. Cossalter, Investigation of wall induced modifications to vortex shedding from a circular cylinder, J. Fluids Eng. 104 (1982) 518. doi:10.1115/1.3241896.

[5]   M. Zdravkovich, Intermittent flow separation from flat plate induced by a nearby circular cylinder., Proc. 2nd Int. Symp. Flow Vis. (Ed. W. Merzkirch), Bochum, West Ger. (1980) 265–270.

[6]   M. Zdravkovich, Forces on a circular cylinder near a plane wall, Appl. Ocean Res. 7 (1985) 197–201. doi:10.1016/0141-1187(85)90026-4.

[7]   E. Marumo, K. Suzuki, T. Sato, Turbulent heat transfer in a flat plate boundary layer disturbed by a cylinder, Int. J. Heat Fluid Flow. 6 (1985) 241–248. doi:10.1016/0142-727X(85)90056-6.

[8] S. Taniguchi, K. Miyakoshi, Fluctuating fluid forces acting on a circular cylinder and interference with a plane wall, Exp. Fluids. 9 (1990) 197–204. doi:10.1007/BF00190418.

[9] O. Griffin, M. Hall, Review—Vortex shedding lock-on and flow control in bluff body wakes, J. Fluids Eng. 113 (1991) 526. doi:10.1115/1.2926511.

[10] J. Sheridan, J. Lin, D. Rockwell, Flow past a cylinder close to a free surface, J. Fluid Mech. 330 (1997) S002211209600328X. doi:10.1017/S002211209600328X.

[11] C. Lei, L. Cheng, K. Kavanagh, Re-examination of the effect of a plane boundary on force and vortex shedding of a circular cylinder, J. Wind Eng. Ind. Aerodyn. 80 (1999) 263–286. doi:10.1016/S0167-6105(98)00204-9.

[12] D. Sumner, S. Wong, S. Price, M. Païdoussis, Fluid behaviour of side-by-side circular cylinders in steady cross-flow, J. Fluids Struct. 13 (1999) 309–338. doi:10.1006/jfls.1999.0205.

[13] C. Norberg, Flow around a circular cylinder: Aspects of fluctuating lift, J. Fluids Struct. 15 (2001) 459–469. doi:10.1006/jfls.2000.0367.

[14] S. Price, D. Sumner, J. Smith, K. Leong, M. Païdoussis, Flow visualization around a circular cylinder near to a plane wall, J. Fluids Struct. 16 (2002) 175–191. doi:10.1006/jfls.2001.0413.

[15] X. Wang, S. Tan, Near-wake flow characteristics of a circular cylinder close to a wall, J. Fluids Struct. 24 (2008) 605–627. doi:10.1016/j.jfluidstructs.2007.11.001.

[16] M. Akoz, Flow structures downstream of the horizontal cylinder laid on a plane surface, Proc. Inst. Mech. Eng. Part C-Journal Mech. Eng. Sci. 223 (2009) 397–413. doi:Doi 10.1243/09544062jmes1111.

[17] S. Sarkar, S. Sarkar, Vortex dynamics of a cylinder wake in proximity to a wall, J. Fluids Struct. 26 (2010) 19–40. doi:10.1016/j.jfluidstructs.2009.08.003.

[18] G. He, J. Wang, C. Pan, Initial growth of a disturbance in a boundary layer influenced by a circular cylinder wake, J. Fluid Mech. 718 (2013) 116–130. doi:10.1017/jfm.2012.599.

[19] G. He, C. Pan, J. Wang, Dynamics of vortical structures in cylinder/wall interaction with moderate gap ratio, J. Fluids Struct. 43 (2013) 100–109. doi:10.1016/j.jfluidstructs.2013.09.005.

[20] G. He, J. Wang, Flat plate boundary layer transition induced by a controlled near-wall circular cylinder wake, Phys. Fluids. 27 (2015) 24106. doi:10.1063/1.4907744.

[21] B. Zhou, X. Wang, W. Guo, W. Gho, S. Tan, Control of flow past a dimpled circular cylinder, Exp. Therm. Fluid Sci. 69 (2015) 19–26. doi:10.1016/j.expthermflusci.2015.07.020.

[22] M. Raiola, A. Ianiro, S. Discetti, Wake of tandem cylinders near a wall, Exp. Therm. Fluid Sci. 78 (2016) 354–369. doi:10.1016/j.expthermflusci.2016.06.003.

[23] G. He, C. Pan, L. Feng, Q. Gao, J. Wang, Evolution of Lagrangian coherent structures in a cylinder-wake disturbed flat plate boundary layer, J. Fluid Mech. 792 (2016) 274–306. doi:10.1017/jfm.2016.81.

[24] G. He, J. Wang, C. Pan, L. Feng, Q. Gao, A. Rinoshika, Vortex dynamics for flow over a circular cylinder in proximity to a wall, J. Fluid Mech. 812 (2017) 698–720. doi:10.1017/jfm.2016.812.

[25] S. Peter, A. De, Characteristics of the wake behind a transversely oscillating cylinder near a wall, J. Fluids Eng. 139 (2017) 31201. doi:10.1115/1.4035012.

[26] D. Gao, W. Chen, H. Li, H. Hu, Flow around a circular cylinder with slit, Exp. Therm. Fluid Sci. 82 (2017) 287–301. doi:10.1016/j.expthermflusci.2016.11.025.

[27] F. Jiang, B. Pettersen, H.I. Andersson, Influences of upstream extensions on flow around a curved cylinder, Eur. J. Mech. - B/Fluids. (2017). doi:10.1016/j.euromechflu.2017.08.006.

[28] S. Bose, S. Dey, Far-wake flows downstream of cylinders: A novel generalized similarity method, Eur. J. Mech. - B/Fluids. (2017). doi:10.1016/j.euromechflu.2017.08.008.

[29] U. Sen, A. Mukhopadhyay, S. Sen, Effects of fluid injection on dynamics of flow past a circular cylinder, Eur. J. Mech. - B/Fluids. 61 (2017) 187–199. doi:10.1016/j.euromechflu.2016.11.006.

[30] C. Lei, L. Cheng, S. Armfield, K. Kavanagh, Vortex shedding suppression for flow over a circular cylinder near a plane boundary, Ocean Eng. 27 (2000) 1109–1127. doi:10.1016/S0029-8018(99)00033-5.

[31] A. Dipankar, T. Sengupta, Flow past a circular cylinder in the vicinity of a plane wall, J. Fluids Struct. 20 (2005) 403–423. doi:10.1016/j.jfluidstructs.2005.01.001.

[32] D. Ting, Basics of Engineering Turbulence, Academic Press, 2016.

[33] G. Taylor, The Spectrum of Turbulence, Proc. R. Soc. A Math. Phys. Eng. Sci. 164 (1938) 476–490. doi:10.1098/rspa.1938.0032.

[34] F. Fouladi, P. Henshaw, D. Ting, Turbulent flow over a flat plate downstream of a finite height perforated plate, J. Fluids Eng. 137 (2014) 21203. doi:10.1115/1.4028402.

[35] F. Fouladi, P. Henshaw, D. Ting, Effect of a triangular rib on a flat plate boundary layer, J. Fluids Eng. 138 (2015) 11101. doi:10.1115/1.4031161.

Appendix B. Experimental Uncertainty Analysis

The uncertainty of a measured independent parameter (such as temperature (T), time-averaged velocity ($\bar{U}$) and fluctuation velocity (u_{rms})) consists of bias (B) and precision (P) errors. Bias error arises from the calibration, data acquisition and data reduction processes. Total bias is calculated using Equation B - 1. The bias errors produced by the hot wire and thermal camera OEMs are around 4% and 2%, respectively.

$$B = \sqrt{B_1^2 + B_2^2 + \cdots + B_k^2} \qquad \text{(B - 1)}$$

Precision uncertainty is due to random errors. In this experiment, repeatability is the major factor contributing to precision errors. The repeatability error for each parameter was calculated using the Student's T distribution. Ten samples of a velocity dataset were acquired at a random position for each Re_d. The same process was performed for thermal data.

The precision error of independent parameters was then calculated using the following method. First, the average and standard deviations of the ten values were calculated using equations B – 2 and B – 3:

$$\bar{X} = \frac{1}{N-1} \sum_{i=1}^{N} X_i \qquad \text{(B - 2)}$$

$$X_{Sd} = \sum_{i=1}^{10} \frac{(X_i)^2}{N-1} \qquad \text{(B - 3)}$$

Precision uncertainty is then calculated using the following equation:

$$P = \frac{\dfrac{X_{Sd} \cdot t}{\sqrt{10}}}{\bar{X}} \qquad \text{(B- 4)}$$

where t is obtained from the Student's t-tables for a two-tail distribution at a 95% confidence interval. The bias and precision errors were combined to give the overall uncertainty (W):

114

$$W = \sqrt{B^2 + P^2} \qquad \text{(B - 5)}$$

For variables dependent on instantaneous velocity (U), the equation for calculating uncertainty is as follows:

$$\frac{W_{Tu_u}}{Tu_u} = \sqrt{\left(\frac{W_{\bar{U}}}{\bar{U}}\right)^2 + \left(\frac{W_{u_{rms}}}{u_{rms}}\right)^2} \qquad \text{(B - 6)}$$

$$\frac{W_{u \cdot w}}{u \cdot w} = \sqrt{\left(\frac{W_{Tu_u}}{Tu_u}\right)^2 + \left(\frac{W_{Tu_w}}{Tu_w}\right)^2} \qquad \text{(B - 7)}$$

The uncertainty propagation in parameters calculated from temperature data is shown below:

$$\frac{W_{Q_{Radiation}}}{Q_{Radiation}} = \sqrt{4 \cdot \left(\frac{W_T}{T}\right)^2} \qquad \text{(B - 8)}$$

$$\frac{W_{Q_{Total}}}{Q_{Total}} = \sqrt{\left(\frac{W_T}{T}\right)^2} \qquad \text{(B -9)}$$

$$\frac{W_{Q_{Convection}}}{Q_{Convection}} = \sqrt{\left(\frac{W_{Q_{Total}}}{Q_{Total}}\right)^2 + \left(\frac{W_{Q_{Radiation}}}{Q_{Radiation}}\right)^2} \qquad \text{(B- 10)}$$

$$\frac{W_h}{h} = \sqrt{\left(\frac{W_T}{T}\right)^2 + \left(\frac{W_{Q_{Convection}}}{Q_{Convection}}\right)^2} \qquad \text{(B - 11)}$$

$$\frac{W_h}{h} = \sqrt{\left(\frac{W_T}{T}\right)^2 + \left(\frac{W_{Q_{Convection}}}{Q_{Convection}}\right)^2} \qquad \text{(B - 12)}$$

VITA AUCTORIS

NAME:	Ashhar Ahmed
PLACE OF BIRTH:	Karachi, Pakistan
YEAR OF BIRTH:	1987
EDUCATION:	NED University of Engineering and Technology, Karachi, Pakistan, 2006-2010, B.Eng.
	University of Windsor, Windsor, ON, 2015-2018, M.A.Sc.